ESMRMB

European Society for Magnetic Resonance in Medicine and Biology

ESMRMB 2019 Congress

October 3-5, Rotterdam/NL

Book of Abstracts

Electronic Posters / Paper Posters / Clinical Review Posters / Software Exhibits

DOI: 10.1007/s10334-019-00756-0

www.esmrmb.org

P01 Electronic and Paper Posters

Applications of MRI

P01.01

Diagnosis of deep vein thrombosis based on a DANTE-prepared gradient echo sequence

H. Mao[1], K. Peng[2], X. Guan[1], X. Zhang[3], **G. Xie**[1]

[1]Guangzhou Medical University, Department of Biomedical Engineering, Guangzhou, CHINA, [2]Nanshan people's hospital, Department of Radiology, Shenzhen, CHINA, [3]Siemens healthineer, Shenzhen, CHINA

Purpose/Introduction: DVT can be diagnosed by contrast-free magnetic resonance (MR) imaging, such as MR direct thrombus imaging (MRDTI)[1] and black-blood MR thrombus imaging (BTI)[2]. DANTE-FLASH is another black-blood MR technique previously proposed for vessel wall imaging at lower extremities. This work was aimed to investigate the feasibility of using DANTE-prepared FLASH sequence (DANTE-FLASH) to diagnose DVT.

Subjects and Methods: The IRB approved prospective study was performed on a 3 T scanner, and consecutively enrolled 6 healthy volunteers and 16 patients. All subjects underwent three-station DANTE-FLASH scan to cover bilateral lower limbs. Ultrasound and MR direct thrombus imaging (MRDTI) were also conducted to provide standard references. The scan parameters for the DANTE module were: FA = 15°, pulse train length = 150. The parameters for the FLASH readout were: echo spacing/TE = 5.4/2.08 ms, FA = 12°, TR = 800 ms, water excitation for fat suppression. The scan parameters of MRDTI were the same as those of FLASH readout in DANTE-FLASH except the inversion recovery time (200 ms) and flip angle (18°). The image quality of DANTE-FLASH and MRDTI was quantitatively analyzed by image signal-to-noise ratio (SNR), apparent contrast to noise ratio (CNR) between muscle and dark venous lumen, and CNR between thrombus and dark venous lumen. The diagnosis performance was qualitatively analyzed by two radiologists independently with a 4-point scale (1 = poor, 4 = excellent). The sensitivity (SE), specificity (SP), positive and negative predictive values (PPV and NPV), and accuracy (ACC) of DANTE-FLASH were calculated using MRDTI and US as references, respectively.

Results: Compared to MRDTI, DANTE-FLASH achieved better image quality in terms of SNR, CNR, and image quality scores (Table 1). Thrombi were correctly identified by DANTE-FLASH and matched well with those detected by MRDTI (Figure 1). It was noted that the iso-intense thrombus was easier to identify using DANTE-FLASH because it provides better blood suppression (Figure 2). Using US as reference, the diagnosis SE, SP, PPV, NPV and ACC of DANTE-FLASH were 86.79%, 95.51%, 71.88%, 98.21%, and 94.49%, respectively. Using MRDTI as reference, the values were 92.31%, 98.97%, 93.75%, 98.72% and 98.02%, respectively.

Discussion/Conclusion: DANTE-FLASH allows for direct visualization of thrombus, which may serve as an alternative for the diagnosis of DVT.

References:

1. Fowkes FJI, Price JF, Fowkes FGR. Incidence of Diagnosed Deep Vein Thrombosis in the General Population: Systematic Review. European Journal of Vascular & Endovascular Surgery 2003;25(1):1–5.

2. Moody AR. Magnetic resonance direct thrombus imaging. Journal of Thrombosis & Haemostasis 2010;1(7):1403–9.

P01.02

Dosimetric Impact of MRI Geometric inaccuracy in SBRT planning for liver cancer in the presence of motion

T. Torfeh, R. Hammoud, A. Khemissi, T. El Kaissi, S. Aouadi, S. Paloor, N. Al-Hammadi

Hamad Medical Corporation, National Center for Cancer Care & Research NCCCR, Radiation Oncology, Doha, QATAR

Purpose/Introduction: MRI is increasingly being used in radiotherapy applications for tumor delineation and tracking in the presence of respiratory motion [1]. The purpose of this work is to investigate the impact of system-related MR geometric inaccuracies on dose distributions for liver cancers.

Subjects and Methods: An in-house motion platform and a control point based phantom (Fig. 1) were used to calculate the MR inaccuracies (distortion and blur) during motion for a Cine sequence which is the standard sequence for target delineation in liver cancer RT [2].

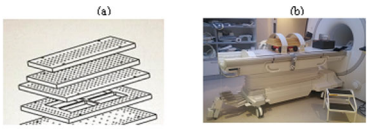

Fig. 1 a) View of the phantom showing the layers and b) the Phantom placed on a track attached to the motion motor positioned inside the MR.

Planning CT Images of 2 liver cancer patients were used. 3D shapes representing the liver, kidneys, heart, spinal cord and lungs were extracted to create 2 digital phantoms. Four set of images were then derived from each digital phantom by adding spherical targets of 50, 40, 30, 20 and 15 mm of diameter (Fig. 2).

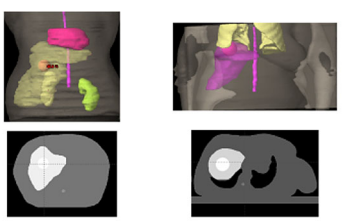

Fig. 2 a) 3D and 2D views of the digital phantoms extracted from a) the first patient and b) the second patient. Liver, heart, spinal cord, kidneys, lungs and the tumor are shown.

For each dataset, geometric inaccuracy was simulated by deforming the images based on the calculated distortion map and the blurring artifact.

Using a thresholding method, organs on the original and distorted datasets were automatically delineated. Using Eclipse^{TM} TPS, highly conformal volumetric modulated arc therapy (VMAT) plans were generated and optimized on the distorted dataset. These plans were then transferred to the original dataset where dose distribution was analyzed. Dose Volume Histograms (DVH) including D_{50}, D_{min} and D_{mean} were used to assess the accuracy.

Results: For geometric inaccuracies; the mean magnitude of the geometric distortion was 0.7, 0.9 and 1 mm for radial distances of 50, 100 and 150 mm respectively. Blurring was also observed during motion causing an increase in the Full Width at Half Maximum of the objects of ≈ 16%. Dosimetric evaluation showed that the dose received by the original set of images was higher than the dose received by the distorted images. Mean differences in the DVH parameters for the distorted and undistorted treatment plans ranged between − 1 and − 14% and − 1.8 and − 15% for the target and the OARs respectively. Results also showed that the difference in the DVH is inversely proportional to the target size (Fig. 3).

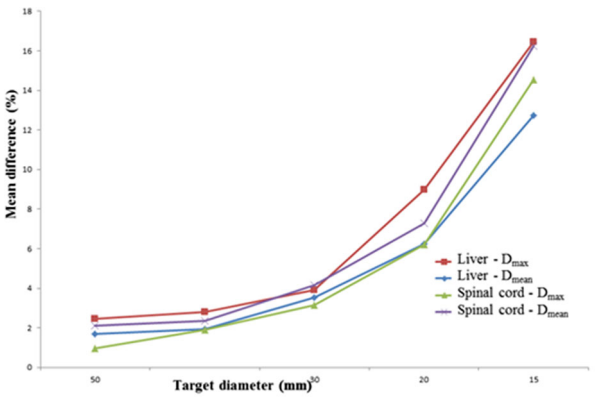

Fig. 2 a) 3D and 2D views of the digital phantoms extracted from a) the first patient and b) the second patient. Liver, heart, spinal cord kidneys, lungs and the tumor are shown.

Discussion/Conclusion: The dosimetric impact of MRI inaccuracies during motion on liver SBRT plans was analyzed. The methodology used in this study which is based on digital phantoms extracted from real patients, represents an important technique allowing the assessment of the dosimetric impact of organ deformation for different anatomic sites as well as treatment techniques.

References:

1. Cai J *et al*. Four-dimensional magnetic resonance imaging (4D-MRI) using image-based respiratory surrogate: a feasibility study. Med Phys. 2011;38:6384–6394.

2. Torfeh T *et al*. Geometric accuracy of the MR imaging techniques in the presence of motion. J Appl Clin Med Phys. 2018;19(2):168-175.

P01.03

Lipids composition of visceral fat in overweight and obese patients using 1^H NMR at 9.4T

A. Xavier[1,2,3], F. Zacconi[4], C. Morelli[1], M. Andia[3], S. Uribe[1]

[1]Pontificia Universidad Catolica de Chile, Santiago, CHILE, [2]Pontificia Universidad Catolica de Chile, Millennium Nucleus for Cardiovascular Magnetic Resonance, Santiago, CHILE, [3]Pontificia Universidad Catolica de Chile, Biomedical Imaging Center, Santiago, CHILE, [4]Pontificia Universidad Catolica de Chile, Faculty of Chemistry, Santiago, CHILE

Purpose/Introduction: The adipose tissue has big influence in the risk to develop multiple diseases. The fatty acids composition of this tissue could be related to various disorders like cancer and diabetes[1,2]. The purpose of this study is to investigate the fatty acids composition of visceral fat in overweight and obese patients by quantifying metabolites signals in H^1 NMR and estimating the diunsaturated (DUFA), monounsaturated (MUFA) and saturated fatty acids (SFA), and compare those estimations with Gas chromatography analysis.

Subjects and Methods: Visceral fat samples were collected from 10 patients that undergoing abdominal elective surgery. Those patients were classified in overweight and obese patients using the body mass index (BMI). Fatty Acids Methyl Esters (FAME) from the visceral fat were extracted[3] and analyzed using a 9.4T MRS (Bruker Bruker Ultra-shield) and gas chromatography (GC) with a mass spectrometer (Agilent technologies). We calculated the DUFA, MUFA and SFA by using the equations bellow[4]. We also calculated the contribution of the fatty acid with 16 carbons and 18 carbons. The peaks are shown in Figure 1.

$$DUFA = Area(F/E)$$
$$MUFA = 0.5 \times Area(D/E) - DUFA$$
$$SFA = 1 - (DUFA + MUFA)$$
$$f16 + f18 = 1$$
$$Area(B/E) = f16(12 \times SFA + 8 \times MUFA) + f18(14 \times SFA + 10 \times MUFA + 7 \times DUFA)$$

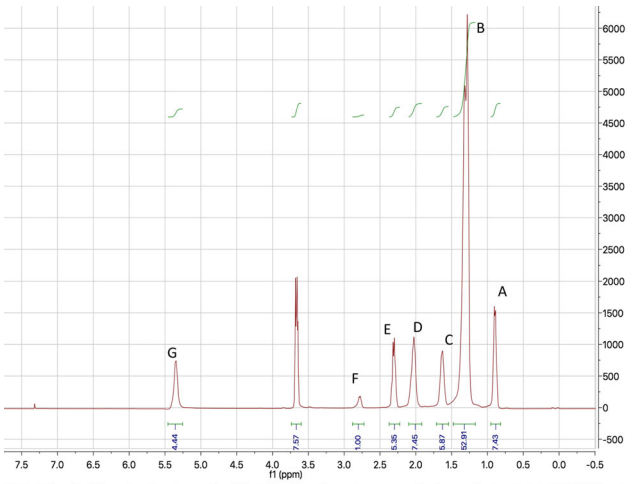

Fig 1. Fatty acids MR spectra of an obese patient. The letters above the peaks correspond to the equation to calculate DUFA, SFA and MUFA.

Results: In overweight patients the fat composition was 23.3± 3.8% DUFA, 48.8 ± 3.9% MUFA and, 27.9 ± 2.0% SFA. In obese patients the fat composition was 25.0 ±3.5% DUFA, 46.3 ± 3% MUFA and, 28.7 ± 1.7% SFA (Fig. 2). Also, the contribution of the fatty acid with 16 carbons were 20.0 ± 5.8% and 22.5 ± 3.7%, in overweight and obese patients respectively, and the contribution of the fatty acid with 18 carbons were 80.0 ± 5.8% and 77.5 ± 3.7% in overweight and obese patients, respectively. The MRS results presented a good correlation with the GC results. The DUFA, MUFA, SFA showed a correlation of 0.86, 0.85 y 0.72 ($p < 0.05$), respectively (Fig. 3).

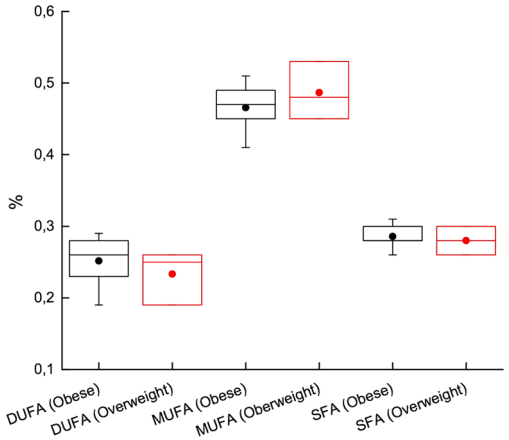

Fig 2. MRS results comparing DUFA, MUFA and SFA in Obese and overweight patients. No significant changes were observec between the obese group and overweight group), p-value>0.05 with Mann-Witney test.

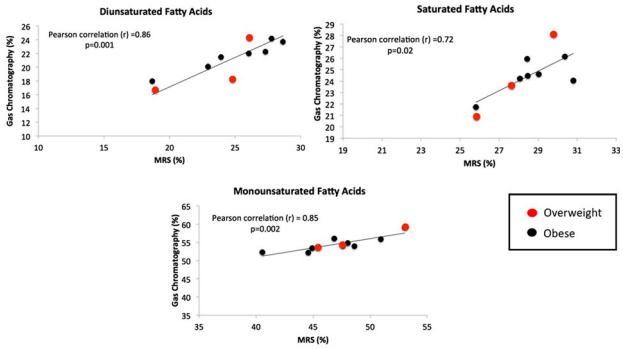

Fig 3. Correlation between MRS results and GC results corresponding to the DUFA (a), MUFA (b), SFA(c).

Discussion/Conclusion: Our results showed no significant difference in fatty acid composition comparing overweight patients with the obese ones. A good correlation between GC and MRS data was found. This technique could be performed no-invasively to increase the number of patients in all BMI conditions and that analysis could be performed as a routine exams.

Acknowledgements

This publication has received funding from Millenium Science Initiative of the Ministry of Economy, Development and Tourism, grant Nucleus for Cardiovascular Magnetic Resonance. CONICYT-PCHA/Doctorado Nacional/2016-21160835 and FONDECYT 1180525.

References:

1. SIMOSEN, N. et al. Am J Epidemiol. 1998
2. STORLIEN, L. et al. Br J Nutr. 2000
3. FOLCH, J. STANLEY, S. J. Biol. Chem. 1956.
4. REN, J. et al. Journal of Lipid Research. 2008

P01.04

Serial Imaging of Splenomegaly in the Sleeping Sickness Infected Mouse

S. Paterson[1], L. Carberry[1], W. Holmes[1], J. Rodgers[2]

[1]*University of Glasgow, Institute of Neuroscience and Psychology, Glasgow, UNITED KINGDOM,* [2]*University of Glasgow, Glasgow, UNITED KINGDOM*

Purpose/Introduction: Human African Trypanosomiasis (HAT) or sleeping sickness is a fatal parasitic disease that affects Africa. As the disease progresses, the parasites proliferate in the blood, lymph and many of the internal organs, including the brain, during the later stages of the disease. Splenomegaly is a known clinical symptom associated with HAT[1]. This research uses a well-established and characterised murine model of HAT to assess the changes in spleen volume over time as the infection progresses using serial MRI.

Subjects and Methods: Six female CD-1 mice were each scanned on day 0, 7, 14, 21 and 28 post trypanosome infection. Volume T1 FLASH (TR = 600 ms, TE = 2.6 ms) and T2 RARE (TR = 8000 ms, TE = 55 ms) scans were performed with 30 × 1 mm slices using a custom-made cradle and a 4-channel rat surface coil on a Bruker 7T PharmaScan MRI system. At each time point, parasitaemia levels, body weight and blood samples were taken for analysis. At the end of the study, spleens were taken, weighed and processed for histology. MRI data was analysed using in-house MATLAB code. A ROI was selected around the spleen on each MRI slice (Figure 1) and the volume calculated. These individual slice volumes were summed to give the volume of the whole spleen.

Results: A clear increase in the size of the spleen was present in the mice from 7 days post infection (Figure 1) although the magnitude of the increase varied between animals (Figure 2a).

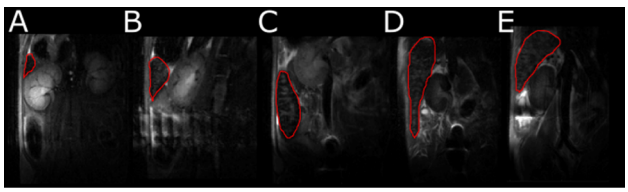

Figure 1: ROI taken for one slice at each time point of the infection: day 0 (A), 7 (B), 14 (C), 21 (D) and 28 (E), shown for one mouse, from a T2 volume scan. Splenomegaly is seen throughout all points of infection with changes in size and shape.

Figure 2b shows the percentage changes in volume of spleen size for each animal from early results for T2 data. The biggest increase in spleen size comes during day 14 and day 21 post-infection, where an average change of 2000% is seen. A small decrease in spleen size between days 21 and 28 post-infection was also detected. Haematological and histological analysis are on going to further investigate the splenomegaly.

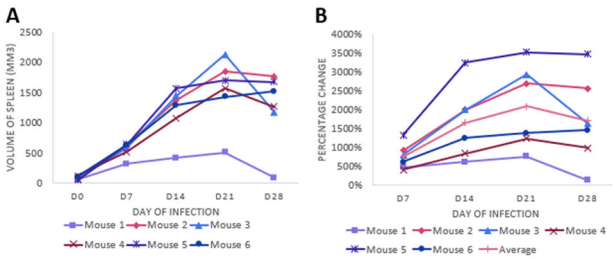

Figure 2: A) The volume of the spleen for each mouse in mm3. B) The percentage change of spleen volume compared to the original volume before infection of HAT. Spleen size increases until day 21 where the volume decreases by day 28 post infection.

Discussion/Conclusion: We have successfully imaged splenomegaly in a group of sleeping sickness infected mice over the course of a 28-day infection. This data shows that the average spleen size increases by 2000% at day 21 post-infection with the spleen decreasing slightly in size by day 28 post infection. Although splenomegaly is recognised in HAT, this is the first quantitative study using MRI to serially measure changes in spleen volume as the infection progresses and provides new insights into the pathogenesis of this parasitic infection.

References:

[1]Kennedy PGE and Rodgers J (2019) Clinical and Neuropathogenetic Aspects of Human African Trypanosomiasis. Front. Immunol. 10:39. https://doi.org/10.3389/fimmu.2019.00039.

P01.05

Homogeneity of hepatic fat response to dietary interventions

P. Sedivy[1], M. Drobny[1], M. Dezortova[1], M. Burian[1], T. Dusilova[2], J. Kovar[2], M. Hajek[1]

[1]Institute for Clinical and Experimental Medicine, MR unit, Prague, CZECH REPUBLIC, [2]Institute for Clinical and Experimental Medicine, Experimental Medicine Centre, Prague, CZECH REPUBLIC

Purpose/Introduction: We studied changes of hepatic fat content (HFC) according to Longo[1] in the group of 10 healthy volunteers after two different dietary interventions[2]. We investigated the HFC changes using proton MR spectroscopy (MRS) in three liver volumes of interest. The purpose of the study was to describe HFC changes during the day.

Subjects and Methods: 10 healthy male volunteers (39 ± 10 years, BMI 26 ± 2 kg/m^2, HFC under 5%) were repeatedly examined by MRS. All the subjects provided their informed consent in line with local Ethical Committee rules.

Two dietary interventions were compared during 6 h experiments:

(1) prolonged fasting
(2) high-fat load (150 g of fat in dairy cream).[2]

Concentrations of triglycerides (TG), non-esterified fatty acids (NEFA), glucose and insulin were monitored.

3T MR system (Siemens Trio) with surface 8–channel array coil was used. MR protocol consisted of T2-weighted HASTE images and PRESS single voxel spectroscopy (TR/TE = 4500/30 ms, 1 acquisition, breath hold; three spectra were measured). Three volumes of interest (VOI, 30 ml; see Fig 1) in the liver were selected for HFC measurement.

MR spectra were evaluated by LCModel software[3] with T2 corrections[4]. Obtained data were statistically analyzed by Linear Mixed Model (LMM; R soft.) and $\alpha = 0.05$.

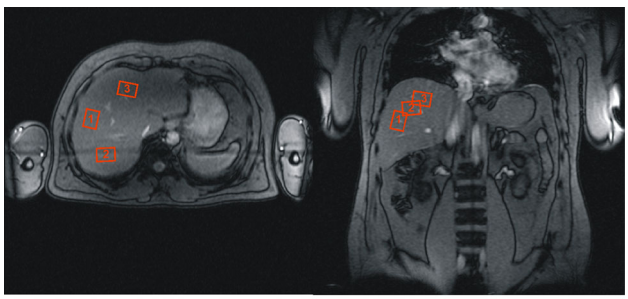

Figure 1: Positions of the three VOIs for PRESS ^{1}H MRS (red ones). Parameters of PRESS sequence were following: 1 acquisition, TE=30 ms, VOI size 40x30x25 cm^3, three spectra from each VOI were obtained.

Results: The HFC changes in three VOI measured by MRS during 6 h at two dietary interventions are summarized in Table 1.

HFC was increased 6 h after high-fat load and was not changed during fasting—these changes were detected in all three VOI (Table 2). In spite of the consistent response of HFC with time, the results of HFC measurements were inhomogeneous between three VOI (Table 2).

Table 1: HFC results obtained from MRS results by linear mixed model. Complete dataset consists of values measured twice during the day under two dietary interventions. The data are means±SE.

Diet	Time [hours]	Position 1 [%]	Position 2 [%]	Position 3 [%]	Mean [%]
Fasting	0	1.7±0.4	2.2±0.4	1.8±0.4	1.9±0.3
	6	1.8±0.4	2.2±0.4	1.9±0.4	2.0±0.2
Fat	0	1.9±0.4	2.3±0.4	2.0±0.4	2.1±0.2
	6	2.3±0.4	2.7±0.4	2.4±0.4	2.5±0.2

Table 2: Effect of dietary intervention on the HFC and its homogeneity based on linear mixed model analysis. There are differences in HFC during the day measured by MRS between two dietary interventions and also among three positions of VOI (differences from value measured in position 1). In the last column the p-values of individual significance changes are shown.

Diet	Type	HFC difference [%]	p-value
	Fasting	0.08	0.66
	Fat	**0.41**	**0.02**
Homogeneity	**Position**	**HFC difference [%]**	**p-value**
	2	**0.44**	**<0.01**
	3	0.10	0.52

Discussion/Conclusion: Our results show that changes of the absolute concentration of HFC after dietary intervention can be measured by MRS during 1 day (the HFC changes throughout the experiments are consistent with changes in concentrations of TG and NEFA in plasma). Our results also demonstrate that lipid accumulation is inhomogeneous even the absolute concentration of HFC is low (inhomogeneity of fat distribution was described in the literature for significantly higher fat content HFC > 10%[5]). Absolute size of HFC differences depends on the voxel position in the liver (see Table 2, the lipid accumulation is the smallest in the voxel 2).

The borderline between homogeneous and inhomogeneous liver tissue can be derived from the confidence interval obtained from LMM analysis. It is approx. 0.8% of absolute HFC measured by MRS method. These outputs can be used for decision making on local steatosis occurrence.

Supported by MH CZ—DRO (IKEM, IN 00023001) and grant nr. 16-28427A.

References:

1. Longo R. et al.: JMRI 1995;5, 281.
2. Dezortova M. et al.: In: Proc. of 26. ISMRM-ESMRMB meeting, 2018.
3. Provencher S.: NMR Biomed. 2001;14, 264.
4. Hájek M. et al.: MAGMA 2011; 24, 297.
5. Bonekamp S. et al.: JMRI 2014; 39, 1525.

P01.06

Comparison of Fused Diffusion-Weighted Imaging Using Unenhanced MR imaging and Abbreviated Postcontrast-Enhanced MR imaging in Patients with Breast Cancer

K. J. Nam, K. S. Choo, Y.-J. Jeong

Pusan National University Yangsan Hospital, Radiology, Yangsan-si, SOUTH KOREA

Purpose/Introduction: To determine what percentage of breast cancers were detectable by fused diffusion-weighted imaging (DWI) using unenhanced magnetic resonance imaging (MRI) and abbreviated postcontrast-enhanced MRI.

Subjects and Methods: This retrospective study was approved by the institutional review board. The requirement to obtain informed consent was waived. Between October 2016 and October 2017, 194 consecutive women (mean age 54.2 years; age range 28–82 years) with newly diagnosed unilateral breast cancer who underwent preoperative 3.0 T breast MRI with DWI were evaluated. A senior radiologist identified the location of the index caner on full dynamic contrast enhanced MRI before analysis. Both fused DWI and abbreviated MRI were reviewed independently by two radiologists for detection of index cancer which showed the most suspicious finding in both breasts, location, lesion conspicuity, lesion type, and lesion size. Each reader reviewed the 2 datasets at least 2 weeks interval.

Results: Detection rates of index cancers were similar for fused DWI and abbreviated MRI (174/194 (89.7%) vs. 184/194 (94.8%), respectively, $P = 0.057$, Reader 1; 174/194 (89.7%) vs. 183/194 (94.3%), respectively, $P = 0.092$, Reader 2). Lesion conspicuity was significantly higher on abbreviated MRI than fused DWI at both readers (9.37 ± 2.24 vs 8.78 ± 3.03, respectively, $P = 0.001$, Reader 1; 9.16 ± 2.32 vs 8.39 ± 2.93, respectively, $P < 0.001$, Reader 2). The κ value for interobserver agreement of index cancer detection was 0.548 ($P < 0.001$) on fused DWI and 0.849 ($P < 0.001$) on abbreviated MRI.

Discussion/Conclusion: Detection of index cancers by fused DWI was similar to that of abbreviated MRI, although lesion conspicuity was significantly better with abbreviated MRI. Our study showed a potential use of fused DWI using unenhanced MRI as an alternative to abbreviated postcontrast-enhanced MRI.

References:

1. Ko ES, Morris EA. Abbreviated Magnetic Resonance Imaging for Breast Cancer Screening: Concept, Early Results, and Considerations. Korean J Radiol. 2019 Apr;20(4):533–541.

2. Shin HJ, Chae EY, Choi WJ, et al. Diagnostic Performance of Fused Diffusion-Weighted Imaging Using Unenhanced or Postcontrast T1-Weighted MR Imaging in Patients With Breast Cancer. Medicine (Baltimore). 2016 Apr;95(17):e3502.

3. Kang JW, Shin HJ, Shin KC, et al. Unenhanced magnetic resonance screening using fused diffusion-weighted imagingand maximum-intensity projection in patients with a personal history of breast cancer: role of fused DWI for postoperative screening. Breast Cancer Res Treat. 2017 Aug;165(1):119–128.

P01.07

Feasibility Study of Visualizing Tree-Rings of Waterlogged Wood by Deep-Learning Reconstruction

M. Mori[1], S. Kuhara[1], K. Kobayashi[1], K. Fukushima[2], T. Yoshioka[2], H. Machida[3], K. Yokoyama[3]

[1]Kyorin University, Department of Medical Radiological Technology, Tokyo, JAPAN, [2]Kyorin University Hospital, Tokyo, JAPAN, [3]Kyorin University, School of Medicine, Department of Radiology, Tokyo, JAPAN

Purpose/Introduction: Recently, the application of magnetic resonance imaging (MRI) to dendroarchaeology has been reported [1], and the development of related technology is expected to be useful as a non-destructive inspection method. Low signal-to-noise ratio (SNR) is one of the challenges for realizing the high-resolution imaging needed for dendroarchaeology. To overcome this problem, multiple averaging is used, and it leads to long scan times. However, a new denoising technology called deep-learning reconstruction (DLR) has been developed and has yielded significant results in the medical-imaging field. In this paper, a study of the feasibility of visualizing tree-rings of waterlogged wood by DLR is presented. We focus on whether the same Neural Network, which is learned with human images, is still useful for denoising and visualizing tree-rings were investigated.

Subjects and Methods: The test sample was made for simulating an excavated wooden material: a fresh cut of Hinoki (*Chamaecyparis obtusa*) was boiled to a deaerated and waterlogged condition. A 3T MRI (Vantage Galan 3T ZGO; Canon Medical Systems Corporation) equipped with a 16-channel phased-array coil was used for obtaining images. The uHR-T2WI sequence [2] was used (spatial resolution: 0.02×0.04 mm^2, slice thickness: 5 mm, field of view (FOV): 3×2 cm^2, matrix: 624×1024, TR/TE: 2000/100 ms) to obtain high-resolution images. The scan was repeatedly performed to cover the whole material by shifting the small FOV. The number of acquisition (NAQ) was changed, and the image quality was compared with images obtained by DLR.

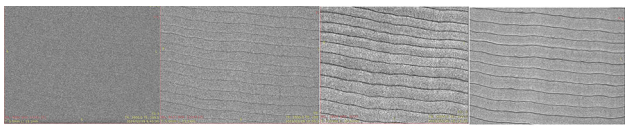

Figure.1 The uHR-T2WI images: (a) NAQ1 (acquisition time, 31:28), (b) NAQ4 (acquisition time, 2:05:52), (c) NAQ4 + DLR, and (d) NAQ16 (8:23:28)

Results:

The tree-rings of a low-SNR image (NAQ1, Acquisition time: 31:28) were hardly visible (Fig. 1a), but could be recognized by NAQ4. However, the tree-rings were still not sufficiently visualized (Fig. 1b). The tree-rings became much clearer by NAQ16 (Fig. 1d) but the acquisition time became approximately 8.5 h. However, by applying DLR to a NAQ4 image (Fig. 1b), the visualization of tree-rings were significantly improved (Fig. 1c), and the image quality became equivalent to or better than that of the NAQ16 image (Fig. 1d), even when the imaging time was one-fourth.

Discussion/Conclusion: A feasibility study of visualizing tree-rings of waterlogged wood was performed by applying DLR to uHR-T2 W image. The results show that DLR had a sufficient reduction effect on the noise of the wood image and significantly improved the image quality with greatly reduced scan time (one-fourth), with the same Neural Network leaned with human images. By using this technology, one can expect to obtain further high-resolution images, or, if the

spatial resolution is the same, the scan time can be significantly shortened. Thus, the imaging of tree-rings by MRI with DLR is expected to be a leading technology for the field of dendroarchaeology.

References:

[1] Magnetic Resonance Imaging 38 (2017), pp196–201
[2] ESMRMB Congress (2017) 30 (Suppl 1), S652

P01.08

Fat content changes in individuals with type 2 diabetes by a combined intervention of digital education, behavioral modification and a calorie-restricted diet

Y. Kupriyanova[1], D. Pesta[1], O. -P. Zaharia[1], T. Van Gemert[1], M. Trenell[2], J. Szendroedi[1], J. -H. Hwang[1], M. Roden[1]

[1]Institute for Clinical Diabetology, German Diabetes Center, Leibniz Institute for Diabetes Research at Heinrich Heine University, Düsseldorf, GERMANY, [2]NIHR Innovation Observatory, Newcastle University, Newcastle Upon Tyne, UK; Changing Health, Newcastle upon Tyne, UNITED KINGDOM

Purpose/Introduction: Digital education, behavioral modification and calorie restriction can improve the metabolic profile of patients with type 2 diabetes mellitus (T2DM). This study aimed at quantitatively monitoring changes in hepatocellular lipid content (HCL) and intramyocellular lipid content (IMCL) using ^{1}H-MRS in patients with T2DM in response to a combined approach using digital education, behavioral modification and real food-based very low calorie (800 kcal/day) diet.

Subjects and Methods: After consenting to the protocols approved by the local institutional review board, eight T2DM patients (males/females = 4/4; age 56 ± 6 years; body mass index (BMI) 31 ± 4 kg/m^2; mean ± SD) underwent ^{1}H-MRS at baseline and after 12 weeks of the intervention, during which the patients received a digital education and behavioral change program along with individual coaching. All MR measurements were performed on a 3-T MR scanner (Achieva X-series, Philips Healthcare). Single voxel STEAM ^{1}H-MRS was performed for quantitative assessment of HCL (TR/TE = 4000/10 ms). Both water suppressed and non-suppressed ^{1}H-MRS were acquired in the identical voxel within the homogeneous part of liver tissue with a volume of interest (VOI) of 25 × 25 × 25 mm^3. For IMCL measurement, water suppressed and non-suppressed ^{1}H-MRS were acquired in a VOI (10 × 10 × 20 mm^3), placed within the tibialis anterior muscle using PRESS sequence (TR/TE = 2000/29 ms). All spectra were processed using jMRUI software [1]. HCL content was quantified by the ratio of signal integrals of fat and total signal (water + fat) and expressed in %. The difference in T2 relaxation times of water and fat peaks was corrected based on a previous publication [2]. IMCL content was calculated from the peak areas of IMCL CH2 (methylene) at 1.3 ppm with respect to the water peak area and was corrected for T1 and T2 relaxation effects according to a previous study [3]. Comparisons of HCL and IMCL contents in pre- and post-intervention were computed using a paired *t* test.

Results: After 12 weeks, body weight, HCL and IMCL had decreased by 9% ($p < 0.01$), by 67% ($p = 0.04$) and by 42% ($p = 0.03$), respectively [Table 1].

	Baseline	12 weeks follow-up	Percentage change (p value)
Body weight [kg]	90 ± 10	82 ± 10	-9% (<0.01)
HCL [%]	9.5 ± 10.1	3.1 ± 3.2	-67% (0.04)
IMCL [%]	0.45 ± 0.2	0.26 ± 0.1	-42% (0.03)

HCL and IMCL content (mean±SD) in T2DM at baseline and after 12 weeks intervention.

Discussion/Conclusion: Non-invasive ^{1}H-MRS allows one to detect changes in HCL and IMCL contents in T2DM and can serve as valuable tool for quantitative, reliable and continuous monitoring of lifestyle interventions in humans.

References:

[1] Naressi A et al., MAGMA, 2001.
[2] Hamilton G et al., NMR Biomed, 2010.
[3] Krssák et al., MAGMA, 2004.

P01.09

Systemic pulse pressure in mild stroke patients is associated with pulsatility of blood vessels in the neck and brain

A. Morgan, M. Stringer, U. Clancy, M. Thrippleton, I. Marshall, J. Wardlaw

University of Edinburgh, Centre for Clinical Brain Sciences, Edinburgh, UNITED KINGDOM

Purpose/Introduction: Cerebral small vessel disease (SVD) a cause of many strokes and dementias [1], with vessel stiffness appearing to play a significant role in the disease. Vessel pulsatility (i.e. temporal variation in blood flow) is one way of expressing this stiffness. Previous studies have investigated blood flow and pulsatility in cranial vessels such as the carotids, jugular veins, and venous sinuses, finding some associations with SVD features, including white matter hyperintensities (WMH), on MRI scans [2, 3].

Subjects and Methods: In the work described here, the cerebral blood flow data from 40 patients with non-disabling stroke was analysed to assess the relationship between systemic pulse pressure (the difference between brachial systolic and diastolic blood pressures; PP) and vessel pulsatility. Phase-contrast MRI (Siemens 3T Prisma) with retrospective peripheral pulse gating was used to examine the internal carotid arteries (ICAs) and vertebral arteries (VAs) (TR/TE: 19.6/5.8 ms, venc: 70 cm/s, 20-channel neck coil), as well as the internal jugular veins (IJVs), superior sagittal sinus (SSS), straight sinus (StS), and transverse sinuses (TSs) (TR/TE: 21.7/6.6 ms, venc: 50 cm/s, 32-channel head coil). In-house Matlab code was used to extract the flow data from the PC-MRI images, and subsequently calculate pulsatility using Gosling's pulsatility index equation [PI = ($flow_{max}$ − $flow_{min}$)/$flow_{mean}$)]. Regression analysis was carried out to test for possible associations between PP and vessel PI.

Results: PP showed significant correlation with the PI values of the ICAs ($R^2 = 0.26$, $p < 0.01$; corrected for age: $R^2 = 0.27$, $p < 0.05$), VAs ($R^2 = 0.19$, $p < 0.01$; $R^2 = 0.19$, $p < 0.05$), and SSS ($R^2 = 0.28$, $p < 0.001$; $R^2 = 0.34$, $p < 0.05$).

Discussion/Conclusion: Previously, increased PP has been shown to be associated with increased ICA PI (measured using Carotid Doppler Ultrasound Imaging), which is associated with WMH burden [3]. It is suggested this may be due to hypertension increasing arterial stiffness, which then leads to WMH over time by exposing the brain's small vessels to higher pulsatility. The analysis done here shows that MRI-acquired PI measurements at different intracranial points also show an association with increased PP. These results support the

notion that intracranial vessel stiffness increases with systemic vessel stiffness, although we do not yet know which comes first.

References:
1. Shi, Y et al. Update on cerebral small vessel disease: a dynamic whole-brain disease. Stroke Vasc. Neurol 2016.
2. Shi, Y et al. Small vessel disease is associated with altered cerebrovascular pulsatility but not resting cerebral blood flow. J Cereb Blood Flow Metab 2018.
3. Aribisala et al. Blood pressure, internal carotid artery flow parameters, and age-related white matter hyperintensities. Hypertension 2014.

P01.10

A setup for multi-parametric MRI of the rat gastrocnemius at 4.7T during effort-related contraction

S. Loubrie, A. Trotier, P. Massot, E. Ribot, S. Miraux, I. Bourdel-Marchasson

RMSB, Bordeaux, FRANCE

Purpose/Introduction: Sarcopenia, which is muscle atrophy due to aging, is not well defined to this day [1]. To deeply characterize this process, MR relaxation times (T1 and T2) can be measured to evaluate muscle function during effort. But, a reproducible contraction is necessary and MR parametric sequences that can be applied during contraction are needed. Animal models can help to develop methodologies to assess these issues.

The purpose of this study is to develop an MRI compatible protocol for rat muscle structure evaluation through multi-parametric MR acquisitions. The aim is to measure quantitative data (T1, T2) in the rat gastrocnemius during effort.

Subjects and Methods: A setup [FreeCAD software and 3D printed (FormLabs, Form 2, France)] was developed to fit inside a standard 8 cm-∅ transmit coil and so that the rat gastrocnemius and the receive coil (Miniflex, RAPID Biomedical) would always be located at the center of the magnet. The muscle is electro-stimulated at 3 Hz due to electrodes placed at the heel and knee levels to fully excite the muscle (Figure 1a). We developed an electronic card linked to a microprocessor in order to synchronize the MR acquisitions with the electrostimulation.

To perform T1 measurements, we developed a radial encoded 2D Look-Locker sequence with readouts triggered by the stimulus (Figure 1b). The following parameters were used : TR/TE = 4/1 ms; Time between two inversions, 8 s; Inversion pulse, sech 10 ms; matrix 128 × 128; FOV 30 × 30 mm^2; slice thickness = 1.2 mm.

To perform T2 measurements, we developed a « segmented » 2D spin-echo sequence that is triggered by the stimulus (Figure 1c). The following parameters were used: TR/TE = 5000/3.5 ms; 30 echo images; 90° RF pulse, hermite 1 ms; refocusing pulse, hermite 1.5 ms; matrix 96 × 64; FOV 25 × 20 mm^2; slice thickness = 1 mm.

Phantoms containing vials of different gadolinium or manganese concentrations were created for T1 or T2 measurements, respectively. Four Wistar rats (Janvier Labs, 200 g) were imaged on a Bruker small-animal 4.7T scanner.

Results: In vitro experiments enabled to determine the optimal parameters for accurate relaxation times measurements: 8 projections per Ti and 128 projections per k-space for T1 measurements in 2min08 s and 3 segments of 10 echos for T2 measurements in 16 min. T1 and T2 were then measured on the static muscle: 1360 ± 90 ms and 27.4 ± 2.0 ms, respectively. During the contraction, T1 got longer (1420 ± 105 ms). Due to motion, T2 values using a single segment were inhomogeneous. On the contrary, segmenting the readout in 3 enabled to precisely mesure T2 of 29.5 ± 2.6 ms (Figures 2, 3).

Discussion/Conclusion: We developed a new MRI-compatible setup for muscle exploration in rats. T1 and T2 values lengthens with effort, which is in accordance with literature. Next experiments will be performed on old rats to quantitatively assess sarcopenia.

References:
[1] "Sarcopenia: revised European consensus on definition and diagnosis" Cruz-Jentoft et al. 2018

P01.11

Fast field cycling-NMR relaxometry: an emerging biomarkers of cancer invasion

M. Leclercq[1], L. Broche[2], M. Petit[1], F. Berger[1], **H. Lahrech**[1]

[1]INSERM, BrainTech Lab INSERM U1205 Faculté de Médecine et de Pharmacie de Grenoble, Grenoble, FRANCE, [2]University of Aberdeen Foresterhill Aberdeen, Bio-Medical Physics School of Medicine, Medical Sciences and Nutrition, Aberdeen, UNITED KINGDOM

Purpose/Introduction: T_1-dispersion curves of different glioma models were obtained by FFC-NMR relaxometry. Here parameters derived from mathematical models applied to T_1-dispersion curves were compared to identify FFC-NMR biomarkers for glioma invasion diagnostic, which remains challenging in any medical imaging.

Subjects and Methods: Animal procedures were approved by French/European laws (C3818510003 license). 3 glioma mouse models were studied, the U87 a solid glioma model, and the Glio6 and Glio96 models of tumour cell migration/invasion, both derived from human stem cells, developed in our lab. The Glio6 and Glio96 were validated as migration/invasion[1] and invasion models, respectively. Human glioma cells (5.10^5 in 5 µl PBS) were injected in nude mice in the right caudate nucleus. After, the tumor growth, brains were removed and glioma extracted (30–210 mg) and stored at − 80 °C. FFC-NMR were performed at 37 °C with a Stelar SpinMaster relaxometer. The magnetization polarization was built up at 0.8T and T_1 relaxation occurs during t^E (at 30 variable B_0^E in [0.2mT–0.5T]). For each B_0^E, 12 t^E values were used to describe T_1 relaxation. Quadrupolar peaks (QPs) that result from ^{14}N-^1H interactions were acquired around 58.7mT (n = 30). Relaxation rate $R_1 = 1/T_1$ versus ^1H Larmor frequency $\nu_0 = \gamma/2\pi B_0^E$ were plotted.

Power model[2] (Eq. 1) and Lorentzian model[3] (Eq. 2) were fitted T_1-dispersion curves. QP peak were modeled according to[4] (Eq.2). All the models and statistics (Kruskal–Wallis test) were achieved under MATLAB

Results: In Fig. 1 the mean R_1-dispersion curves of Glio6, Glio96 and U87 glioma are presented. At low magnetic fields, invasive glioma is well separated from the solid one. In Fig. 2, three biomarkers are selected: b (power model) and correlation times $\mathbf{t_s, t_i, t_f}$ (Lorentzian model) related to water dynamics, all found shorter in case of invasion, having therefore rapid dynamics. And the QP amplitude A, sensitive to immobilized proteins, found lower in invasion case. Clearly, these 3 parameters discriminate invasive glioma cells from solid tumor.

Discussion/Conclusion: Peritumoural regions invaded by infiltrative glioma cells are not adequately and sufficiently early diagnosed by MRI or any current medical imaging method. This study highlights the interest of low magnetic fields accessible by FFC NMR/MRI to discriminate tissue of infiltrative glioma cells from solid tumors. Similar results were observed in human resections highlighting the

interest to develop FFC-MRI for clinical investigations which is under development at Aberdeen

References:

[1]Gimenez U and al. NMR in Biomed 2016.
[2]Kimmich R and al. Prog Nucl Magn Reson Spect 2004.
[3]Bertini I, and al. Reson. Chem (2000).
[4]Fries PH and al. J Chem Phys 2015.

P01.12

In vivo liver pH in eNOS$^{-/-}$ mice model fed with High Fat Diet may provide clues to understand their susceptible to develop NAFLD

A. Xavier[1], T. Eykyn[2], B. Plaza[2], A. Phinikaridou[2], M. Andia[1]

[1]*Pontificia Universidad Catolica de Chile, Biomedical Imaging Center, Santiago, CHILE,* [2]*King's College London, School of biomedical engineering and imaging sciences, London, UNITED KINGDOM*

Purpose/Introduction: Mice are very resistant to develop fatty liver diseases, however the eNOS$^{-/-}$ mice have a high susceptibility to develop this condition when fed with high-fat diet [1]. In this model, the NAFLD conditions is developed in concomitance with a metabolic syndrome that include type 2 diabetes and hypertension, very similar to the same condition in humans[2].

In this work we studied the progression of this disease from the metabolic point-of-view using an in vivo phosphorus NMR at 9.4T.

Subjects and Methods: A group of male C57BL/6 wild type mice (n = 6) and eNOS$^{-/-}$ (n = 6) were fed with a high-fat diet for 8 weeks. A control group of wild type mice (n = 5) and eNOS$^{-/-}$ mice (n = 5) were fed with a chow diet for 8 weeks. Mice were scanned in a 9.4T Bruker MR equipment at week 8.

To obtain the phosphorus spectra we used the ISIS sequence TR = 2000 ms; Averages = 32; Voxel Size = 4.7 × 6.5 × 11.8 mm^3; BW/points = 8000 Hz/2048. To obtain the proton spectra and quantify the fat fraction we used a Zg sequence with TR = 3.45 s; BW = 5597 Hz; NSA = 64; flip angle = 90.

All the spectra were processed using TopSpin V6.0. The distance between *Pi* peak and αATP peak was measured. The pH was calculated by the Eqs. 1 and 2 proposed by Rata 2013[3].

$$pH = 6.75 + log10\ (\delta\text{-}3.27/5.69\text{-}\delta) \quad (1)$$

$$\delta = FPi\text{-}F\alpha ATP\text{-}7.56 \quad (2)$$

Results: Figure 1 shows the voxel position for the phosphorus spectra.

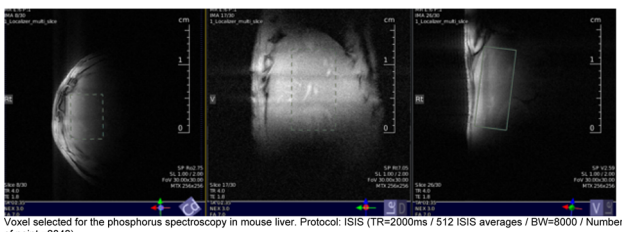

Voxel selected for the phosphorus spectroscopy in mouse liver. Protocol: ISIS (TR=2000ms / 512 ISIS averages / BW=8000 / Number of point =2048)

Figure 2 shows the difference between the eNOS spectra and WT spectra concerning the distance between P_i peak and αATP peak.

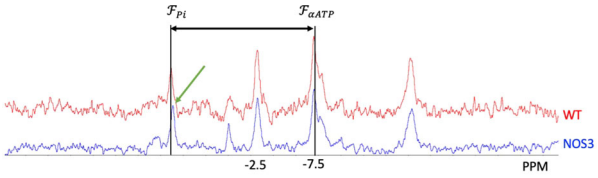

Phosphorus spectra showing the Pi and ATPs peaks. The red spectra correspond to wild type group and the blue spectra, eNOS-/-. The Pi peak is slightly shifted to the right in the eNOS-/- spectra (green arrow).

Figure 3a shows the fat accumulation in the liver in the eNOS$^{-/-}$ mice fed with chow and HFD compare with the controls. With 8 weeks of high fat diet, the eNOS$^{-/-}$ mice accumulates significantly more fat in the liver compared to the other groups.

Figure 3b shows the liver pH of the WT mice and eNOS$^{-/-}$ with a chow diet. eNOS$^{-/-}$ mice show an acidic liver compared with the WT mice.

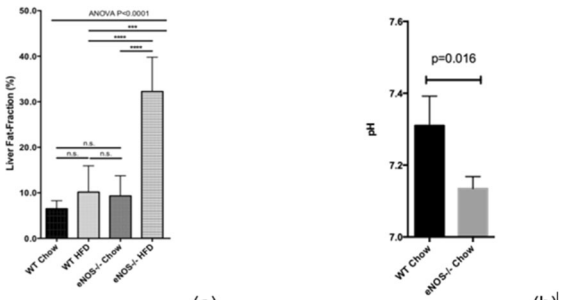

(a)Fat fraction in the mice liver eNOS -/- model with 8 weeks of high fat diet. (b) pH of a WT mice and eNOS-/- with a chow diet

Discussion/Conclusion: We analyzed the liver pH in vivo in eNOS$^{-/-}$ mice fed with normal diet trying to understand the mechanism of the eNOS$^{-/-}$ susceptibility to develop NAFLD.

NO regulates AMPK so its absence leads to decreased AMPK activity. A decrease in AMPK activity reduces H+ pumped out of the cell, therefore results in an increase in intracellular [H+] which could explain the decreased pH we observed by ^{31}P in the eNOS$^{-/-}$ mice. This reduced AMPK activity also implicates in obesity, inflammation, fat accumulation in the liver and diabetes[4].

This study proved to be useful in measuring the pH of mice liver and correlating it with the fat accumulation.

References:

[1]Sheldon RD, J Appl Physiol 2014 [2]Takahashi T, J Diabetes Res 2014; [3]Rata et al. NMR in Biom. 2013. [4] smith et al. Am J Physiol Endocrinol Metab. 2016.

This publication has received funding from Millenium Science Initiative of the Ministry of Economy, Development and Tourism, grant Nucleus for Cardiovascular Magnetic Resonance. CONICYT-PCHA/Doctorado Nacional/2016-21160835 and FONDECYT 1180525.

P01.13

Biliary confluence types distribution in hilar cholangiocarcinoma patients: what are the causes for more uncommon types?

M. Shorikov, O. Sergeeva, D. Frantsev, M. Lapteva, E. Virshke, B. Dolgushin

N.N. Blokhin RCRC, Radiology, Moscow, RUSSIAN FEDERATION

Purpose/Introduction: The purpose of the study is to compare biliary confluence type distributions in hilar cholangiocarcinoma patients and in those with unremarkable bile ducts.

Subjects and Methods: 203 Klatskin tumor patients and 204 patients with unremarkable bile ducts were enrolled in the study. All the patients underwent abdominal MRI including MR-cholangiopancreatography; percutaneous transhepatic cholangiography was additionally performed in 141 study group patients. Biliary anatomy variants were arranged according Nakamura bile duct confluence classification [1] by two radiologists: Cohen's kappa = 0.7 in study group and 0.9 in control, differences were resolved by consensus. Anatomical variations in right sectoral bile ducts confluence according to Nakamura: type I right posterior hepatic duct converges with right anterior hepatic duct, type II: right posterior hepatic duct converges with right anterior and left hepatic ducts, type III: right posterior hepatic duct converges with common hepatic duct, type IV: right posterior hepatic duct converges with left hepatic duct, type V: non of the above. Groups dissimilarities were evaluated with Chi-square and Pearson exact test criteria, p = 0.05 was considered statistically significant.

Results: In study group, type I,II,III,IV,V confluences were observed in 27.6%, 22.2%, 1.5%, 36.0% and 2.4% of cases, respectively. In control group, confluence type distribution was close to the one described in general population[1]:I,II,III,IV,V confluences were presented in 75.0%, 9.3%, 0.5%, 14.2% and 1.0% of patients, respectively. Differences between groups were statistically significant ($p < 0.001$).

Discussion/Conclusion:

(1) Uncommon biliary confluence types are overrepresented in Klatskin tumor patients

(2) Assuming tumor onset probability proportional to duct surface area (ps = probability/surface) and taking into account Murray's law [2]:

$pI = ps \times \pi \times l \times (2 \times d_h + 1.25 \times d_h) = 3.25 \times ps \times \pi \times l$ − tumor onset probability for confluence type I,

$pII = ps \times \pi \times l \times (d_h + 0.8 \times 2 \times d_h + 1.25 \times d_h) = 3.85 \times d_h \times ps \times \pi \times l$ − type II,

pIII, IV = pII + $0.8 \times d_h \times$ руд $\times \pi \times a$ − type III, IV; d_h—hepatic duct diameter, l—duct length, a—additional duct length in types III, IV

$pI < pII, III, IV$

(3) 3. Assuming lamilar flow in bile ducts, taking into account Murray's law and parallel duct junction tube resistance is no less than 1.25 times higher in uncommon confluence types thus pressure in confluence in II, III, IV types is higher than in Ist type, higher pressure is shown to be a malignisation factor for cholangiocarcinoma in animal studies [3]

References:

1. Nakamura T., et al. Anatomical variations and surgical strategies in right lobe living donor liver transplantation: lessons from 120 cases. *Transplantation* 2002; 73(12).
2. Zheng X., et al. Bio-inspired Murray materials for mass transfer and activity. *Nat. Comm.* 2017; 8: 14921.
3. Cadamuro M., et al. Animal models of cholangiocarcinoma: What they teach us about the human disease.*Clin. Res. Hepatol. Gastroenterol*. 2018; 42(5).

P01.14

Breast dynamic contrast-enhanced MR imaging detected additional nodule: correlation with kinetic features using computer-aided diagnosis and histopathology

S. Y. Nam[1], E. Y. Yoo[1], M. J. Hong[1], H. K. Park[2]

[1]*Gil Medical Center, Gachon University College of Medicine, Radiology, Incheon, SOUTH KOREA,* [2]*Gil Medical Center, Gachon University College of Medicine, Surgery, Incheon, SOUTH KOREA*

Purpose/Introduction: To evaluate whether preoperative breast dynamic contrast-enhanced (DCE) magnetic resonance (MR) imaging kinetic features, assessed using computer-aided diagnosis (CAD), is useful to predict malignancy and tumor biology in MR detected additional nodule in patients with breast cancer.

Subjects and Methods: Between August and December 2018, 66 consecutive women (mean age 54.9 years; range 33–77 years) who underwent preoperative DCE breast MR imaging for breast cancer, with CAD data, were identified. The tumor size and kinetic parameters (initial peak enhancement, the proportion of early phase medium and rapid enhancement, and the proportion of delayed phase persistent, plateau, and washout enhancement) were measured with CAD system on DCE MR Images. The peak signal intensity and kinetic enhancement profiles were compared with the clinical and histopathologic features.

Results: There were 66 MR-detected additional nodules, including 28 benign nodules and 38 malignant nodules. Univariate and multivariate analysis revealed that a higher peak enhancement ($P = 0.034$) and a higher proportion of washout component ($P = 0.002$) on DCE MR imaging were associated with a malignancy.

Discussion/Conclusion: Higher peak enhancement and higher washout component on DCE MR Images assessed with CAD were independent parameters of predicting malignancy in MR detected additional nodule. Peak enhancement and volumetric analysis of kinetic patterns were useful for predicting malignancy in MR detected additional nodule.

References:

1. Yi A, Cho N, Im SA, Chang JM, Kim SJ, Moon HG, et al. Survival outcomes of breast cancer patients who receive neoadjuvant chemotherapy: association with dynamic contrast-enhanced MR imaging with computer-aided evaluation. Radiology. 2013;268(3):662–72.
2. Loiselle CR, Eby PR, DeMartini WB, Peacock S, Bittner N, Lehman CD, et al. Dynamic contrast-enhanced MRI kinetics of invasive breast cancer: a potential prognostic marker for radiation therapy. International journal of radiation oncology, biology, physics. 2010;76(5):1314–9.
3. Song SE, Cho KR, Seo BK, Woo OH, Jung SP, Sung DJ. Kinetic Features of Invasive Breast Cancers on Computer-Aided Diagnosis Using 3T MRI Data: Correlation with Clinical and Pathologic Prognostic Factors. Korean J Radiol. 2019 Mar;20(3):411-421.
4. Bhooshan N, Giger ML, Jansen SA, Li H, Lan L, Newstead GM. Cancerous breast lesions on dynamic contrast-enhanced MR images: computerized characterization for image-based prognostic markers. Radiology. 2010;254(3):680–90.
5. Meeuwis C, van de Ven SM, Stapper G, Fernandez Gallardo AM, van den Bosch MA, Mali WP, et al. Computer-aided detection (CAD) for breast MRI: evaluation of efficacy at 3.0 T. European radiology. 2010;20(3):522–8.
6. Song SE, Cho N, Han WS. Post-clip placement MRI following second-look US-guiede core biopsy for suspicious lesions identified on breast MRI. Eur Radiol. 2017; 27: 5196-5203.

P01.15
Use of DWI and ADC in gastric cancer staging

L. Soydan[1], A. A. Demir[2], M. Torun[3], M. Arar[4]

[1]Haydarpasa Numune Education and Research Hospital, Radiology, Istanbul, TURKEY, [2]Haseki Education and Research Hospital, Radiology, Istanbul, TURKEY, [3]Haydarpasa Numune Education and Research Hospital, General Surgery, Istanbul, TURKEY, [4]Haydarpasa Numune Education and Research Hospital, Pathology, Istanbul, TURKEY

Purpose/Introduction: Gastric cancer (GC) has a poor prognosis, especially in advanced stage (1). Presurgical clinical staging is therefore important in planning the extent of surgery. In this study we investigated the diagnostic role of Diffusion-weighted Imaging (DWI) and its quantitative parameter Apparent Diffusion Coefficient (ADC) in staging of GC based on the 8th edition of AJCC classification (2–5).

Subjects and Methods: Forty-six patients with non-metastatic biopsy-proven GC who underwent abdominal MRI with DWI before surgery were included in this retrospective study. Tumor invasion depth (T stage) and nodal involvement (N stage) was evaluated using signal increase on DWI and tumor ADC was measured. Diagnostic performance of these results were assessed by comparing with post-surgical histopathology based on 8th TNM classification.

Results: Sensitivity, specifity and accuracy of DWI in T-staging are 92.1%, 75%, 89.1% for $\leq$ T2 vs $\geq$ T3 and 75%, 88.5%, 82.6% for $\leq$ T3 vs T4, whereas in N-staging 89.3%, 88.9%, 89.1% for $\leq$ N1 vs $\geq$ N2 and 73.7%, 96.3%, 86.9% for $\leq$ N2 vs N3, respectively.

Relative preoperative ADC values correlated with pT staging ($r = -0.397$, $p = 0.006$). There was also a statistically significant difference of relative ADC values between $\leq$ T3 and T4 stages and a cutoff of 0.64 s/mm^2 could distinguish between these stages with an odds ratio of 7.714 (95% CI 1.479–40.243). The area under the receiver operating characteristic (ROC) curve for differentiating $\leq$ T3 and T4 stages was 0.725.

Table 1: Patient Characteristics

		n (%)
Segment	**Distal**	17 (37,0)
	Cardia	14 (30,4)
	Corpus	15 (32,6)
Histological Type	**Poor diff adenoca**	6 (13,0)
	Mod diff adenoca	12 (26,1)
	Well diff adenoca	3 (6,5)
	Mixed adenoca	5 (10,9)
	Mucinous adenoca	3 (6,5)
	Undiff adeno	1 (2,2)
	PCC	12 (26,1)
	Manec	2 (4,3)
	GIST	2 (4,3)
Lauren (n=44)	**Diffuse**	14 (31,8)
	İntestinal	25 (56,8)
	Mixed	5 (11,4)
Grade	**Grade 1**	3 (6,5)
	Grade 2	14 (30,4)
	Grade 3	29 (63,1)
c-erbB-2 (HER-2)	**Negative**	39 (84,8)
	Pozitive	7 (15,2)
LNR	*Min-Max (Median)*	0-1 (0,2)
	Mean±SD	0,26±0,29
ADC	*Min-Max (Median)*	0,61-2,17 (1,2)
	Mean±SD	1,23±0,36
Gastric wall	*Min-Max (Median)*	1,33-2,94 (2,2)
	Mean±SD	2,25±0,39
Relative ADC	*Min-Max (Median)*	0,28-0,92 (0,5)
	Mean±SD	0,56±0,17
Perigastric LAP (mm)	*Min-Max (Median)*	0-25 (10,5)
	Mean±SD	9,35±6,70
N stage	**N0**	12 (26,1)
	N1	7 (15,2)
	N2	12 (26,1)
	N3	15 (32,6)
T stage	**T1-T2**	9 (19,6)
	T3	19 (41,3)
	T4	18 (39,1)
pT stage	**pT1**	4 (8,7)
	pT2	4 (8,7)
	pT3	18 (39,1)
	pT4	20 (43,5)
pN stage	**pN0**	14 (30,4)
	pN1	4 (8,7)
	pN2	9 (19,6)
	pN3	19 (41,3)

Diff: Differentiated ; PCC: Poorly Cohesive Carcinoma ; Adenoca: Adenocarcinoma; Manec: Mixed Adenoneuroendocrine Carcinoma; GIST: Gastrointestinal Stromal Tumor; LNR: Lymph Node Ratio; Relative ADC: Mean tumor ADC/Mean ADC of normal appearing gastric wall; LAP: Lymphadenopathy ; HER-2: Human epidermal growth factor receptor 2 ; p: pathological

Table 2

			Absolute ADC	Relative ADC
c-erbB-2	Negative	Min-Max (Median)	0,61-2,17 (1,16)	0,28-0,92 (0,5)
	(n=39)	Mean±SD	1,23±0,38	0,55±0,18
	Positive	Min-Max (Median)	0,97-1,54 (1,17)	0,46-0,85 (0,56)
	(n=7)	Mean±SD	1,26±0,24	0,62±0,15
		*a*p*	***0,511***	***0,204***
Lauren	Diffuse	Min-Max (Median)	0,75-1,54 (1)	0,36-0,74 (0,48)
	(n=14)	Mean±SD	1,06±0,24	0,51±0,11
	Intestinal	Min-Max (Median)	0,61-2,17 (1,16)	0,28-0,92 (0,56)
	(n=25)	Mean±SD	1,29±0,38	0,59±0,20
	Mixed	Min-Max (Median)	0,9-2,01 (1,37)	0,34-0,8 (0,56)
	(n=5)	Mean±SD	1,43±0,46	0,59±0,18
		*b*p*	***0,103***	***0,498***
pT stage	T1-T2-T3	Min-Max (Median)	0,75-2,17 (1,19)	0,35-0,92 (0,59)
	(n=26)	Mean±SD	1,32±0,40	0,62±0,18
	T4	Min-Max (Median)	0,61-1,76 (1,13)	0,28-0,78 (0,45)
	(n=20)	Mean±SD	1,12±0,28	0,48±0,14
		*c*p*	***0,070***	***0,006****
pT stage	T1-T2	Min-Max (Median)	0,88-2,17 (1,37)	0,35-0,92 (0,66)
	(n=8)	Mean±SD	1,45±0,56	0,65±0,22
	T3-T4	Min-Max (Median)	0,61-2,08 (1,16)	0,28-0,88 (0,51)
	(n=38)	Mean±SD	1,19±0,29	0,54±0,16
		*a*p*	***0,496***	***0,164***
pN stage	N0-N1-N2	Min-Max (Median)	0,78-2,17 (1,21)	0,34-0,92 (0,55)
	(n=27)	Mean±SD	1,30±0,39	0,60±0,19
	N3	Min-Max (Median)	0,61-1,76 (1,1)	0,28-0,74 (0,48)
	(n=19)	Mean±SD	1,13±0,28	0,50±0,14
		*c*p*	***0,106***	***0,051***
pN stage	N0-N1	Min-Max (Median)	0,88-2,17 (1,22)	0,34-0,92 (0,53)
	(n=18)	Mean±SD	1,36±0,43	0,61±0,20
	N2-N3	Min-Max (Median)	0,61-1,76 (1,13)	0,28-0,85 (0,5)
	(n=28)	Mean±SD	1,15±0,28	0,53±0,15
		*c*p*	***0,081***	***0,154***
Grade	Grade 1+2	Min-Max (Median)	0,93-2,17 (1,15)	0,35-0,92 (0,55)
	(n=17)	Mean±SD	1,33±0,41	0,59±0,19
	Grade 3	Min-Max (Median)	0,61-2,01 (1,16)	0,28-0,85 (0,51)
	(n=29)	Mean±SD	1,17±0,32	0,54±0,16
		*c*p*	***0,150***	***0,351***

*a*Mann Whitney U Test* *b*Kruskal Wallis Test* *c*Student t Test* ***p<0.01*

Table 3: Diagnostic performance of DWI for TN staging of GC

TN staging	*Sensitivity*	*Specificity*	*PPV*	*NPV*	*Accuracy*
≤ T2 vs ≥ T3	92.1	75..0	94.6	66.7	89.1
≤ T3 vs T4	75.0	88.5	83.3	82.1	82.6
≤N1 vs ≥N2	89.3	88.9	92.6	84.2	89.1
≤N2 vs N3	73.7	96.3	93.3	83.9	87.0

McNemar Test, Numbers given in %,

PPV: Positive Predictive Value ; NPV: Negative Predictive Value

Discussion/Conclusion: DWI may be used in preoperative TN staging of preoperative non-metastatic GC. Relative ADC may help distinguish advanced T stages (T4) from less advanced stages of GC.

References:

(1) F. Kamangar, G.M. Dores, W.F. Anderson, Patterns of cancer incidence, mortality, and prevalence across five continents: defining priorities to reduce cancer disparities in different geographic regions of the world. J. Clin Oncol: Offic. J. Am. Soci. Clin. Oncol. 24 (2006) 2137e2150.

(2) M.B. Amin, S. Edeg, D.R. Byrd, et al., AJCC Cancer Staging Manual, SpringerVerlag, New York, 2016.

(3) M.B. Amin, F.L. Greene, S.B. Edge, et al., The Eighth Edition AJCC Cancer Staging Manual: continuing to build a bridge from a population-based to a more "personalized" approach to cancer staging. CA A Canc. J. Clin. 67 (2017) 93e99.

(4) Giganti F, Tang L, et al., Gastric cancer and imaging biomarkers: Part 1—a critical review of DW-MRI and CE-MDCT findings. Eur Radiol. 2019 Apr;29(4):1743–1753.

(5) Liu S, Wang H et al., Preoperative apparent diffusion coefficient value of gastric cancer by diffusion-weighted imaging: Correlations with postoperative TNM staging. J Magn Reson Imaging. 2015 Sep;42(3):837–43.

P01.16

The effects of chronic stress in mice bearing B16F10 melanoma cell line and it's role in angiogenesis

A. Barbieri[1], N. Raiano[2], A. Luciano[1], D. Rea[1], R. Fusco[2], C. Raiano[2], V. Granata[2], A. Petrillo[2], C. Arra[3]

[1]IRCCS Istituto Nazionale Tumori Fondazione G.Pascale, Research, Naples, ITALY, [2]IRCCS Istituto Nazionale Tumori Fondazione G.Pascale, Radiology, Naples, ITALY, [3]IRCCS Istituto Nazionale Tumori Fondazione G.Pascale, Research, Naples, ITALY

Purpose/Introduction: Accumulating evidences suggest that chronic stress can be a cofactor for the initiation and progression of cancer. Here we evaluated the role of endothelial nitric oxide synthase (eNOS) in stress-promoted tumour growth of murine B16F10 melanoma cell line in C57BL/6 mice.

Subjects and Methods: Animals subjected to restraint stress showed increased levels adrenocorticotropic hormone, enlarged adrenal glands, reduced thymus weight and a 3.61-fold increase in tumour growth respect to no-stressed animals Fig 1. Mice were subjected to magnetic resonance imaging (MRI) at 1.5 T and a phased array coil for tumor growth evaluation and infiltration.

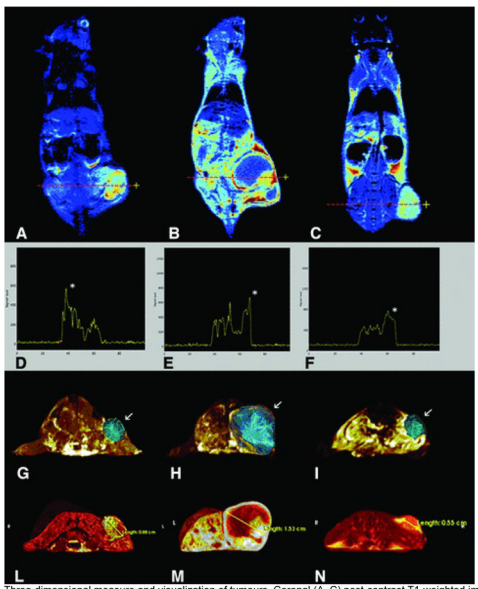

Three-dimensional measure and visualization of tumours. Coronal (A–C) post-contrast T1-weighted images (T1-w), applying intensity colouring maps of stressed + PpI (A), stressed + placebo (B) and placebo (C).

Results: Tumour growth as also highlighted was significantly reduced in mice treated with the β-antagonist propranolol. Tumour samples obtained from stressed mice displayed high levels of vascular endothelial growth factor (VEGF) protein in immunohistochemistry Fig 2.

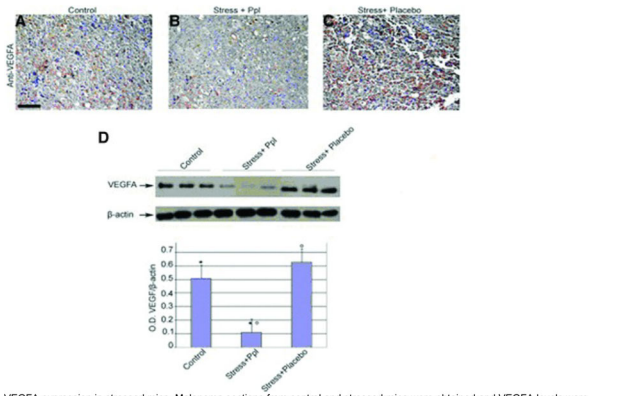

VEGFA expression in stressed mice. Melanoma sections from control and stressed mice were obtained and VEGFA levels were analysed by IHC.Densitometry analysis was obtained from samples of two separate experiments. Scale bar: 100 μm in A–C. Ppl: propra

Because VEGF can induce eNOS increase, and nitric oxide is a relevant factor in angiogenesis, we assessed the levels of eNOS protein by Western blot analysis. We found a significant increase in eNOS levels in tumour samples from stressed mice, indicating an involvement of this enzyme in stress-induced tumour growth Fig 3.

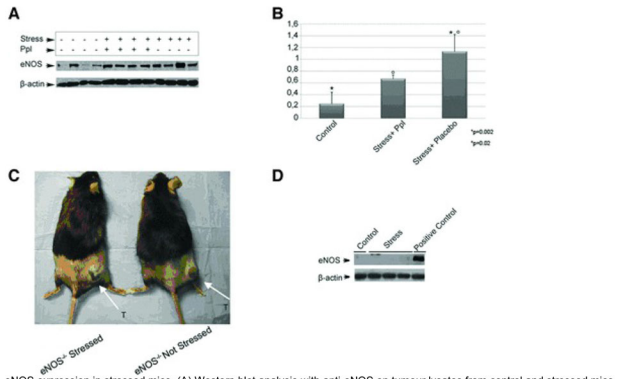

eNOS expression in stressed mice. (A) Western blot analysis with anti-eNOS on tumour lysates from control and stressed mice revealed an increased level of eNOS in stressed + placebo mice compared to control; **P= 0.02 and stressed + Ppl mice; *P= 0.0

Discussion/Conclusion: Accordingly, chronic stress did not promote tumour growth in eNOS *knockout* mice. These results disclose for the first time a pivotal role for eNOS in chronic stress-induced initiation and promotion of tumour growth.

References:

1. Dhabhar FS, McEwen BS. Acute stress enhances while chronic stress suppresses cell-mediated immunity in vivo: a potential role for leukocyte trafficking. Brain Behav Immun. 1997; 11: 286–306.
2. Montoro J, Mullol J, Jauregui I, et al. Stress and allergy. J Investig Allergol Clin Immunol. 2009; 19: 40–7.
3. Vere CC, Streba CT, Streba LM, et al. Psychosocial stress and liver disease status. World J Gastroenterol. 2009; 15: 2980–6.
4. Antoni MH, Lutgendorf SK, Cole SW, et al. The influence of bio-behavioural factors on tumour biology: pathways and mechanisms. Nat Rev Cancer. 2006; 6: 240–8.
5. Chida Y, Hamer M, Wardle J, et al. Do stress-related psychosocial factors contribute to cancer incidence and survival? Nat Clin Pract Oncol. 2008; 5: 466–75.
6. Desaive P, Ronson A. Stress spectrum disorders in oncology. Curr Opin Oncol. 2008; 20: 378–85.
7. Reiche EM, Nunes SO, Morimoto HK. Stress, depression, the immune system, and cancer. Lancet Oncol. 2004; 5: 617–25.
8. Thaker PH, Han LY, Kamat AA, et al. Chronic stress promotes tumour growth and angiogenesis in a mouse model of ovarian carcinoma. Nat Med. 2006; 12: 939–44.
9. Ignarro LJ. Nitric oxide as a unique signaling molecule in the vascular system: a historical overview. J Physiol Pharmacol. 2002; 53: 503–14.

P01.17

Non-contrast MR-angiography for blood circulation studies in patients with pelvic congestion syndrome

M. Tatarinova[1], K. Sevostyanova[2], A. Tulupov[3], O. Bogomyakova[3], A. Savelov[3]

[1]Novosibirsk State University; 630090, Novosibirsk, st. Pirogov, 2, Новосибирск, RUSSIAN FEDERATION, [2]Institute of Chemical Biology and Fundamental Medicine of the Russian Academy of Sciences; 630090, Novosibirsk, Academician Lavrentyev Avenue, 8, Novosibirsk, RUSSIAN FEDERATION, [3]The Institute International Tomography Center of the Russian Academy of Sciences; 630090, Novosibirsk, st. Institutskaya 3A, Novosibirsk, RUSSIAN FEDERATION

Purpose/Introduction: Despite the fairly widespread prevalence of varicose veins of pelvis among women of reproductive age, the diagnosis of this pathology remains fairly stable [1]. In this paper, we studied some qualitative and quantitative characteristics of the venous circulation in the pelvic area in women with varicose veins using the phase-contrast MRI method [2], that have diagnostic value and contribution in understanding the pathogenesis of this pathology.

Objective: to study the venous blood circulation in the pelvic area by MRI in women with pelvic varicose veins.

Subjects and Methods: The 1.5 T MRI scanner « Achieva » (Philips) was used in this study. The 30 patients with primary and secondary pelvic congestion syndrome according to ultrasound examination were involved in this study. The study was performed with a routine protocol MRI for pelvis and abdomen, including of T1- and T2-weighted images and STIR. The non-contrast 3D MR-angiography of the vessels and Quantitative Flow (Q-Flow) phase contrast technique were used for a detailed study of quantitative parameters of venous blood flow in the inferior vena cava, common iliac and gonadal veins. The quantitative data were processed using nonparametric statistical analysis.

Results: It was shown that in patients with varicose pelvic disease, the bilateral gonadal vein enlargement (43.3%) or the expansion of the left gonadal vein (36.6%) is observed. It was found that the diameter of the gonadal veins cannot be a criterion for the presence of reflux in these veins ($p < 0.05$). In the study group, the most frequent anatomical factor of VBMT is a May-Turner syndrome (23.1%). Patients with the May-Turner syndrome showed a 1.5-fold decrease in peak velocity along the left common iliac vein ($p < 0.05$) and a compensatory bilateral gonadal vein enlargement with no reflux in the left gonad veins ($p < 0.05$). In patients without the MayTurner syndrome, a retrograde blood flow is detected in the left gonadal veins ($p < 0.05$).

Discussion/Conclusion: Qualitative and quantitative data of this study provide additional information on the hemodynamics of the pelvic venous system in women with pelvic varicose disease, which can be used to diagnose and plan therapy in patients with this pathology.

The work was supported by Russian Science Foundation (the project #19-75- 20093) for works of MRI and grant of the Russian Foundation for Basic Research (project #19-015-00488) regarding theoretical and clinical part.

References:
1. Arnoldussen C.W., de Wolf M.A., Wittens C.H. Diagnostic imaging of pelvic congestion syndrome.//The Journal of Venous Disease. 2015, Vol. 30, P. 67–72.
2. Lotz J., Meier C., Leppert A., Galanski M. Cardiovascular Flow Measurement with Phase-Contrast MR Imaging: Basic Facts and Implementation.//RadioGraphics. 2002, Vol. 22, P. 651–671.

P01.18

A comparative VBM study of longitudinal neuroanatomical changes in AD transgenic mouse models

M. Blūma[1], E. Micotti[2], D. Tolomeo[2], G. Forloni[2], C. Babiloni[1]

[1]*Sapienza University of Rome, Department of Physiology and Pharmacology "Vittorio Erspamer", Rome, ITALY,* [2]*IRCCS Institute for Pharmacological Research "Mario Negri", Neuroscience, Milan, ITALY*

Purpose/Introduction: Neurodegeneration and signs of atrophy in brain areas such as the hippocampus and entorhinal cortex are typical for Alzheimer's disease (AD). To various extents, available transgenic (TG) mouse models of AD recapitulate such hallmarks of the disease as amyloid and tangle pathology, cognitive impairment, synaptic and neuronal loss. Less is known, however, about the brain volumetric changes over time in different genetic strains. Voxel-based morphometry (VBM) of structural MRIs is an in vivo method used to study subtle volumetric changes over time in the whole brain longitudinally. Although it has been seldom used in mice, recent developments in automated image analysis algorithms made it a bridgeable gap.
Subjects and Methods: In this study, we compared the progression of neurodegeneration in double (TASTPM; amyloid+ at 6 m; tangle−) and triple (TAUPS2APP amyloid+ ; tangle+ ; both at 4 m) TG strains of AD with a longitudinal design. Control (C67/BL6), TG (TASTPM and TAUPS2APP) male and female mice received MRI scan at 4 m, 13 m, and 24 m; (N ≈ 10–20 mice per group). Data-preprocessing was performed with toolkits from the AFNI, FMRIB, and ANTs software libraries; the statistical analysis—in SPM12 and the read-out of anatomical labels—in ITK-snap.

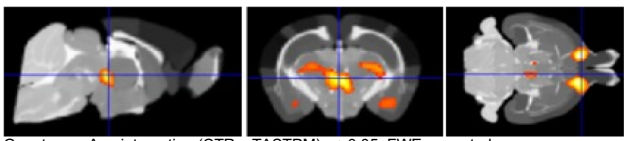
Genotype x Age interaction (CTR x TASTPM). p>0.05, FWE corrected.

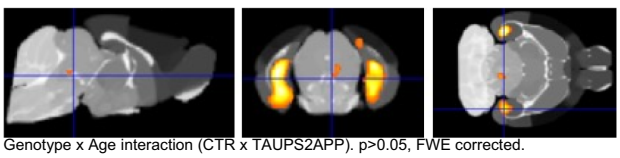
Genotype x Age interaction (CTR x TAUPS2APP). p>0.05, FWE corrected.

Results:
The flexible factorial analysis in SPM12 revealed a strong interaction between time and genotype among the 3 groups in the hippocampal formation, entorhinal area, vermis, thalamus, and neostriatum. In paired comparison—'controls against TASTPM' a strong interaction between time and genotype was seen in the nucleus accumbens, striatum, thalamus, cerebellum, and olfactory areas. The analogous comparison with TAUPS2APP group showed in triple TG mice this interaction was isolated to the hippocampal formation.
Discussion/Conclusion: The present results extend previous evidence obtained from the same database (Micotti et al. 2015; manual tracing) disclosing novel regions of progressive brain atrophy in TASTPM mice (i.e., thalamus, nucleus accumbens, and cerebellum). The effect in the nucleus accumbens corroborated literature about early alterations of mesolimbic dopaminergic systems in Tg2576 TG mice overexpressing the APP695 protein (Nobili et al. 2017), while the alteration in the cerebellum fits previous observation of local AD pathology in early-onset AD patients with PS1 mutation (Larner and Doran 2006). Overall, the present approach was successful to unveil different abnormalities in the brain over time in two common TG strains of AD.

References:
Micotti, E., Paladini, A., Balducci, C., Tolomeo, … Forloni, G. 2015. *Neurobiol. of Aging, 36(2), 776–788.* https://doi.org/10.1016/j.neurobiolaging.2014.10.027.
Nobili, A., Latagliata, E. C., Viscomi, … D'Amelio, M. 2017. *Nature Commun,8.* https://doi.org/10.1038/ncomms14727.
Larner, A. J., & Doran, M. 2006. *J. of Neurol. 253(2), 139–158.* https://doi.org/10.1007/s00415-005-0019-5.

P01.19

Time-dependent diffusion coefficient in Baker's Yeast studied by single-sided NMR: attempts to the exploration of structures with a sub-micrometer size

W. Mazur, A. T. Krzyżak

AGH University of Science and Technology, Department of Fossil Fuels, Krakow, POLAND

Purpose/Introduction: It is well known that time-dependent diffusion coefficient can be an indicator of tissue compartmentalization [1], and can be used in the studies of dynamic properties of water species in cells. A very common model of living cells in NMR studies is Baker's yeast (*Saccharomyces Cerevisiae*), the geometry of which is known and probed extensively by using pulsed-field-gradient techniques (e.g. [2], [3]). We propose the application of constant gradient compact NMR-MOUSE device in order that enhance the existing analyses and develop the characterization of micrometer and sub-micrometer biological structures, which are beyond the compass of PFG technique.
Subjects and Methods: We measured diffusion in fresh baker's yeast (Lesaffre Polska SA) by using extremely high, constant gradient $g \sim 24\ \mathrm{Tm}^{-1}$. To obtain an echo decay we varied diffusion encoding time $\tau = 0.02$–0.6 ms for several values of diffusion time, t_d in the short-time limit with the echo time of 40.5 μs. Our analysis is based on the application of existing approximations in order to estimate self-diffusion coefficients in yeast [4], cells' size and to approach the accurate evaluation of cell membrane permeability [2] by single-sided NMR. The results were compared with results from the yeast suspension measurements.
Results: For fresh yeast, three-compartmental model was applied reflecting extracellular water, intracellular fluid and water species associated with cellular organelles (Fig. 1A). From the short-time behavior of water we estimated self-diffusion coefficients of each component. The slowest component was associated with compartment size of < 1 μm. The membrane permeability of yeast cells calculated on the grounds of a tri-exponential stimulated echo decay for fresh yeast was $\sim 10^{-6}\ \mathrm{ms}^{-1}$.

Discussion/Conclusion: In the work we demonstrate, that the most common, two-compartmental model of diffusion of water in fresh yeast is not sufficient for very strong gradients. The analysis of yeast suspension is more problematic, since the models applied to the fresh yeast sample do not fit the data (Fig. 1B). Hence, by using NMR-MoUSE it is possible to distinguish components with very low diffusivities ($\sim 10^{-12}$ m^2s^{-1}) reflecting cellular organelles if the extracellular water fraction is minimized.

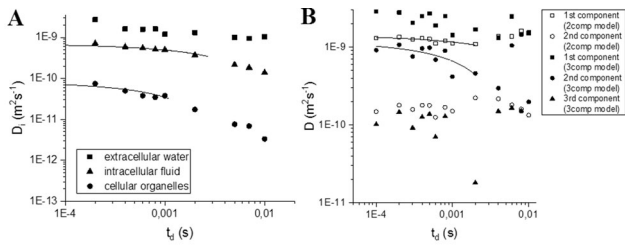

Fig. 1. Time dependent diffusion coefficients: A- fresh yeast, three-compartmental model, B- yeast suspension, two- and three-compartmental models.

References:

[1] D. G. Cory and A. N. Garroway, *Megnetic Reson. Med.*, vol. 14, pp. 435–444, 1990.

[2] K. Suh, Y. Hong, V. D. Skirda, and V. I. Volkov, *Biophys. Chem.*, vol. 104, pp. 121–130, 2003.

[3] I. Åslund and D. Topgaard, *J. Magn. Reson.*, vol. 201, no. 2, pp. 250–254, 2009.

[4] P. P. Mitra, M. P. N. Sen, L. M. Schwartz, and P. Le Doussal, *Phys. Rev. Lett.*, vol. 68, no. 24, pp. 3555–3558, 1992.

Acknowledgments

The work was partly financed by the National Centre of Research and Development, contract no. STRATEGMED2/265761/10/NCBR/2015.

W.M. has been partly supported by the EU Project POWR.03.02.00-00-I004/16.

P01.20

Is the hepatic fatty-acid chain length dependent on the hepatic fat content?

M. Burian[1], M. Drobny[1], P. Sedivy[1], M. Dezortova[1], I. Ibrahim[1], I. Hejlova[2], M. Hajek[1], P. Trunecka[2]

[1]IKEM, MR Unit, Prague, CZECH REPUBLIC, [2]IKEM, Dept. of Hepatology, Prague, CZECH REPUBLIC

Purpose/Introduction: Hepatic fat fraction and the mean fatty-acid chain length were analyzed using single-voxel 1H MR spectroscopy. The ratio of CH_2 and CH_3 resonances at 1.3 and 0.9 ppm served as a marker of aliphatic chain length.

Subjects and Methods: 174 MRS examinations were performed in patients (n = 106) before and after liver transplantation to determine hepatic fat content (HFC).

Basic demographic and clinical characterizations of all patients are specified in Table 1. The experimental protocol was approved by the local ethical committee. All subjects were informed about the examination protocol and signed a written consent.

Subjects were examined in a supine position at 3T Magnetom Trio Siemens tomograph equipped with eight-channel surface body coil. Standard PRESS single voxel spectroscopy sequence was used (echo time (TE) 30 ms and repetition time (TR) 4500 ms) to assess HFC. MR images obtained in three basic anatomical orientations were used to set the chosen volume of interest (VOI) of 40 × 30 × 25 mm, see Figure 1. One acquisition during single breath hold was acquired three times with and without water suppression. Spectra were evaluated with the LCModel[1] using extended basis set to include all the lipid resonances as proposed in [2]. HFC values were used to classify patients according to Kleiner scale—see [3,4]

Male (%)	98(56%)
Age	56±11
BMI	26±4
Triglycerides (mmol/l)	1.35±0.98
Cholesterol (mmol/l)	4.38±1.25
LDL chol (mmol/l)	2.64±0.92
HDL chol (mmol/l)	1.10±0.43
Glycemia (mmol/l)	5.88±1.82
HbA1c (mmol/mol)	35.37±10.33
C-peptid (nmol/l)	1.06±0.58
QUICKI	0.35±0.04

Table 1: Patient group characteristics

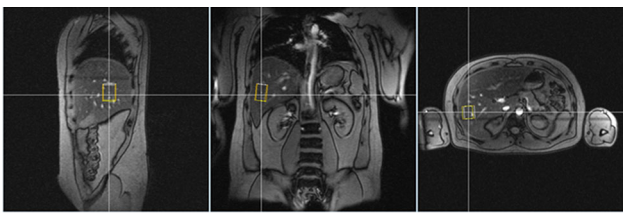

Figure 1: MRS voxel localization within patient liver

Results: Relative signal intensities corresponding to peaks of particular lipid resonances were calculated from water-suppressed spectra and compared to the Kleiner score for each subject. Relative intensities are summarized in graphs representing profile of measured lipid signals in liver for each Kleiner score—see Figure 2.

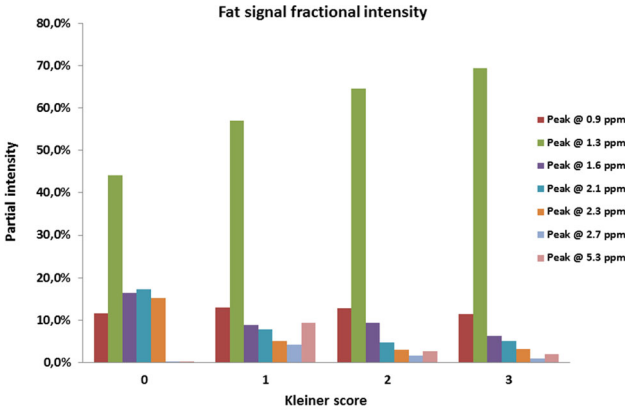

Figure 2: Signal intensities of ^{1}H lipid resonances relative to total fat signal vs. Kleiner score

Discussion/Conclusion: The most prominent signal changes are in CH_2 signal intensities at 1.3 ppm while the CH_3 signal at 0.9 ppm stays steady. There are also significant trends in decrease in signal intensities at 1.6, 2.1 and 2.3 ppm with increasing hepatic fat score. The ratio of these intensities would supposedly change with fatty-acid chain length which seems to be longer with increasing of fat content in liver. These data can be useful for detailed characterization of steatosis.

Acknowledgements

The study was supported by AZV MHCR 15-26906A and MHCZ DRO MZO 00023001 IKEM projects.

References

1. Provencher SW. NMR Biomed. 2001;14(4):260–264.
2. Hamilton G et al. J Magn Reson Imaging. 2009;30(1):145–152.
3. Longo R et al. J Magn Reson Imaging. 1995;5(3):281–285.
4. Hajek M et al. Magn Reson Mater Phy 2011; 24(5):297–304.

P02 Electronic and Paper Posters

Innovations in MR Technology

P02.01

A correction method for motion-induced signal dropout in diffusion MRI

C. -F. J. Huang[1], Y.-J. Chen[2], Y.-C. Hsu[2], W.-Y. I. Tseng[2]

[1]National Taiwan University, Institute of Biomedical Engineering, Taipei, TAIWAN, [2]National Taiwan University, Institute of Medical Device and Image, Taipei, TAIWAN

Purpose/Introduction: A key problem in diffusion MRI is motion-induced signal dropout, which may cause errors in diffusion index calculation.[1,2] Therefore, this work aimed to develop a post-processing algorithm to correct signal dropout of diffusion spectrum imaging (DSI) data. The correction performance was tested by in vivo experiments with the DSI data sets having signal dropout caused by head motion. In addition, simulation experiments were performed by simulating signal dropout in the reference DSI data sets to validate the accuracy in diffusion index calculation.

Subjects and Methods: Imaging:DSI data were acquired on a 3T MRI system (TIM Trio, Siemens, Erlangen) with a 32-channel phased array coil. The DSI pulse sequence used a twice-refocused balanced echo diffusion echo planar imaging sequence [3], TR/TE = 9600/130 ms, FOV = 200 × 200 mm^2, matrix size = 80 × 80, 56 slices, and 2.5 mm in slice thickness. A total of 102 diffusion encoding gradients with the maximum diffusion sensitivity bmax = 4000 s/mm^2 were sampled on the grid points in a half sphere of the 3D q-space. **Signal dropout correction:** For each volume data corresponding to a specific diffusion encoding, we assumed that signal intensity along the z (slice) direction was a smooth curve. Signal dropout at any z location in the curve can be resumed by using least-squares fitting of the remaining data with B-spline curves. [4] **In-vivo experiments:** Fifteen DSI data sets with signal dropout were selected and corrected by signal dropout correction method to show the image quality improvement. **Simulation experiments:** Fifteen DSI data sets without signal dropout were selected as the reference. These DSI data sets were used to simulate the data sets degraded by signal dropout; the original DW images were replaced randomly with signal dropout images. For each data set, 15 simulated data sets were created using 15 different dropout numbers, i.e. 10, 30, 50, 70, 90, 130, 170, 210, 250, 290, 340, 380, 420, 460 and 500. **Validation of simulation experiments:** We used whole brain tract-based automatic analysis to obtain generalized fractional anisotropy (GFA) profiles of 76 white matter tract bundles for each DSI dataset. [5] We tested the performance of the correction method by assessing the functional difference (FD) between GFA profiles derived from the reference DSI data set and those derived from the degraded and corrected data sets. [6] Functional difference was defined as:

$$\mathrm{FD} = \frac{1}{n * m * l} \sum_{k=1}^{n} \sum_{j=1}^{m} \sum_{i=1}^{l} \left| \frac{f(t_i, tb_j, s_k) - f_{ref}(t_i, tb_j, s_k)}{f_{ref}(t_i, tb_j, s_k)} \right|$$

where $f(t_i, tb_j, s_k)$ and $f_{ref}(t_i, tb_j, s_k)$ were the measured GFA values at step t_i for tract bundle tb_j in subject s_k derived from the degraded/corrected DSI data sets and reference DSI data sets, respectively, and l, m, n indicated, the total number of steps of a tract bundle, the total number of tract bundles, and the total number of subjects, respectively.

Results: The results are shown and described below:

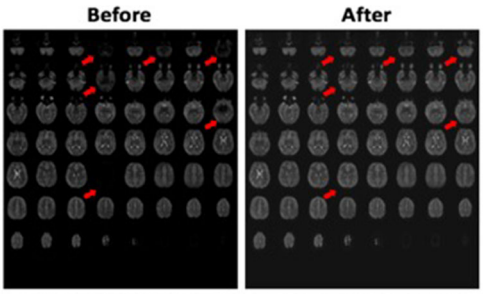

Figure1 : The representative diffusion volume before (left) and after (right) signal dropout correction in in-vivo experiment. Red arrows indicate the image quality improvements of the images which affected by signal dropout and this improvement can be identified via visual inspection.

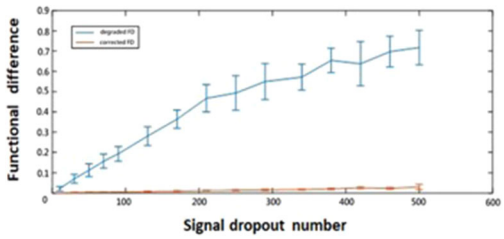

Figure2 : The plot of number of signal dropout vs. functional difference (FD) in degraded and corrected DSI datasets in simulation experiment. The degraded FD values increase sharply with the dropout number. By contrast, the corrected FD values increase very slightly with the dropout number.

Discussion/Conclusion: We develop a novel method to correct motion-induced signal dropout, and validated the method in simulated DSI data sets.

References:

1)Yendiki et al. Neuroimage, 2014. 2) Benner et al. Magnetic resonance in medicine, 2011. 3) Reese et al.Magnetic Resonance in Medicine, 2003. 4) Eberly. Geometric Tools, 2008. 5) Chen et al. Human brain mapping, 2015. 6) Gouttard et al. SPIE Medical Imaging. 2012.

P02.02

An Ultrasound-Guided Injection method for a refinement and efficient breast tumor induction into mice

F. La Cava[1], **A. Fringuello Mingo**[2], S. Colombo Serra[2], A. Di Vito[2], C. Cabella[2], P. Oliva[2], A. Cordaro[2], E. Terreno[1], L. Miragoli[2]

[1]Università di Torino, Department of Molecular Biotechnology and Health Center, Torino, ITALY, [2]Bracco Imaging spa, Colleretto Giacosa, ITALY

Purpose/Introduction: Breast cancer is the most common cancer for US women. MRI with the use of Contrast Agents is a recommended screening, especially for high-risk women.[1]The use of animal models is essential to test contrast efficacy of CAs under development. Breast cancer orthotopic models can be achieved by implantation under direct vision of the mammary fat pad or Orthotopic Percutaneous blind injection (OP) in the nipple area.[2–3] To overcome the invasiveness of surgery and the limited accuracy of OP ultrasound was introduced as a guide for precise localization. The model was characterized by MRI.

Subjects and Methods: BT20 cells (10^6 to 10^7) were injected into the fourth Mammary Fat Pad of female nu/nu mice via classic surgery (n = 6) and UltraSound guided injection (n = 16) by using a Vevo Lazar 2100 US System. 4T1 (5×10^5 to 10^6) and TS/A (5×10^4 to 5×10^5) cells were injected into the mfp of 26 Balb/C female mice by using US guided injection.

Tumor growth was monitored by MR/US imaging weekly or closer. Mice developing noticeable masses were recruited for Contrast Enhanced MRI studies, performed by a Bruker Biospec 3T equipped with a 20 mm diameter surface coil. At the end of the study tumor identity was confirmed by histology.

Results: Both surgery and US-guided injection were successful in locating the BT20 tumor mass into the mfp, as confirmed by MRI and histology. Despite no intraoperative death occurred the invasiveness of surgery was not negligible. US-guided injection, reducing the animal post-operative suffering, resulted an optimized refinement procedure.

BT20 tumor growth was limited, reaching a maximum volume of 10 mm^3 in 6 weeks. When detectable the diseased mass showed a 50–80% signal enhancement after CA administration at 0.1 mmol/kg. 4T1 and TS/A cells were injected into the mfp to confirm the validity of the US-guided injection. 4T1 and TS/A cells grew rapidly reaching the set end point (300 mm^3) or considerable volumes (< 100 mm^3) in less than 2 weeks. The two tumors exhibited a different morphology in the animal, 4T1 tumors were round grew externally and tended to incorporate the mfp rendering it almost invisible during the MRIs. TS/A tumors grew internally and retained the mfp. Moreover necrosis of the nipple area was visible at low volumes (less than 20 mm^3). After CA administration, a > 70% enhancement was observed with MRI sequences.

Discussion/Conclusion: Breast cancer drug development is ineffective without a reliable preclinical model which is hard to identify. In this work a novel refinement method to induce breast cancer was developed and three different cell lines were tested. The use of CE MRI served as a way to fully characterize the tumor and study its vascularization rendering this model useful for efficacy study thus bridging the gap between clinical and preclinical research.

References:

1 JAmCollRadiol 2016;13(11S):R45–R49
2 Am J Pathol. 2007;170(3):793–804
3 Breast Cancer Res Treat. 2014;147(3):501–12

P02.03

Automated segmentation of bone regions by deep learning for the quantitative analysis of whole-body magnetic resonance imaging

N. Hayashi[1], K. Iwasaki[1], Y. Sato[2], T. Maruyama[3], S. Motegi[4], A. Ogura[1], T. Ogura[1], S. Kumasaka[5], Y. Tsushima[5]

[1]Gunma Prefectural College of Health Sciences, Radiological Technology, Maebashi, JAPAN, [2]Gunma University Hospital, Radiology, Maebashi, JAPAN, [3]Shinshu University Hospital, Radiological Technology, Matsumoto, JAPAN, [4]Josai Clinic, Radiology, Maebashi, JAPAN, [5]Gunma University Graduate School of Medicine, Diagnostic Radiology and Nuclear Medicine, Maebashi, JAPAN

Purpose/Introduction: Whole-body diffusion-weighted imaging (WB-DWI) is as sensitive as bone scintigraphy in detecting bone metastasis of prostate and breast cancers [1, 2]. Additionally, WB-DWI can be utilized for whole-body examination at a facility without a nuclear medicine examination equipment. However, unlike for bone scintigraphy, quantitative evaluation of WB-DWI has not been established. Quantitative evaluation using apparent diffusion coefficient (ADC) has been attempted, and we are examining more accurate methods. For this purpose, we should be able to recognize anatomical regions from WB-DWI. In this study, we aimed to segment bone, lung, digestive tract, body, and extracorporeal areas from a T1-weighted image of the WB-MRI using the deep learning technique.

Subjects and Methods: We acquired WB T1-weighted images from 15 patients. The apparatus used was 1.5 T Philips Achieva (Best, Netherlands). To segment regions by deep learning, we manually segmented each region as the teacher data. The manually labeled training image was cut into 61 × 61 patch images and used as the input to the learned AlexNet network, which has been trained using the transfer learning method by fine tuning. We tested the learned network using the 5-hold cross-validation method. The output results of the test image were evaluated using the mixing matrix.

Results: Using patch segmentation by deep learning, we could successfully segment bone, lung, digestive tract, body, and extracorporeal areas. The segmentation accuracy of the proposed method was 89.1%.

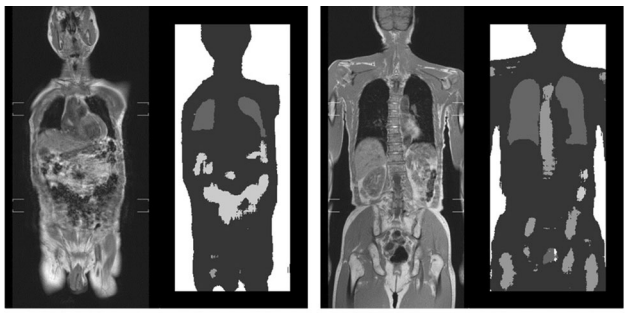

Results of the segmentation using deep learning. (a) and (c) are original WB T1-weighted images. (b) and (d) are the results of the segmentation of (a) and (c).

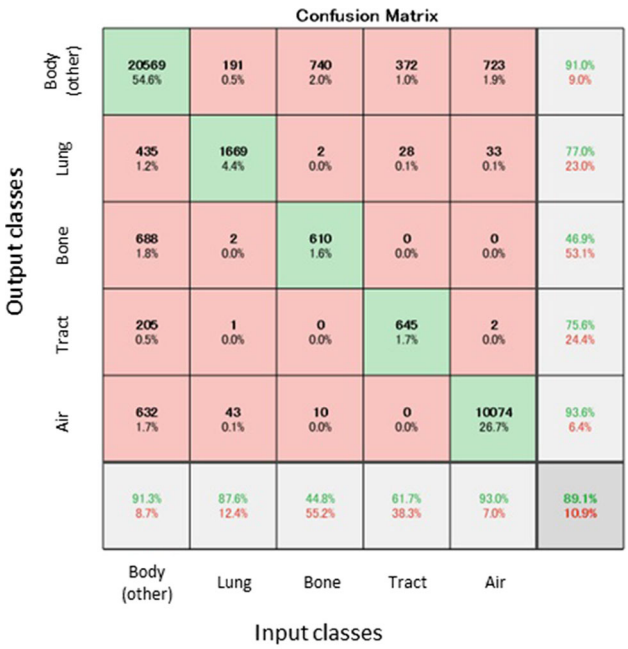

Results of the confusion matrix. The total accuracy was 89.1 %.

Discussion/Conclusion: The quantitative analysis in WB-DWI uses the ADC volume and a high signal. Unlike in bone scintigraphy, in DWI, normal regions are counted because of artifacts and calculation errors. If an anatomical region is segmented in advance using this method, these false positive counts can be deleted. Therefore, it is expected that a quantitative analysis in WB-DWI with higher accuracy is possible.

References:

1. Blackledge MD, Collins DJ, Tunariu N, Orton MR, Padhani AR, Leach MO, et al. Assessment of treatment response by total tumor volume and global apparent diffusion coefficient using diffusion-weighted MRI in patients with metastatic bone disease: a feasibility study. PLoS One. 2014;9(4):e91779.

2. Nakanishi K, Kobayashi M, Nakaguchi K, Kyakuno M, Hashimoto N, Onishi H, et al. Whole-body MRI for detecting metastatic bone tumor: diagnostic value of diffusion-weighted images. Magn Reson Med Sci. 2007;6(3):147–55.

P02.04

Active Learning for the Adaption of Trained CNN Models for Detection of Motion Artifacts to New Data

A. Liebgott[1], T. Haueise[2], T. Küstner[2], K. Nikolaou[1], B. Yang[2], S. Gatidis[1]

[1]*University Hospital of Tuebingen, Diagnostic and Interventional Radiology, Tuebingen, GERMANY,* [2]*University of Stuttgart, Institute of Signal Processing and System Theory, Stuttgart, GERMANY*

Purpose/Introduction: Motion artifacts can critically impair image quality and diagnostic value. Recently, several promising studies involving automated detection of motion in MR images have been published, mostly using convolutional neural networks (CNNs)[1,2]. However, CNN models strongly depend on the training data, so even slightly different data often can not be classified as well. Re-training a model with additional data involves time-consuming labeling. To adapt a CNN model using as little new data as possible is hence desirable. We investigated if active learning (AL) is suitable to extend a model from detecting strong motion to also recognizing weak motion artifacts.

Subjects and Methods: We used scans of 12 volunteers acquired on a 3T MR scanner (Siemens Skyra) with 3 stages of motion (see Fig. 1). We trained a patch-based 3D CNN based on VNET[1] to classify type 1 vs. type 3, achieving an accuracy A = 89.9%.

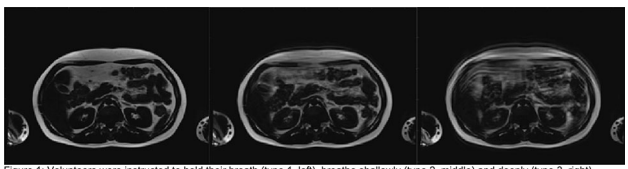

Figure 1: Volunteers were instructed to hold their breath (type 1, left), breathe shallowly (type 2, middle) and deeply (type 3, right), resulting in no, week and strong motion artifacts.

Classification of type 2 images of 5 volunteers unused during the previous training resulted in A = 64.3%. When simply re-training the model with type 2 and type 3 as class "motion", an accuracy of A_T = 90.1% was achieved, serving as our target accuracy. To enable the model to also correctly classify type 2 patches as motion with as few additional samples as possible, we included AL in the training (Fig. 2) to iteratively re-train the CNN with only the most informative new patches. As criterion for informativeness, we investigated uncertainty sampling (US)[3] and DeepFool Active Learning (DFAL)[4].

We also analyzed the influence of the batch size N_B (samples drawn per iteration).

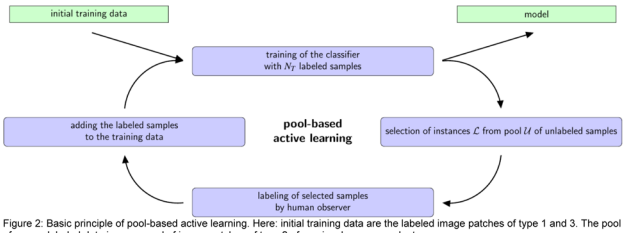

Figure 2: Basic principle of pool-based active learning. Here: initial training data are the labeled image patches of type 1 and 3. The pool of new unlabeled data is composed of image patches of type 2 of previously unseen volunteers.

Results: Fig. 3a shows the resulting accuracy over the total number of samples drawn for different N_B using US. While all investigated N_B result in similar A_{max} in the end (ca. 96%), using N_B = 250 leads to the lowest amount of new samples $N_{S,T}$ needed to achieve A_T. Figure 3b shows a comparison between different sampling criteria. US slightly outperforms DFAL and is significantly better than drawing random samples (RS).

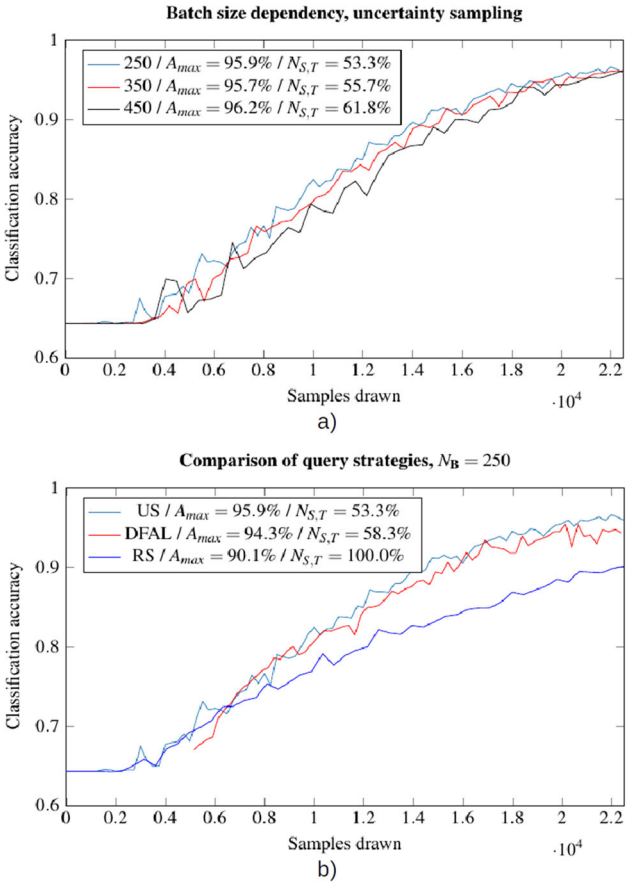

Fig. 3: Accuracy over total samples drawn for different N_B with uncertainty sampling (US) (a) and for different sampling criteria US, DFAL and random (RS) with N_B = 250 (b). A_max: maximum accuracy, N_S,T: percentage of samples needed to reach A_T

Discussion/Conclusion: We found that AL can be used to adapt a trained CNN model to new data. Training with only the most informative samples can lead to an increased accuracy compared to training with all available new samples. Moreover, the batch size influenced the total amount of data needed to achieve our target accuracy. Overall, we found that $A_{max} > A_T$ for all N_B and both US and DFAL, with US combined with smaller N_B resulting in the lower N_T. In general, the decision criterion is a crucial factor, so additional strategies should be investigated.

References:
[1]Küstner et al. "Automated reference–free detection of motion artifacts in magnetic resonance images" *MAGMA 09/17*.
[2]Fantini et al. "Automatic detection of motion artifacts on MRI using Deep CNN" *PRNI 2018*.
[3]Lewis et al. "A sequential algorithm for training text classifiers" *Proc. SIGIR '94*.
[4]Ducoffe et al. "Adversarial Active Learning for Deep Networks: a Margin Based Approach" *arXiv 2018*.

P02.05

3D Rigid-Body Motion Estimation for Brain Imaging using Orbital Navigators and Field Monitoring

T. Ulrich, F. Patzig, B. J. Wilm, K. P. Prüssmann

ETH Zürich and University of Zürich, Institute for Biomedical Engineering, Zürich, SWITZERLAND

Purpose/Introduction: Patient motion is a common problem in MRI, because it can lead to severe image artifacts. K-space navigators have been studied extensively as a means of estimating patient motion, but errors in the trajectory affect the accuracy of the motion estimates. Therefore, we propose a combination of k-space navigators and field monitoring for motion estimation.

Subjects and Methods: We used a modified version of 3D orbital navigators.[1] Our navigator trajectory consists of three orthogonal circles, all at the same radius r = 400 rad/m. For a fast single-shot acquisition of the navigator signal, the trajectory has been smoothed using a moving average filter. We used field monitoring[2] to reliably measure the actual k-space trajectory.

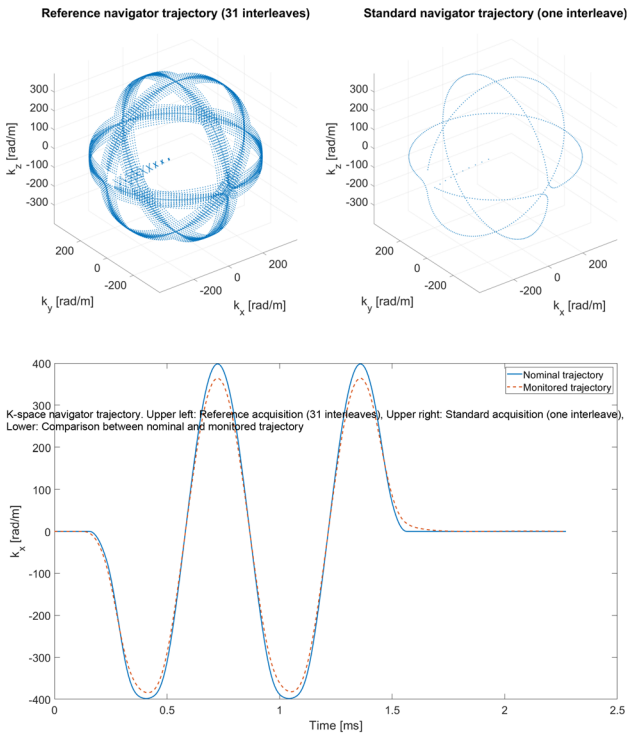

K-space navigator trajectory. Upper left: Reference acquisition (31 interleaves), Upper right: Standard acquisition (one interleave), Lower: Comparison between nominal and monitored trajectory

The lower plot shows how the monitored trajectory deviates from the nominal trajectory. Because of the low-pass filter characteristics of the gradient impulse response function, the monitored trajectory does not reach the desired radius of 400 rad/m. Moreover, because of delays in the gradient system and gradient pre-emphasis, there are temporal mismatches between the nominal and monitored trajectory.

K-space navigator trajectory. Upper left: Reference acquisition (31 interleaves), Upper right: Standard acquisition (one interleave), Lower: Comparison between nominal and monitored trajectory

Like Welch et al.,[3] we calculated the optimal rotation angles iteratively through a least-squares minimization problem, and we interpolated the expected navigator signal for a set of rotation angles from the reference scan. Unlike them, however, we solved the minimization problem with MATLAB's *fminunc* function, and we used 4D convolution-based interpolation with the Kaiser-Bessel kernel.
Once rotations have been estimated, the translation parameters are calculated through a weighted least-squares fit of the phase difference between the two navigator signals. The signal magnitude serves as the weighting parameter.

Results: Simulations were performed using a 3D version of the Shepp-Logan phantom. We applied a rigid-body transformation to the phantom, simulated the k-space navigator signal along a monitored trajectory before and after the transformation, and estimated the transformation parameters as described above. Estimation was performed both with the monitored and the nominal trajectory. After 25 simulation runs, we calculated the mean absolute error of the estimated vs. the simulated motion parameters.

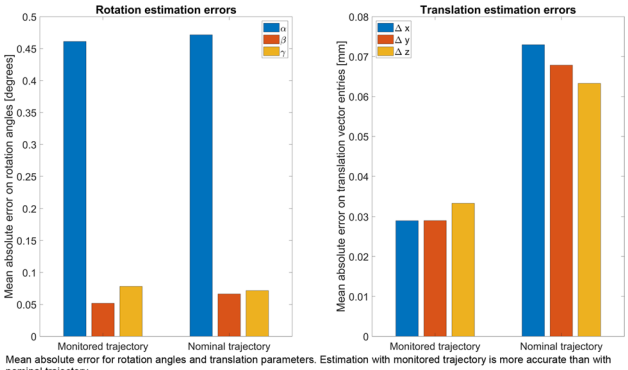

Mean absolute error for rotation angles and translation parameters. Estimation with monitored trajectory is more accurate than with nominal trajectory.

Additionally, we performed cross-validation of our navigator method and image registration in vivo. We have acquired a reference navigator signal (31 interleaves), and a stack of slice images (center-out spiral trajectory). We have instructed the volunteer to move his head, before acquiring another navigator signal (one interleave) and another stack of slice images. We have estimated the motion parameters both from the k-space navigators (with field monitoring) and from the image scans using image registration.

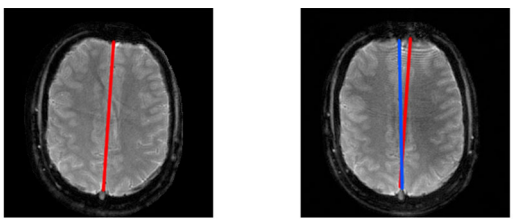

Slice images of a volunteer before and after instructed head movement. The red line highlights the orientation of the interhemispheric fissure in the first picture. The blue line highlights its orientation in the second picture. From the stack of 2D images, the rotation angles and translation vector between the two positions can be estimated using MATLAB's *imregtform* function. We found the following transformation parameters using our k-space navigator technique:
Rotation angles: 4.67° (HF axis), -0.94° (LR axis), 2.13° (AP axis)
Translation vector: 0.00mm, 4.43mm, 1.77mm
Values found with image registration deviated from those values by up to 0.36° and up to 0.25mm, respectively.

Slice image of volunteer's brain. Left: Before instructed head movement, Right: After instructed head movement

Discussion/Conclusion: We have demonstrated that errors in the trajectory negatively affect the accuracy of k-space navigator-based motion estimation. We believe that rotation estimation is mostly affected by residual gradient delay, while translation estimation suffers from the low-pass filter characteristics of the gradient system.

Monitoring of the k-space trajectory improves the accuracy of the estimated motion parameters.

References: 1. Fu Zhuo Wu et al. *MRM* **34**, 746–753 (2005).
2. Barmet, C. et al., *MRM* **60**, 187–197 (2008).
3. Welch, E. B. et al., *MRM* **47**, 32-41 (2001).

P02.06

On Accurate Metabolite Quantification in Presence of Different Coil Loading. "TRAMP" Method for Single Voxel MR Spectroscopy Revised

R. Sitnikov

Karolinska University Hospital, Neuroradiology, Stockholm, SWEDEN

Purpose/Introduction: Most of the pitfalls in quantification procedure for SV MR spectroscopy are overcome when the ratio method metabolite to endogenous reference is used with the assumption they are acquired under the same conditions hence, all instrumental factors are cancelled out from the ratios. Apparently, this may not be the case when different transmit coil loading by patients causes the scanner transmitter gain (TG) calibration to converge not always to optimal value. The shape for the voxels associated with metabolites and REF begin to diverge at small TG offsets. This is amplified by chemical shift displacement (CSD) giving rise to inconsistency in obtained ratios. LCmodel^{TM} has a built-in correction coefficient for such effects called "*TRAMP*" (*TRansmitterAMPlitude*). *TRAMP* has been found seldom useful for MRS quantification despite of previous efforts [1]. We have developed further this concept that ideally should enable accurate quantification at the stage of post processing.

Subjects and Methods: The MRS data was acquired on GE MR750, 3 T scanner, 8 channels head coil array In-VIVO^{TM}, with PRESS localization, te/tr = 68/2000 ms. For ex vivo a GE phantom BRAINO + 10 mM GABA was used. To emulate patient loading TG was varied ± 6 mdBu units from the calibrated TG while controlling for the RF pule profile. In-vivo data was obtained from 180 healthy subjects in age 20–80, with 11 mL voxel positioned in Putamen. Data was quantified in LCModel^{TM} 6.3 with simulated basis set for 20 metabolites. The *TRAMP* was computed by Nedler-Mead optimization routines with the objective function $std(C_{met} \cdot TRAMP)$ that showed a robust convergence with phantom data.

$TRAMP = 10^{(amp\_met \cdot \Delta TG)}$, *where* $\Delta TG = TG - TGref$, $TGref = W \cdot \partial TG/\partial W + b$

TRAMP was computed for each metabolite. TG is transmitter gain and W pat.weight read from the data header. TGref was found from linear fit to TG(W) data and established a "true" TG.

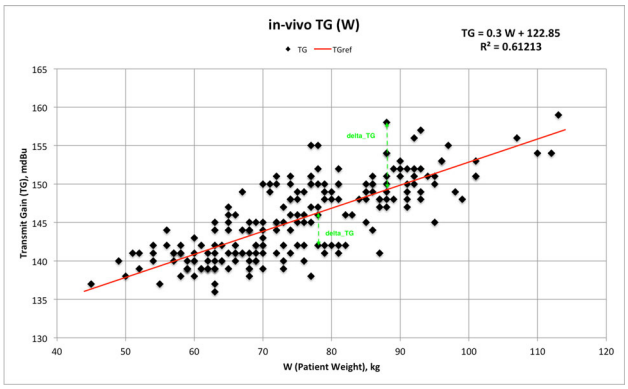

Transmitter Gain Calibration vs. Patient Weight, Putamen.

Results: Ex-vivo: CRLB after LCModel fit was between 1-6%. The standard error (SE) over 12 experiments for each VOI positions was largest for GABA, Glu, Ins and was reduced by factor of 3 after correction (Table).

BRAINO+						
Metab	Conc. Nominal	Conc. LCM	Conc corr	Amp TRAMP	SDerr %	STDerr % Corr
Cr	10	11.24	11.09	-0.0011	1.60	1.04
GABA	10	9.93	9.59	-0.0084	**9.28**	2.59
Glu	12.5	12.35	12.50	-0.0065	**8.47**	4.18
PCh	3	3.16	3.19	-0.0022	2.96	1.53
Lac	5	5.73	5.73	-0.0025	4.69	3.77
NAA	12.5	13.37	13.30	-0.0026	2.98	0.61
Ins	7.5	7.82	7.69	-0.0052	**6.85**	4.15
Cr REF	10	10.00	-	-	-	-
GABA/Cr	10	8.91	8.49	-0.0073	**8.25**	2.96
Glu/Cr	12.5	11.32	11.04	-0.0054	**7.45**	4.59
PCh/Cr	3	2.84	2.86	-0.0011	2.22	1.79
Lac/Cr	5	5.12	5.16	-0.0014	3.60	3.22
NAA/Cr	12.5	11.99	11.94	-0.0015	2.03	1.13
Ins/Cr	7.5	6.99	7.04	-0.0048	6.78	4.41

TRAMP corrections applied to each metabolite, ex-vivo data.

In-vivo: TG variations was up to ± 8 mdBu for selected patient weights. *TRAMP* corrects effectively for this variability (Fig. 2). The amp_met was in the range of 0.001–0.011, with the largest for Lac, 0.015. After correction SE and means were reduced only by 1-3%. A general linear model (Cmet ~ Age + Gender + BMI) revealed significant changes due to Age but not BMI or Gender for corrected GABA, Glu, NAA, Ins, Cr, MM09, MM18.

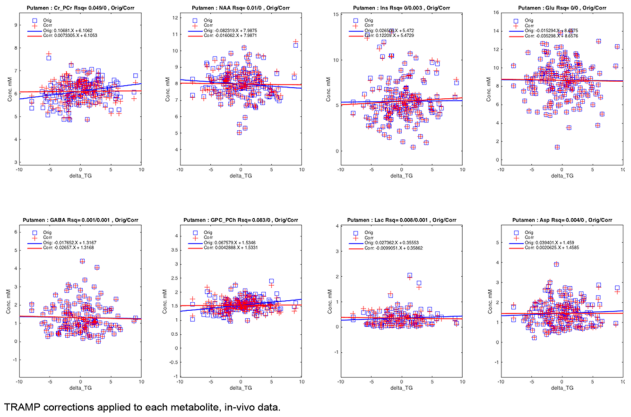

TRAMP corrections applied to each metabolite, in-vivo data.

Discussion/Conclusion: The suggested approach for correction in overall reduces instrumental variance in quantified data and preserves the biologically relevant information. The data demonstrated significant changes of neurotransmitters in healthy aging brain that are consistent with published studies [2].

References:

1. Fernandez-Seara MA, et al. (2001) MRM 30:672–679
2. Ding X-Q, et al. (2016) NI 137:45–51

P02.07
WITHDRAWN

P02.08
Tracking integrity and localization of cell-containing capsules

J. Haeck[1], S. Khatab [2], M. Leijs[2], G. van Buul[3], G. van Osch[4], **M. Bernsen**[1]

[1]*Erasmus MC, Radiology & Nuclear medicine, Rotterdam, NETHERLANDS,* [2]*Erasmus MC, Radiology & Nuclear medicine; Orthopaedics, Rotterdam, NETHERLANDS,* [3]*Erasmus MC, Orthopaedics, Rotterdam, NETHERLANDS,* [4]*Erasmus MC, Orthopaedics; Otorhinolaryngology, Rotterdam, NETHERLANDS*

Purpose/Introduction: Alginate microcapsules support long term in vivo viability of locally administered cells, such as embryonic or mesenchymal stem cells, for therapeutic purposes (Blocki_2015). To study the use of microcapsules in stem cell therapies it is important to be able to monitor their presence and the integrity of the alginate microcapsules in vivo. We and others have previously shown that Gadolinium (Gd) can be used as a cellular label to label cells in vivo and that depending on the environment Gd exerts different effects on T1 and T2 relaxation times. In this study, we investigate the feasibility to engineer Gd-conjugated alginate constructs, and the use of quantitative parametric MRI to assess the integrity of these constructs based on T1, T2 and T2* times measured, when used as carriers for mesenchymal stem cells.

Subjects and Methods: Alginate containing high α-L-guluronic acid (G) next to β-D-mannuronic acid (M) polysaccharides (kind gift of CellMed AG, Alzenau, Germany) was crosslinked using a range of Gadolinium(III) chloride hexahydrate concentrations in a 102 mM $CaCl_2$ solution. Resulting Gd-conjugated microcapsules were imaged under different conditions in vitro, ex vivo and in vivo, using T1-weighted imaging and T1, T2, en T2* parametric mapping. As model systems for in vivo monitoring of cell-based therapy we administered alginate constructs subcutaneously and intra-articularly in rats and intra-articularly in horse knees.

Results: Incorporation of Gd into alginate constructs resulted in the ability to visualize these constructs and the amount of Gd in the construct could be quantified using quantitative parametric mapping techniques. Using weighted imaging we were able to visualize Gd-conjugated alginate constructs under various conditions. Single beads with a diameter of 300 μm could be visualized intra-articularly in rats (in vivo) and horses (ex vivo). Moreover, we were able to perform longitudinally follow up of cell-containing constructs for at least 8 weeks. Furthermore we show that depending on the Gd concentration contained alginate constructs, different quantitative MR signatures are obtained and that such an imaging approach may be used to monitor the integrity of the alginate constructs over time.

Discussion/Conclusion: We show that alginate constructs can be efficiently conjugated with Gadolinium which allows for visualization, quantification and characterization of these constructs. These findings may be relevant in cell-based therapy studies or other applications using polymeric constructs as a carrier.

References:

Blocki A et al. Microcapsules engineered to support mesenchymal stem cell (MSC) survival and proliferation enable long-term retention of MSCs in infarcted myocardium. Biomaterials 53:12 (2015).
Guenoun J et al. Compartmentalization of Gd liposomes: the quenching effect explained. Contrast Media Mol Imaging 11(2):106 (2016).

P02.09
3D rigid body motion correction in ASL-perfusion imaging using 3D GRASE PROPELLER

J. Huber, D. C. Hoinkiss, M. Vicari, M. Günther, R. Wilke

Fraunhofer MEVIS, Bremen, GERMANY

Purpose/Introduction: Arterial spin labeling (ASL) MRI allows to visualize and quantify tissue perfusion without exogenous contrast agents by using labeled blood as an endogenous tracer. However, relying on images from different time points, ASL is sensitive to motion artefacts. It has been shown that a 3D GRASE PROPELLER (3DGP) readout is able to retrospectively correct in-plane rigid body motion in ASL perfusion images [1]. Through-plane motion is indirectly addressed by underweighting the affected data. This is problematic for ASL due to the low overall SNR. To this aim, we demonstrate a novel 3DGP ASL reconstruction pipeline, which includes a 6-parameter 3D rigid body registration, to allow correction for through-plane motion and thus exploiting a maximum of the acquired data.

Subjects and Methods: Four measurements were performed on a 3 T scanner (MAGNETOM Skyra) of which three included a single predefined rotational motion along the x-/y-/z-axis, respectively, starting after half the acquisition time. Imaging was performed using a pseudo-continuous 3DGP ASL sequence with a label duration of 1.8 s and post-labeling delay of 1.7 s and 4 Label/Control bricks with a 96 × 32 × 24 matrix. Additional parameters were: ETL 32, TR/TE = 4300 ms/21.5 ms, 4 mm isotropic voxel size, 0.5 ms echo spacing, background suppression, 9 averages; resulting in 5:10 min total measurement time. A scheme of the 3DGP sequence is shown in Fig. 1a. Fig. 1b depicts the proposed image reconstruction pipeline. All reconstruction steps are implemented as C ++-Gadgets [2]. Image registration is performed using ITK [3]. The algorithm is verified by analyzing he quality of reconstructed perfusion images as well as calculated trajectories.

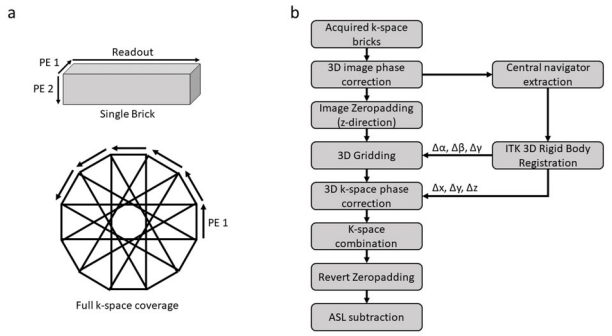

Fig. 1: a) 3DGP acquisition scheme; b) Proposed reconstruction pipeline. Estimated rotations are integrated in the gridding procedure while subject translations are transferred to linear phase ramps, that are removed from each brick afterwards.

Results: The reconstructed perfusion images are shown in Fig. 2. Without motion correction (MOCO OFF), perfusion maps show areas with increased blurring (cf. arrows). Using our proposed correction algorithm (MOCO ON), these areas reveal finer structures, giving good accordance with the reference images (REST). Estimated motion parameters are shown in Fig. 3. The defined motion protocol including rotations around a single axis is visibly identified by the algorithm at half the acquisition time.

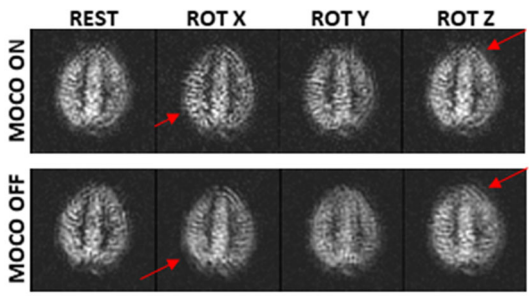

Fig. 2: Reconstructed perfusion images.

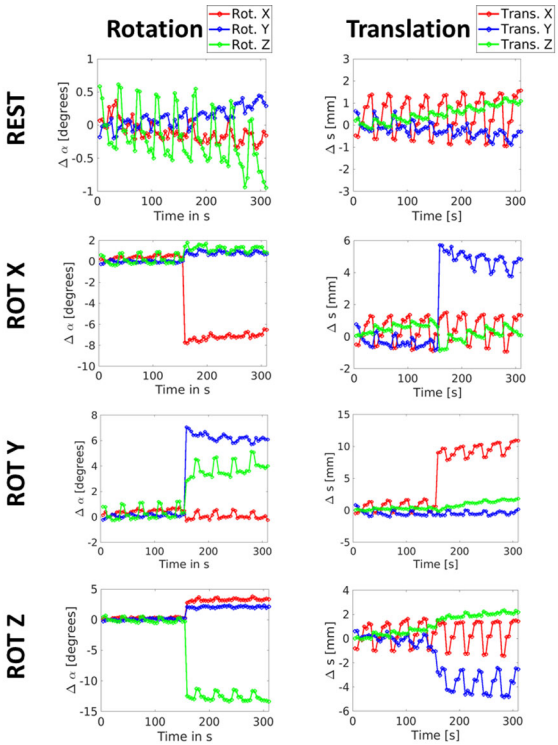

Fig. 3: Rotation and translation estimates for the given motion strategy. Visible systematic oscillations are due to 3DGP specific signal shifts resulting from magnetic field inhomogeneities.

Discussion/Conclusion: We have demonstrated that reliable 3D rigid body parameters can be estimated from low-resolution 3DGP navigators. Systematic fluctuations in estimated motion are linked to different directions of geometric distortion in each brick. Hence, integration of self-referred distortion correction may further increase the accuracy of motion estimates. As a future perspective, a combination of prospective and retrospective motion correction for ASL using 3DGP will be investigated.

Acknowledgments

This work was supported by the FhG Internal Programs under Grant No. Attract 142-600172.

References:

[1] Tan et al. MRM 2011;66:168–173.
[2] Hansen and Sørensen. MRM 2013;69:1768–1776.
[3] Yoo et al. IOS Press 2002:586–592.

P02.10

Novel pixel-based approach for artifact evaluation of passive implants in MRI validated on intruterine devices at 3T

I. Brumer, **A. Adlung**, W. Neumann, T. Uhrig, M. Malzacher, L. R. Schad, F. G. Zöllner

Computer Assisted Clinical Medicine, Medical Faculty Mannheim, Heidelberg University, Mannheim, GERMANY

Purpose/Introduction: Magnetic Resonance Imaging (MRI) at higher magnetic field strengths is becoming more common in clinics but is more prone to artifacts[1], like susceptibility artifacts induced by implants. The ASTM F2119 standard[2], which has been established to assess MR signal attenuation induced by passive metallic implants,

suggests taking the maximum rectangular area around the artifact in a single slice. Potential drawbacks of this approach are sensitivity to outlier pixels and spatial misrepresentation of implants[3]. We compare the ASTM F2119 to a novel pixel-based approach in both 2D and 3D using metal-containing intrauterine devices (IUDs) in a phantom as an example for passive implants which have high clinical relevance.

Subjects and Methods: Images were acquired at 3T (Siemens MAGNETOM Skyra, 32-channel spine coil) with a gradient echo sequence (TE/TR = 16/61 ms, voxel size = 1.1 × 1.1 × 1.5 mm^3). Seven types of IUDs made of different materials (Fig. 1) were consecutively placed in a soft tissue-mimicking phantom (1000 g of distilled water, 3.75 g of $NiSO_4$ and 5 g of NaCl). Reference images were acquired after each IUD scan. A pixel was defined as an artifact if the pixel's magnitude in the image with IUD differed by > 30% from its reference[2]. Artifacts were calculated using Matlab [The MathWorks Inc. USA]. In 3D, all slices with artifacts were considered (volume artifact), and in 2D only the slice with maximum artifact (area artifact). We compare two approaches (Fig. 2):

(I) Area-based: rectangle containing all artifact pixels (ASTM F2119 procedure);

(II) Pixel-based: sum of all pixels classified as artifacts.

Results: The calculated artifact areas and volumes for both approaches are shown in Fig. 3. As expected, artifacts were larger with approach I than II since approach I is sensitive to outlier pixels, which can increase the artifact with little consequence on image quality (Fig. 3: largest relative difference in 2D (90%) and 3D (85%) for CuT-380A-QL IUD). Overall, the area artifacts determined by approach I and II differed significantly (student's paired t-test). Across all approaches, models containing steel or nitinol components displayed the largest artifacts.

Discussion/Conclusion: We have presented a novel approach to evaluate artifacts of passive implants in MRI. Our evaluation, based on IUDs imaged at 3T, shows that the pixel-based approach describes induced artifacts in a better way than the ASTM F2119. The 3D properties of implants should be taken into account for artifact evaluation as implants' artifacts extend over multiple slices, thus affecting image quality differently than apparent with 2D standard artifact evaluation. A re-evaluation of the current artifact quantification standard could thus improve the comparability of implant-induced artifacts and lead to an improved assessment of clinically relevant reduction in image quality.

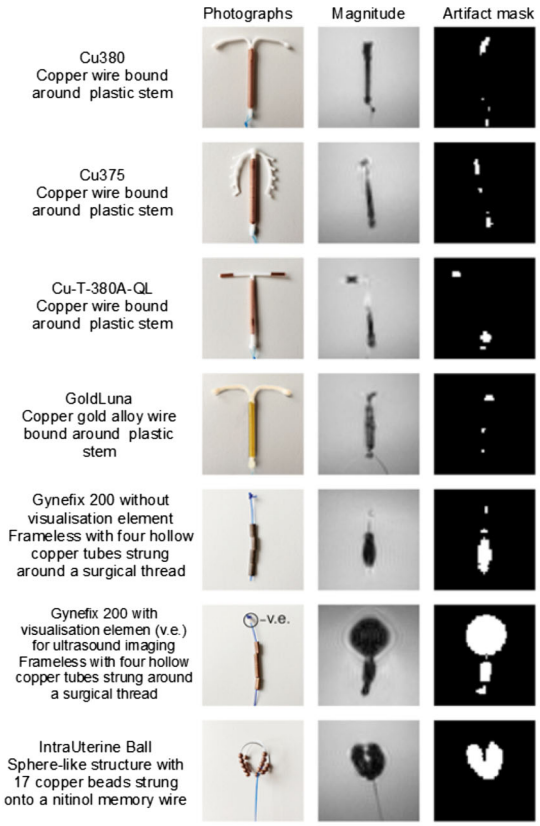

Figure 1: Overview of the seven tested IUD models: name and description of components, photographs, MR magnitude images acquired with a gradient echo sequence, and artifact masks according to the ASTM standard.

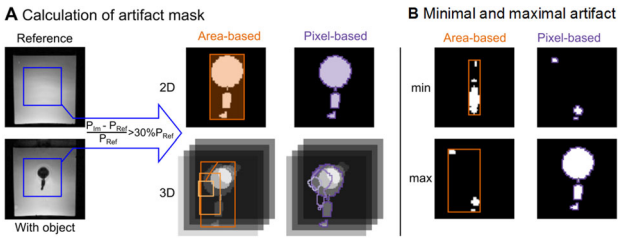

Figure 2: Schematic representation of the two procedures. A: Reference and implant image in the field of view, and calculated artifact masks. B: Minimal and maximal artifacts for both approaches in 2D for the Gynefix 200 without v.e.

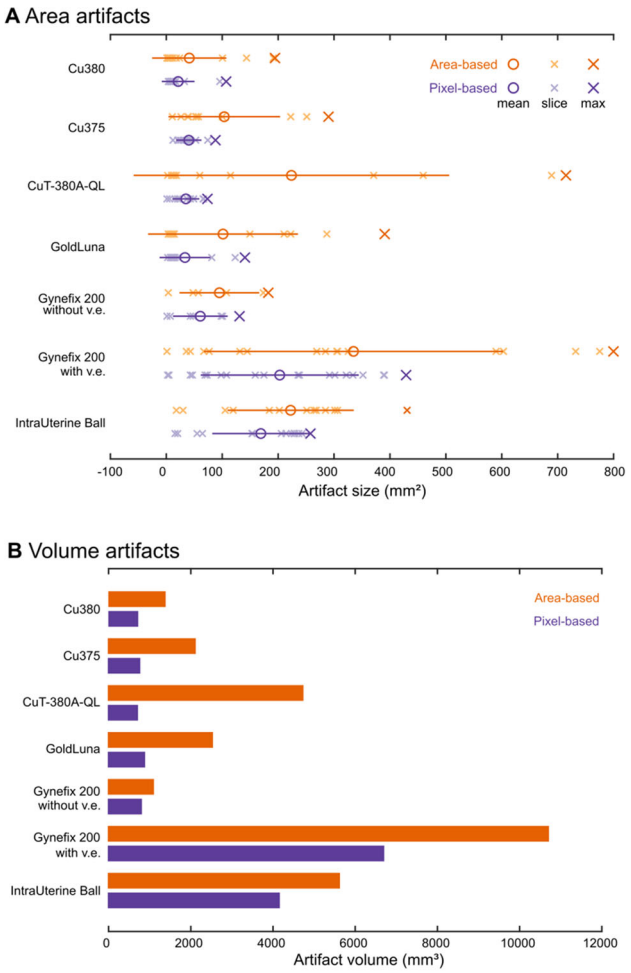

Figure 3: Area and volume artifacts for all IUDs for both procedures: approach I in orange and II in purple. Size values are shown for individual slices (light color), as mean over all slices with standard deviation and maximum value (bright color).

References:
[1] Bernstein J MI 2006.
[2] ASTM Standard F2119 2007.
[3] Neumann Eur Radio 2018.

P02.11

Robust outlier detection for diffusion kurtosis MRI based on IRLLS

V. Anania[1], T. Billiet[1], B. Jeurissen[2], J. Sijbers[2], A. J. den Dekker[2]

[1]*icometrix, Research and Development, Leuven, BELGIUM,* [2]*imec—Vision Lab, University of Antwerp, Department of Physics, Antwerp, BELGIUM*

Purpose/Introduction: The diffusion tensor imaging (DTI) model is the most commonly applied to extract quantitative measures from diffusion weighted images, yet recent literature has shown that the diffusion kurtosis imaging (DKI) model can provide additional information in clinical applications [1]. Unfortunately, the quality of the estimated metrics can be affected by several types of artifacts, many of which produce outliers in the intensity of the signal. To deal with these outliers, recently, two linear, outlier-robust, voxel-wise estimation methods have been proposed: REKINDLE [3] and IRLLS [2].

Whereas REKINDLE was specifically designed to detect outliers in DKI data, IRLLS was introduced in the framework of DTI. However, the authors already pointed out that its extension to DKI is straightforward [2]. In this work, such an extension is performed, along with a simple but effective modification of the method, which involves the removal of the goodness of fit pre-processing step [2]. Additionally, the performance of the thus upgraded version of IRLLS is compared to REKINDLE.

Subjects and Methods: Diffusion weighted signals were generated with a DKI protocol consisting of 5 b_0 images and 60 gradient directions per shell (b = 1200 and 2500 s/mm^2) [3]. We simulated 20,000 signal realizations with the same underlying ground truth diffusion parameters. Experiments were carried out for different SNRs (defined on the b_0 images), with different types of outliers (50% signal decrease/increase) and with 2 percentages of outliers (0% and 5%). The b_0 data points were not corrupted with outliers.

Results: Figs. 1–2 suggest that, in the presence of outliers, the upgraded IRLLS method outperforms the original version in terms of mean squared error (MSE) of diffusion and kurtosis metrics. This improvement appears more noticeable at lower SNRs and for outliers that manifest as a reduction in the signal intensity. In contrast, in the case of outlier-free diffusion signals, the goodness of fit step is beneficial since it prevents us from detecting false positives.

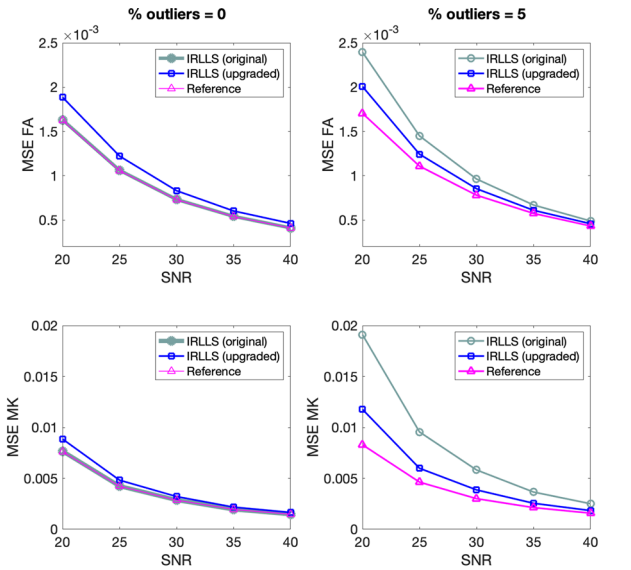

Fig. 1: MSE of FA and MK as a function of SNR for 0% (left) and 5% (right) outliers, simulated as 50% decrease in the signal intensity. Both versions of IRLLS are compared to an iterative WLLS after complete outlier removal (reference).

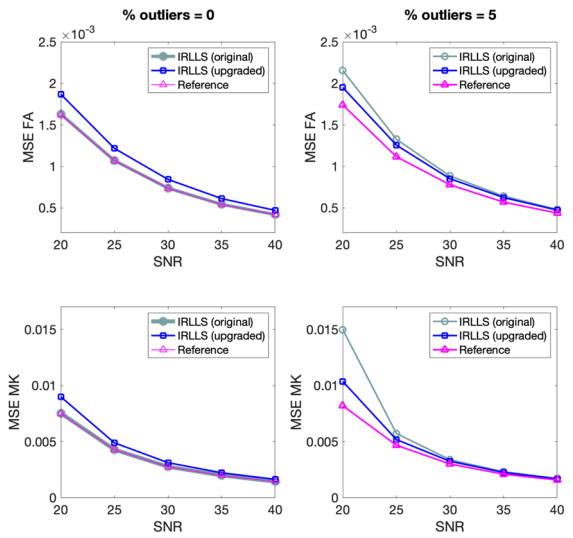

Fig 2: MSE of FA and MK as a function of SNR for 0% (left) and 5% (right) outliers, simulated as 50% increase in the signal intensity Both versions of IRLLS are compared to an iterative WLLS after complete outlier removal (reference).

Figure 3 shows that the outlier detection steps of the upgraded IRLLS method and REKINDLE exhibit similar sensitivity and specificity performance.

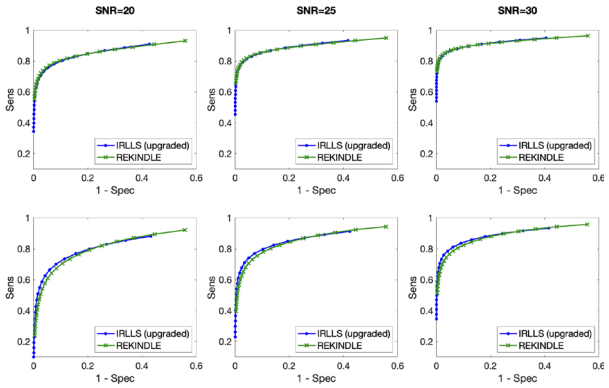

Fig. 3: Performance of the outlier detection steps of IRLLS and REKINDLE as a function of the decision threshold, set from 6 to 0.5 (0.25 step size). Outliers (5%) were simulated as 50% decrease (top) or increase (bottom) in the signal intensity.

Discussion/Conclusion: While the application of a goodness of fit criterion in IRLLS is beneficial in the absence of outliers in the data, we show that this step can hamper the outlier detection especially at lower SNRs. A fair comparison between IRLLS and REKINDLE in terms of diffusion parameter estimation quality is critically dependent on the choice of the decision threshold, which will be subject of future work.

We acknowledge Chantal Tax for providing us with the Matlab code of REKINDLE. This study was partially funded by the B-Q Minded EU H2020 project (grant agreement No. 764513).

References:

1. Rosenkrantz et al. JMRI, 42(5), 1190–1202, (2015).
2. Collier et al. MRM, 73(6), 2174–2184, (2015).
3. Tax et al. MRM, 73(2), 794–808, (2015).

P02.12

GROG Based Compressed Sensing for Accelerated Radial MRI

M. H. Hassan[1], R. Zainab[1], I. Aslam[2], K. Afsar[1], H. Omer[1]

[1]COMSATS University Islamabad, Electrical and Computer Engineering, Islamabad, PAKISTAN, [2]Hospital University of Geneva, Department of Radiology and Medical Informatics, Geneva, SWITZERLAND

Purpose/Introduction: Non-Cartesian trajectories are helpful to speed-up the MR scan time but may result in complex artefacts. This work proposes a GROG based Compressed Sensing (GROG-CS) solution for accelerated radial MRI to get the unaliased images. At first, the proposed method maps the under-sampled non-Cartesian k-space data onto a Cartesian grid using GROG and then iterative Conjugate Gradient based CS with Total Variation (TV) constraint is applied to obtain final image.

In-vivo human head data is used for testing the proposed scheme. The experimental results are compared with the conventional NUFFT based CS reconstruction. The proposed method (GROG-CS) provides improved images in comparison to the NUFFT based CS reconstruction.

Subjects and Methods: GROG [1] uses multi-coil weight-sets to resamples the non-Cartesian data onto a Cartesian grid and leaves some empty positions [1]. GROG gridding is more advantageous than conventional gridding techniques e.g. Convolution [2] and NUFFT [3] as it doesn't require density compensation and interpolation kernel with different sizes and shapes [1].

This paper proposes an application of GROG [1] in CS with TV constraint [4] to get the final MR images using radial k-space data. Since, some empty positions are randomly left by GROG in the gridded k-space, it leads to noise like artifacts, therefore GROG gridding is a good choice for CS based reconstruction. Figure 1 shows a schematic model of the proposed method.

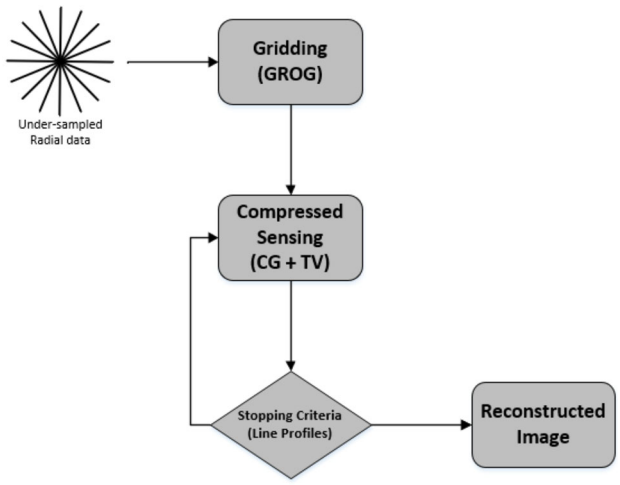

Figure 1: Schematic Diagram of the Proposed Method (GROG-CS)

As a stopping criteria, the correlation measure (tolerance value = 0.999 in our experiments) between the central line profiles of the reconstructed images in the current and previous iterations is used [5].

Results: The proposed scheme (GROG-CS) is validated on the 1.5T human head data. Using Fessler toolbox the data set is initially encoded into fully sampled radial k-space and AF is calculated as given in [6].

The solution images of the proposed method (Row A) and conventional NUFFT based CS (Row B) are shown in Figure 2. Experiments are performed on human head data having AF 4, 6 and 7 with 101, 67 and 57 radial spokes respectively.

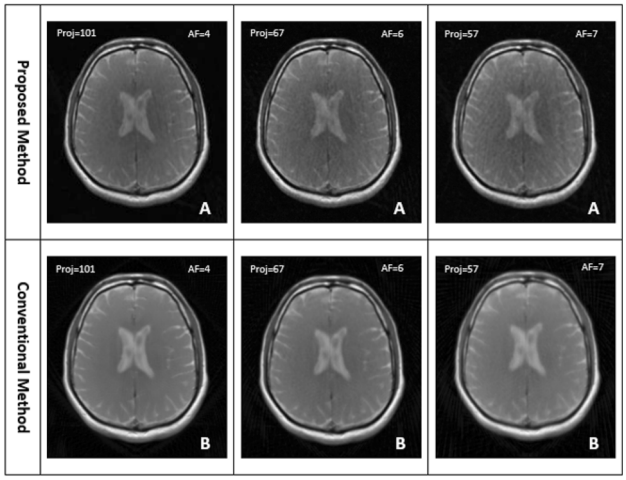

Figure 2: Reconstruction results of 1.5T human head data using Proposed method (GROG-CS) {Row A} and Conventional NUFFT based CS {Row B}

Table 1 shows results in terms of quantifying parameters. The results illustrate that the reconstruction results for proposed scheme out-performs the conventional approach (e.g. 74%, 54% and 10% improvement in AP, RMSE and PSNR respectively at AF=4 for in-vivo 1.5T human head dataset in our experiments).

Acceleration Factor	Proposed Method (GROG + CS)			Conventional Method (NUFFT + CS)			% Improvement of Proposed Method w.r.t Conventional Method		
	AP	RMSE	PSNR	AP	RMSE	PSNR	AP	RMSE	PSNR
AF = 4	0.0050	0.0175	83.3146	0.0193	0.0383	75.2414	74%	54%	10%
AF = 6	0.0076	0.0218	81.3856	0.0245	0.0443	74.4906	69%	50%	9%
AF = 7	0.0090	0.0233	80.8039	0.0302	0.0635	72.1134	70%	63%	12%

Table 1: Reconstruction results of 1.5T human head data in terms of AP, RMSE and PSNR. % improvement section represents the improvement achieved with the proposed method (GROG-CS) as compared to conventional method (NUFFT based CS)

Table 1 shows results in terms of quantifying parameters. The results illustrate that the reconstruction results for proposed scheme out-performs the conventional approach (e.g. 74%, 54% and 10% improvement in AP, RMSE and PSNR respectively at AF = 4 for in vivo 1.5T human head dataset in our experiments).

Discussion/Conclusion: This work proposes a new method (GROG-CS) to reconstruct the solution image instead of the conventional NUFFT based CS approach. The reconstruction results depict that optimal quality images are provided by proposed method in comparison to the conventional scheme.

References:

1. N. Seiberlich et.al. MRM 2008, 930–935.
2. J. I. Jackson et.al. IEEE 1991, 473–478.
3. J. A. Fessler et.al. IEEE 2003, 560–574.
4. M. Lustig et.al.MRM 2007, 1182–1195.
5. M. Khan et.al.APMR 2017, 227–240.
6. I. Aslam et.al.APMR 2017, 107–124.

P02.13

Reconstruction of under-sampled Radial MRI using SC-GROG followed by Singular Value Thresholding (SVT) based CS

H. J. Bhatti[1], F. Aamir[1], I. Aslam[2], H. Omer[1]

[1]COMSATS University Islamabad, Electrical and Computer Engineering, Islamabad, PAKISTAN, [2]Hospital University of Geneva, Department of Radiology and Medical Informatics, Geneva, SWITZERLAND

Purpose/Introduction: In pMRI, undersampled non-Cartesian trajectories are used to speed up the MR scan time but lead to artifacts in the final images. This paper proposes Singular Value Threshold (SVT) [1] along with self-calibrated GROG [2] (SC-GROG) for CS based reconstruction to get the unaliased MR images from the under-sampled radial k-space data.

Proposed scheme is validated on 1.5T human head data and compared with the conventional pseudo-Cartesian GRAPPA approach. Proposed method show better results both visually and qualitatively i.e. 83%, 60% and 11% improvement in terms of AP, RMSE and PSNR at AF = 4.

Subjects and Methods: SC-GROG [2] maps the non-Cartesian k-space data to the Cartesian grid via coil-by-coil self-calibrated weight sets. Conventionally, pseudo-Cartesian GRAPPA has been proposed with SC-GROG for the reconstruction of unaliased MR images [2].

In this work, SC-GROG with CS based SVT (GROG-SVT) is proposed to get the artifact free MR images from under-sampled radial k-space data. In proposed method, SC-GROG is used to map the acquired non-Cartesian data of k-space onto the adjacent Cartesian place. In the next stage, receiver coil sensitivity maps, estimated from center of GROG gridded data using self-calibration [3] scheme, along CS based SVT is utilized to get the solution image (Figure 1). The proposed method optimization problem as Lagrangian expression is:

$$\min_m \|F_u.C.m - y_g\|_2^2 + SVT_\lambda\,(m)$$

Where,

F_u = Under-sampled Fourier operator

C = Receiver coil sensitivity profiles

m = desired recon. image

y_g = GROG gridded k-space (i.e. $y_g = G.y_r$ where G: GROG operator, y_r: radial data)

SVT = Singular value thresholding function (i.e. $SVT_\lambda\,(m) = U.\lambda(S).V^t$; here t is conjugate transpose, U and V are unitary matrices, S is a square diagonal matrix consisting of singular values $(\sigma_1,\sigma_2,\ldots\sigma_N)$

λ = thresholding parameter ($\lambda = 0.6 \times 10^{-3}$ chosen empirically) which used to retain the most important singular values.

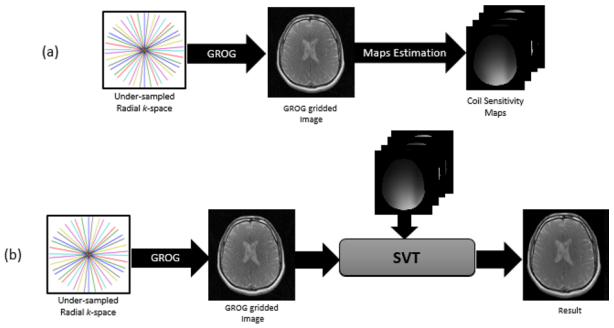

Figure 1: Block diagram of the proposed method (a) Sensitivity Maps estimation from the GROG gridded data using self-calibration method[3] (b) Reconstruction pipeline of the proposed scheme

Results: The proposed work is validated on 1.5T human head data acquired at St. Mary Hospital, London having dimensions 256 × 256 × 8 with TR/TE = 500/10 ms and Flip Angle = 50°. Initially, human head data is retrospectively converted to a fully sampled radial *k*-space using Fessler toolbox and following formula: $(\pi/2) \times$ FOV [4].

Figure 2 and Table 1 shows the results of the proposed method (GROG-SVT) and the GROG with Pseudo-Cartesian GRAPPA[7] in terms of AP, RMSE and PSNR at AF 4, 6 and 9.

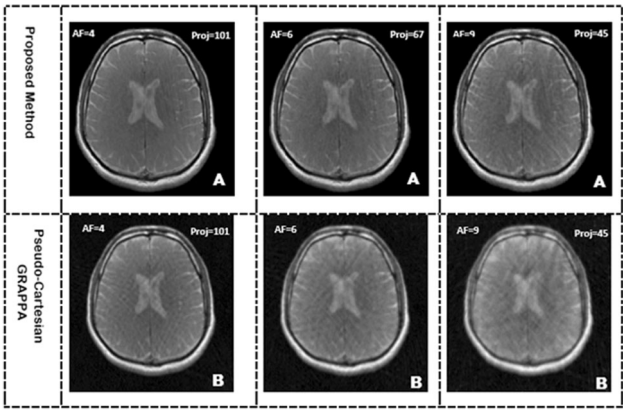

Figure 2: Reconstruction results of 1.5T GE scanner human head data for the proposed method (Row A) and conventionally used pseudo-Cartesian GRAPPA (Row B). at AF= 4,6 and 9.

Proposed work provides better reconstruction results both visually and in terms of quantifying parameters (i.e. 83%, 60% and 11% improvement in AP, RMSE and PSNR at AF = 4 respectively.

	Proposed Method (GROG with SVT)			Pseudo-Cartesian GRAPPA			% Improvement of Proposed Method w.r.t Conventional Method		
Acceleration Factor	AP	RMSE	PSNR	AP	RMSE	PSNR	AP	RMSE	PSNR
AF = 4	0.0048	0.0171	83.4879	0.0297	0.0425	75.6025	83%	60%	11%
AF = 6	0.0066	0.0200	82.1473	0.0683	0.0644	71.9886	90%	69%	14%
AF = 9	0.0146	0.0298	78.6902	0.0998	0.0778	70.3448	85%	62%	12%

Table 1: Reconstruction results of 1.5T GE scanner human head image using the proposed method and Pseudo-Cartesian GRAPPA in terms of AP, RMSE and PSNR at AF= 4,6 and 9

Discussion/Conclusion: This paper presents GROG-SVT to reconstruct the highly under-sampled radial *k*-space data iteratively and eliminate the need of ACS lines and weight estimation patterns that used in pseudo-Cartesian GRAPPA approach.

References:

1. R. Otazo et.al. MRM 2015,1125–36.
2. N. Seiberlich et.al. MRM 2008,1127–37.
3. M A Griswold et al. NMRB 2006,316–24.
4. I. Aslam et.al. APMR 2018,107–24.

P02.14

Koch Snowflake Fractal RF Surface Coils to Improve ^{23}Na—Magnetic Resonance Imaging at 3T

C. Nowikow[1], N. Konyer[2], P. Yazdanbakhsh[3], M. Noseworthy[4]

[1]McMaster University, School of Biomedical Engineering, Hamilton, CANADA, [2]St. Joseph's Healthcare, Imaging Research Centre, Hamilton, CANADA, [3]Ceresensa Inc., Toronto, CANADA, [4]McMaster University, Electrical and Computer Engineering, Hamilton, CANADA

Purpose/Introduction: The significantly lower signal-to-noise ratio (SNR) of sodium (^{23}Na) MRI, compared to proton (^{1}H)-MRI [1] justifies interest in developing improvements to create higher quality ^{23}Na-MR images. While developments have been made in pulse sequence design, image reconstruction, and approaches to image filtering [1], RF hardware is not often considered as many believe it to be already optimized. However, the aim of this project *is hardware*, based on newer approaches to RF engineering. Fractal antennas have been used in far-field systems including cellphones for years [2] and so we propose that a fractal geometry surface coil design will produce improved images compared to that of a standard circular surface coil. It is hypothesized that a fractal design will produce a higher amplitude B_1^+ field with improved homogeneity [3, 4] and therefore higher SNR.

Subjects and Methods: Two coils were simulated using HFSS [5]: a simple circular surface (SCS) coil, and a third generation Koch snowflake fractal surface (KSFS) coil. A Koch snowflake geometry was chosen because: (1) it closely resembles the geometry of a circular loop; (2) preliminary simulations were performed and it showed potential for ^{129}Xe imaging [2], whose gyromagnetic ratio is very close to ^{23}Na; and (3) it has been shown that a KSFS coil design can provide a small increase in SNR in ^{1}H—MRI [3]. Both coils were simulated as thin copper strips mounted on a RO4350 substrate with an air radiation box above and loaded box of saline below (Fig. 1). The coils were then compared on the magnitude and homogeneity of the H field produced and the magnitude of the E field.

Results: It was found by measuring the far field radiation that the KSFS coil had a higher mean H field (67.31A/m) than the SCS coil (13.75 A/m), along with the added benefit of a lower maximum E field (15946.07 V/m for the KSFS, 26321.31 V/m for the SCS). Furthermore, the KSFS coil gave a more planar H field in the load (Fig. 2), than in its SCS coil counterpart (Fig. 3), which creates a more spherical H field in the load.

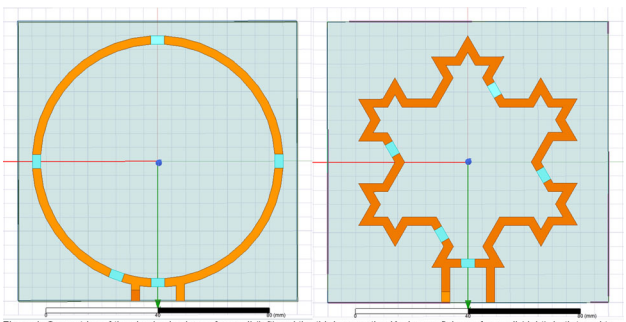

Figure 1: Geometries of the simple circular surface coil (left) and the third generation Koch snowflake surface coil (right), both tuned to 33.8MHz (the frequency of 23Na in a GE MR750 scanner) and impedance matched to 50Ω

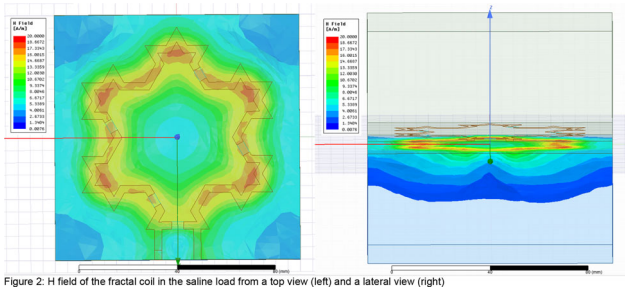

Figure 2: H field of the fractal coil in the saline load from a top view (left) and a lateral view (right)

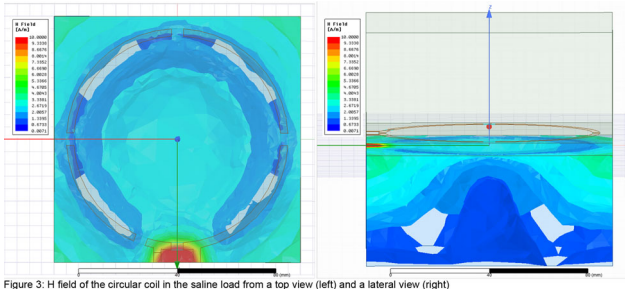

Figure 3: H field of the circular coil in the saline load from a top view (left) and a lateral view (right)

Discussion/Conclusion: Simulations support the hypothesis that a Koch fractal design provides a B_1^+ field that is greater in magnitude and homogeneity than that of a standard surface coil, however further generations of the Koch need to be explored, along with different radii, as well as other fractal geometries.

References:

[1] G. Madelin, J. Lee, R. Regatte and A. Jerschow, "Sodium MRI: Methods and applications", *Progress in Nuclear Magnetic Resonance Spectroscopy*, vol. 79, pp. 14–47, 2014.

[2] Cohen, Fractal antenna applications in wireless telecommunication IEEE Prof Prog Proc, 1997.

[3] O. Dona Lemus, N. Konyer and M. Noseworthy, "Micro-strip Surface Coils Using Fractal Geometry for 129Xe Lung Imaging Applications", in *ISMRM*, 2018.

[4] S. Ha, W. Roeck and O. Nalcioglu, "Fractal RF Coils for Magnetic Resonance Imaging", US 2015/0048828, 2015.

[5]ANSYS HFSS, by Ansoft, Version 19.2.0

P02.15

Calibrationless Parallel Imaging with Compressed Sensing for GROG based Radial MRI

R. Zainab[1], M. H. Hassan[1], I. Aslam[2], H. Omer[1]

[1]*COMSATS University Islamabad, Electrical and Computer Engineering, Islamabad, PAKISTAN,* [2]*Hospital University of Geneva, Department of Radiology and Medical Informatics, Geneva, SWITZERLAND*

Purpose/Introduction: Within the scope of parallel imaging and compressed sensing (pMRI-CS), many diverse methods have been developed in literature in order to get the artefact free MR images from the accelerated non-Cartesian trajectories [1–3]. This paper proposes a new method "Calibrationless parallel imaging with compressed sensing (CS) for GROG gridded Radial MRI" to get unaliased Images. Shepp-Logann phantom is used to validate the proposed method and results are comaperd with conventional 'GROG based Pseudo-Cartesian GRAPPA' [1] and 'GROG followed by ESPIRiT' [2].

Subjects and Methods: Using multi-coil weight sets, GROG[1] resamples the acquired non-Cartesian data onto a Cartesian grid and leaves some empty positions in the gridded *k*-space [1].

In thiswork, calibrationless pMRI with CS is proposed to reconstruct the GROG gridded radial MRI data. In the proposed scheme, initially the under-sampled radial data is mapped onto a Cartesian grid using GROG. Then from center of the GROG gridded data, a set of receiver coil sensitivity profiles are estimated using auto-calibration method [4]. Finally, these sensitivity maps are incorporated with iterative conjugate gradient based CS [5] to efficiently reconstruct the artefact free images. The depiction of the proposed scheme is shown in Figure 1.

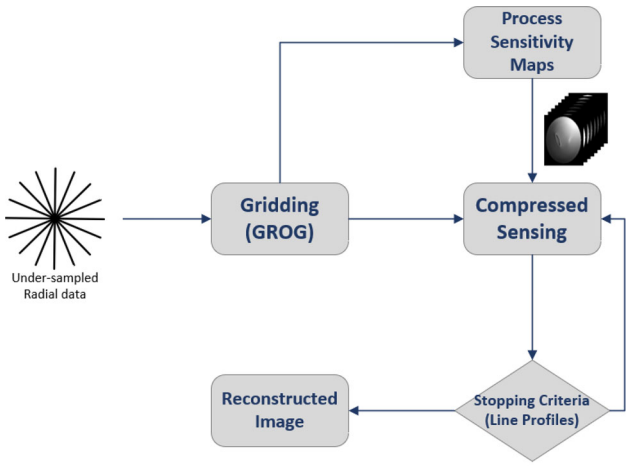

Figure 1: Schematic Diagram of the proposed reconstruction technique. After GROG gridding, receiver coil sensitivity maps are estimated and then incorporated in CS to get the solution image

As a stopping criterion, the correlation measure (i.e. a value of 0.999 empirically chosen from a range of values) between the central line profiles of the reconstructed images in the current and previous iterations is used [6].

Results: Figure 2 shows the optimal quality reconstruction results of the proposed method (Row A) as comapred to GROG followed by ESPIRiT (Row B) and GROG based pseudo-Cartesian GRAPPA (Row C) for Shepp-Logan phantom at AF = 4, 6 and 7 with 101, 67 and 57 radial spokes respectively.

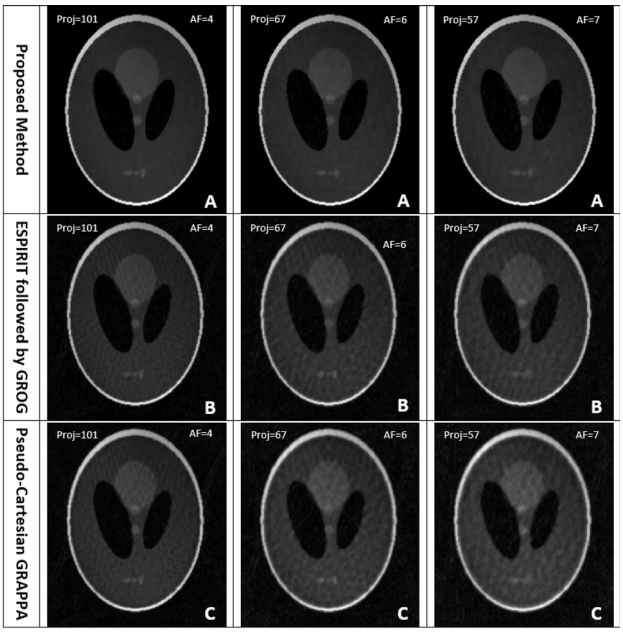

Figure 2: Shepp-Logan phantom reconstruction results using the Proposed Method (Row A), GROG followed by ESPIRiT (Row B) and GROG based pseudo-Cartesian GRAPPA (Row C) at AF= 4, 6 and 7 with 101, 67 and 57 radial spokes respectively.

Along with visual assessment, the proposed scheme also outperforms in terms of quantifying parameters for as given in Table 1 e.g. 95% improvement in AP, 80% in RMSE and 18% in PSNR at AF = 4 than GROG based pseudo-Cartesian GRAPPA [1] whereas 63% improvement in AP, 36% in RMSE and 5% improvement in PSNR than the conventionally used GROG with ESPIRiT [2].

Acceleration Factor	Proposed Method			GROG followed by ESPIRiT			GROG based pseudo - Cartesian GRAPPA		
	AP	RMSE	PSNR	AP	RMSE	PSNR	AP	RMSE	PSNR
AF = 4	0.0030	0.0086	89.4462	0.0081	0.0136	85.5056	0.0771	0.0438	75.3432
AF = 6	0.0042	0.0102	88.0021	0.0171	0.0209	81.7676	0.1446	0.0599	72.6139
AF = 7	0.0047	0.0108	87.4657	0.0212	0.0239	81.7054	0.1929	0.0692	71.3622

Table 1: Reconstruction results of Shepp-Logann phantom in terms of AP, RMSE and PSNR using proposed method, GROG followed by ESPIRiT and GROG with pseudo-Cartesian GRAPPA at AF=4, 6 and 7.

Discussion/Conclusion: This work proposes an auto-calibrated pMRI based CS reconstruction using GROG for accelerated radially encoded *k*-space data. The results show that the proposed algorithm efficiently recovers the solution image as compared to the conventional GROG based ESPIRiT and pseudo-Cartesian GRAPPA schemes.

References:

1. N. Seiberlich et.al. MRM 2008, 1127–1137.
2. I. Aslam et.al. APMR 2018,107–124.
3. T. Block et.al. MRM 2007,1086–1098.
4. M. A. Griswold et al. NMRB 2006, 316–324.
5. M. Lustig et.al. MRM 2007,1182–1195.
6. M. Khan et.al. APMR 201, 227–240.

P02.16

Commissioning of a low-field rampable magnet for a high-resolution MRI system

J. P. Rigla Pérez[1], M. Corberan[2], D. Grau-Ruiz[1], P. Borreguero[2], J. M. Gonzalez[1], E. Pallas[2], A. Rios[1], J. Alonso[2], J. M. Benlloch[2]

[1]*Tesoro Imaging S. L., Valencia, SPAIN,* [2]*Institute for Instrumentation for Molecular Imaging (i3 M), Spanish National Research Council (CSIC), Valencia, SPAIN*

Purpose/Introduction: The HISTO-MRI project [1] aims to developed a pre-clinical MRI system to obtain in vivo imaging of deep tissues with histological resolution. In order to achieve this objective, this MRI system will have a main magnetic system based on an electromagnet rampable from 0 to 1 T with a high magnetic field homogeneity and ultra-fast (< 10 μs) and strong gradient fields (2.4 T/m) [2]. In this work, we present the commissioning of an electromagnet for a low-field (0.1T) carried out in the MRILab at the i3 M.

Subjects and Methods: The main magnetic system is a conventional electromagnet with a classical "H"-shaped structure (see Fig. 1). The dimensions and the weight of the magnet are 594 × 452 × 540 mm^3 and 907 kg, respectively. A description of the electromagnet design can be found in [3]. This electromagnet uses a Danfysik 9100 Unipolar current supply and a SMC HRS060 cooling system. Monitoring of the water flow and temperature is REALIZED by two flowmeters (SMC HRS-PF3W540) located at the input and exit of the electromagnet. The magnetic characterization was carried out using a Hall sensor (Metrolab THM1176-MF) attached to a 3D positioning system available at the MRILab.

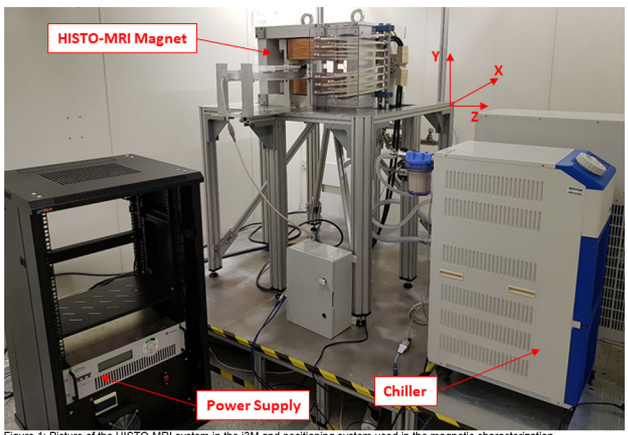

Figure 1: Picture of the HISTO-MRI system in the i3M and positioning system used in the magnetic characterization.

Results: In order to determine the magnet homogeneity, the magnetic properties of the electromagnet were measured at the median plane (XZ-Plane and Y = 0) in a region of 50 × 50 mm^2, the diameter magnetic pole is 250 mm). The magnetic field measurements were taken every 1 mm. The magnetic field profiles along the X (Z = Y=0) and Z-axes (X = Y=0) are shown in Fig. 2. The experimental measurements suggest that in the FoV (spherical region with a diameter of 20 mm) the magnetic field homogeneity of the electromagnet is approximately 293 ppm. This value is insufficient to obtain for high resolution MRI images (< 10 ppm). This can be further improved by means of a shimming system. We have also studied the thermal behavior of the electromagnet. The maximum temperature increase throughout the coil was observed in the cooling system for 1 T (186 A), 5.9 K. For 0.1 T (17.8 A) the jump is negligible, see Fig. 3.

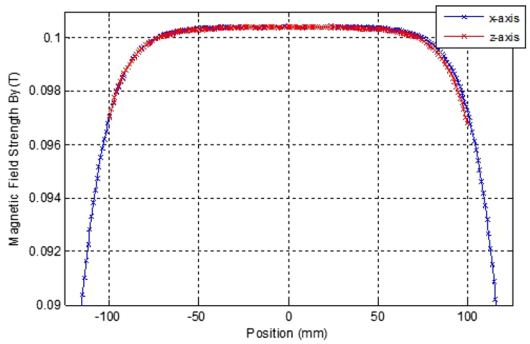

Figure 2: Magnetic field strength for 0.1 T in transversal (X-axis) and axial (Z-axis) directions in the median plane (Y=0) of the electromagnet.

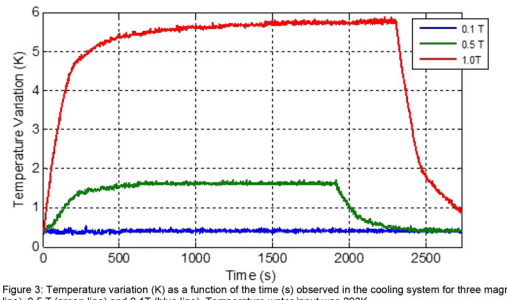

Figure 3: Temperature variation (K) as a function of the time (s) observed in the cooling system for three magnetic field values: 1T (blue line), 0.5 T (green line) and 0.1T (blue line). Temperature water input was 293K.

Discussion/Conclusion: The commissioning of the main magnetic system was carried out. The thermal behavior and the magnetic properties of the system were studied. The value of the magnetic field homogeneity is < 300 ppm and can be shimmed further.

References:

[1] HISTO-MRI Project, http://www.histo-mri.i3m.upv.es/.
[2] D.Grau et al., *Patent Application* US P201830448 (2018).
[3] J.P. Rigla et al., arXiv:1808.05795 (2019).

P02.17

GPU Accelerated GRAPPA Reconstruction for Real-time Cardiac MRI

H. Akram, Z. Laraib, O. Inam, M. Qureshi, H. Omer

COMSATS University Islamabad, Department of Electrical and Computer Engineering, Islamabad, PAKISTAN

Purpose/Introduction: In conventional GRAPPA [1] (a pMRI technique), the handling and processing of massive multichannel MR data limit its performance in terms of reconstruction time for real-time cardiac MRI [1]. Recently, Graphics processing units (GPUs) have emerged as a viable solution to adhere to the rising demands of fast data processing in parallel MRI techniques [2]. This paper presents a new GPU based framework for GRAPPA for efficient cardiac MR image reconstruction. The proposed method accelerates the GRAPPA reconstruction process by harnessing the large computational power of GPUs using an advanced parallel programming model called Compute Unified Device Architecture (CUDA).

Subjects and Methods: The conventional GRAPPA reconstruction algorithm constitutes two phases i.e. calibration and synthesis which involve numerous computation hungry operations such as sequential kernel repetitions, solving large over-determined linear equations for the estimation of GRAPPA weights and complex sequential convolutional kernel fittings for interpolating the missing lines in the undersampled *k*-space of multiple receiver coils. In the proposed method, an efficient and parameterizable GPU based parallel framework for GRAPPA reconstruction is presented. The proposed method addresses the computational bottlenecks of conventional GRAPPA by exploiting the fine-grained parallelism in the GRAPPA reconstruction process using six optimized CUDA kernels (Figure 1).

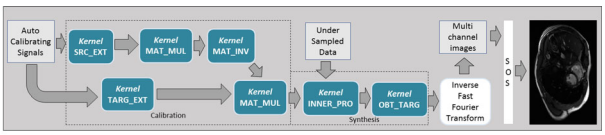

Figure 1: The proposed GPU implementation of GRAPPA using optimized kernel

The proposed CUDA kernels incorporate parallel GRAPPA kernel fittings, parallel complex matrix–matrix multiplications and complex matrix inversions using parallel Gauss-Jordan elimination method [3] for fast data processing. The performance of the proposed GPU-based GRAPPA is evaluated by reconstructing 10 frames of cardiac data set acquired using a 3.0T Siemens Skyra scanner (Table 1).

(a)

Scanner	3.0 T Siemens
No of receiver coils	30
Matrix Size	$512\ x\ 252$
FOV	$300mm^2$
TR	$2ms$
TE	$0.8ms$
Slice thickness	$8mm$
Flip angle	50^0

(b)

Features	CPU	GPU
Model	Core i7-4790	NVIDIATesla-K40c
Cores	4	2880
Clock Speed	3.60 GHz	745 MHz
Memory	16 GB	12GB
Memory	16 GB	12GB

Table 1 (a) Data acquisition details; (b) Hardware Specifications

Results: For a fair comparison, the execution time and reconstruction quality of the proposed method are compared with conventional GRAPPA (Figure 2). The proposed architecture substantially accelerates the computation time of GRAPPA by implementing it on GPUs, thereby providing a significant speedup (up to 37 $\times$ for R = 2 and kernel size = [11 $\times$ 4]) in our experiments. The proposed framework is scalable to different GRAPPA parameter settings (e.g. R and kernel sizes).

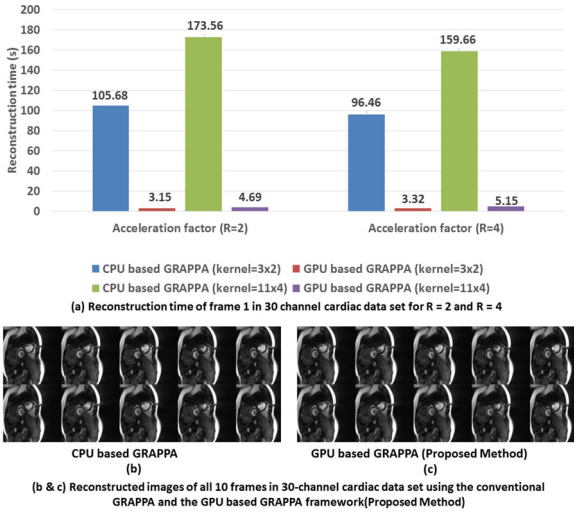

Figure 2: Quantitative and Qualitative comparison of the proposed GPU based GRAPPA with conventional GRAPPA

Discussion/Conclusion: The proposed GPU based parameterized GRAPPA is a suitable choice for efficient cardiac MR image reconstruction producing high-quality images with substantially reduced reconstruction time (a speedup up to 37× in our experiments) as compared to the conventional GRAPPA.

References:

[1] M. A. Griswold, et al. Magn Reson Med, 47(6):1202–1210, 2002.
[2] H. Wang, et al. Quantitative imaging in medicine and surgery, 8(2):196–208, 2018.
[3] Sharma, Girish, et al. Computers and Structures, 32(1):31–37, 2013.

P02.18

Bio-inspired surface coil for preclinical MRI at 15.2 T

S. Solis[1], F. Vazquez[1], R. Martin[1], J. Lazovic[2], O. Marrufo[3], L. Medina[1], **A. Rodriguez**[4]

[1]Universidad Nacional Autonoma de Mexico, Facultad de Ciencias, Departamento de Fisica, Mexico City, MEXICO, [2]Vienna Biocenter Core Facilities, Vienna, AUSTRIA, [3]National Institute of Neurology and Neurosurgery MVS, Department of Neuroimaging, Mexico City, MEXICO, [4]Universidad Autonoma Metropolitana Iztapalapa, Department of Electrical Engineering, Mexico City, MEXICO

Purpose/Introduction: Ultra high field magnetic resonance imaging (UHF MRI) holds many promises in terms of improved higher signal to noise ratio and consequent increase in space resolution or decrease in acquisition time. The sensitivity improvement and the RF coil optimization with respect to coil geometry and further design is one of the most important goals. We investigated biological patterns to use as potential new coil designs. We proposed a coil layout based on flower petal patterns for preclinical UHF MRI at 15.2 T.

Subjects and Methods: Numerical simulations of electromagnetic fields were done using the finite integration method and CST Microwave Studio (CST MICROWAVE STUDIO, CST GmbH, Darmstadt, Germany) at 650 MHz with open boundary conditions. A coil prototype was built following the pattern of a daisy flower (*Bellis perennis*). Circular-like petals were used to facilitate the construction and its analysis. Six circular petals (5 mm dimeter) were accommodated to form a closed loop (10 mm radius), see Fig. 1.

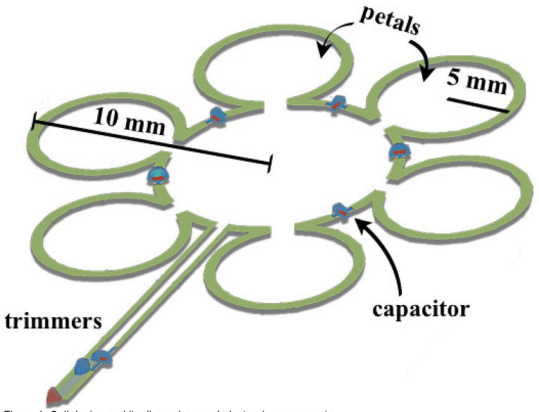

Figure 1. Coil design and its dimensions and electronic components

The coil prototype was constructed using copper sheets laminated onto a nonconductive board. Tuning and matching capacitors (0–15 pF: Voltronics Co. Salisbury, MD, USA) were soldered directly onto the surface. Additionally, five parallel ceramic capacitors (ATC, Huntington Station, NY, USA) were soldered as shown in Fig. 1. The coil design was operated in transceiver mode. Coil performance was measured via the quality factor (Q) as reported in [1]. We acquired phantom imaging experiments with a $CuSO_4 \times 2H_2O$ phantom in a 15.2T/11 cm preclinical imager (BioSpec, Bruker Co, Ettlingen, Germany) using a standard gradient echo sequence (FLASH sequence): TE/TR = 1.6/100 ms, NEX = 2, Flip Angle = 25^0, FOV = 18 × 18 mm^2, matrix size = 256 × 256, slice thickness = 1 mm, NEX = 4.

Results: Fig. 2 shows. (a) a bi-dimensional map of the SNR for the bio-inspired coil at 650 MHz. To demonstrate the feasibility of the coil prototype for application at UHF MRI, phantom image were acquired using standard pulse sequences (d). A SNR comparison plot was computed for the numerical and experimental results (c). Data was taken along the green line in (b). The quality factors were approximately: Q_u/Q_l = 21/13. These values compared very well with those values abundantly reported in the literature [2].

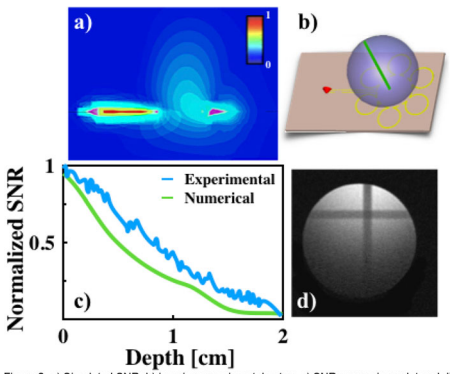

Figure 2. a) Simulated SNR, b) imaging experimental setup, c) SNR comparison plot and d) phantom image acquired at 15.2 T

Discussion/Conclusion: The SNR bi-dimensional map shows the usual pattern of a surface coil, where the higher intensity of the B_1 field is within the vicinity of the coil plane. A fairly good concordance can be appreciated in the SNR comparison plot, offering a reliable way to experimentally validate this coil design. This particular configuration offers the possibility to use a different number of petals and shapes to study the SNR and B_1 uniformity to offer an improved performance coil design.

References:

1. S. Solis-Najera, *et. al.* ISMRM-ESMRMB 2018, Abstract # 1746.
2. J.T. Vaughan, J.R. Griffiths. (Eds). RF Coils for MRI. John Wiley & Sons, 2012.

P02.19

Estimation of B_0 for traveling-wave MRI with a parallel-plate waveguide at 15.2 T

S. Solis[1], F. Vazquez[1], J. Lazovic[2], R. Martin[1], L. Medina[1], O. Marrufo[3], **A. Rodriguez**[4]

[1]Universidad Nacional Autonoma de Mexico, Facultad de Ciencias, Departamento de Fisica, Mexico City, MEXICO, [2]Vienna Biocenter Core Facilities, Vienna, AUSTRIA, [3]National Institute of Neurology and Neurosurgery MVS, Department of Neuroimaging, Mexico City, MEXICO, [4]Universidad Autonoma Metropolitana Iztapalapa, Department of Electrical Engineering, Mexico City, MEXICO

Purpose/Introduction: The transmission and reception of the RF signal at UHF MRI has mainly done using multi coil arrays. The approach poses a number of challenges because its development is associated with significant difficulties in design and construction of RF coil arrays [1]. An alternative to this it is the traveling-wave MRI (twMRI) approach. We have previously tested this approach using a parallel-waveguide (PPWG) with very encouraging results [2, 3]. However, the interaction of the PPWG with the magnet still remains to be investigated. We conducted some experiments to compute B_0 mapping using the PPWG and the bio-inspired surface coil to investigate this matter.

Subjects and Methods: We built a PPWG with 2 aluminium strips (1 cm width) and mounted on a plastic tube (1.2 m long and 2 cm diameter). Then, we filled the waveguide with a saline solution to conduct the RF signal. The bio-inspired surface coil reported in [3] was also used and operated in the transceiver mode and linearly driven. The RF coil was located outside the waveguide and perpendicular to the parallel plates. Fig. 1 shows the experimental setup and a coil diagram.

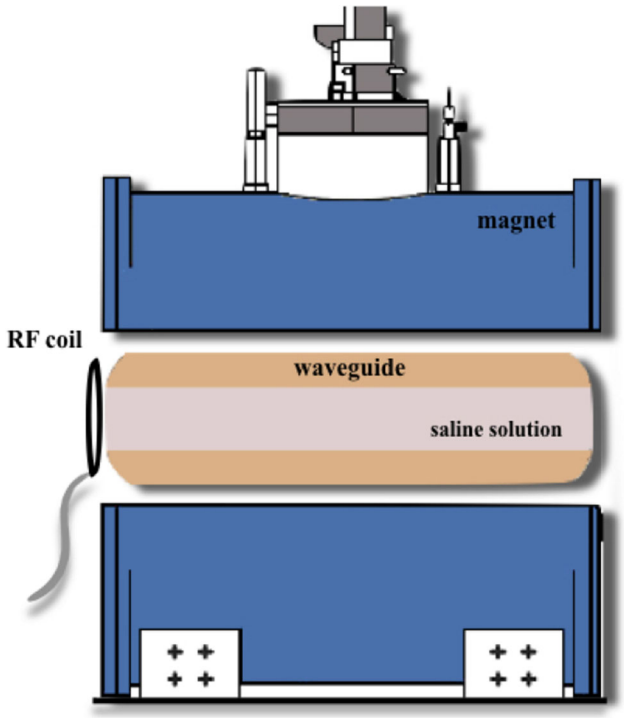

Figure 1. a) Bio-inspired surface coil and b) Imaging experimental setup.

We used a gradient echo sequence (FLASH) and the following acquisition parameters: TR/TE = 1000/3 ms, FA = 90°, FOV = 18 × 18 mm^2, matrix size = 128 × 128, thickness = 1 mm, NEX = 2. All experiments were run in a 15.2T/11 cm MR imager (BioSpec, Bruker Co, Ettlingen, Germany).

Results: Fig. 2c shows phantom images acquired with our RF coil and design and the saline solution-filled waveguide as shown in Fig. 1. These results show a very good image quality despite the fact that the coil was located 62 cm away. With the image data, a uniformity plot was also computed and shown in Fig. 2a. Additionally, B_0 map was calculated for this particular experimental setup and shown in Fig. 2d. Again, a uniformity plot was calculate as shown in Fig. 2b. The image SNR was computed and giving 23.85.

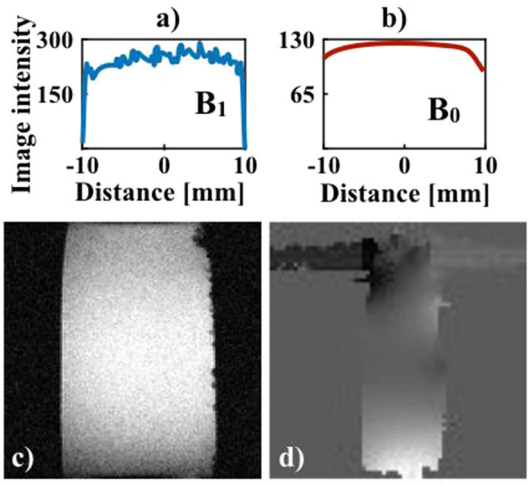

Figure 2. a) B1 uniformity and b) B0 uniformity, and c) phantom image and d) B0 mapping.

Discussion/Conclusion: Both uniformity profiles demonstrate that this particular waveguide is able to produce images with high uniformity and that there is no interaction affecting the image quality.

These experimental results show that remote excitation of the RF signal can be performed and producing high quality images. These results are in very good concordance reported in [2, 3]. This paper demonstrates that traveling wave MRI with high SNR can produce high quality images with a simple layout waveguide.

References:

1. N. I. Avdievich. UHF RF Array Coils for Body & Brain. ISMRM Workshop UF MR: Technological Advances, Translational Research Promises & Clinical Applications. 2019.
2. Vazquez, F., et. al., Travelling-wave transmitted with a simple waveguide for rodents Magnetic Resonance Imaging at 9.4 T. Ann. Meet. ESMRMB 2016:32:S31–S32.
3. Vazquez, F., et. al. Remote RF excitation for a small-bore MR imager at 15.2 T. ICEA IEEE APWC FEM. 2018:202–204.

P02.20

FPGA based Accelerated Pre-Scan Method for Sensitivity Estimation of Receiver Coils using High Level Synthesis

O. Inam[1], A. Akber[2], F. Naeem[2], **M. M. Ashraf**[1], M. Qureshi[1]

[1]COMSATS University Islamabad, Electrical & Computer Engineering, Islamabad, PAKISTAN, [2]COMSATS University Islamabad, Electrical and Computer Engineering, Islamabad, PAKISTAN

Purpose/Introduction: The reconstruction accuracy of SENSE (parallel MRI technique) [1] is a strong function of accurate estimation of receiver coils sensitivity map. In conventional SENSE reconstruction, pre-scan method [1] is widely used to estimate the sensitivity profiles of receiver coils. However, in case of multiple receiver coils, additive computational cost of pre-scan method increases the total reconstruction time of SENSE reconstruction algorithm. Recently, advanced reconfigurable devices known as Field-Programmable-Gate-Arrays (FPGAs) have been used to address the computational complexity of pMRI techniques [2]. This paper proposes a new FPGA based 32-bit floating point parameterized architecture for pre-scan method using advanced high level synthesis (HLS) tool known as Vivado Design suite.

Subjects and Methods: The proposed FPGA based architecture of pre-scan method is a scalable design which is capable of estimating the sensitivity profiles of arbitrary number of receiver coils using optimized modules i.e. Sum of Magnitude Module (SOMM) and Estimation Module (EM) where, SOMM computes Square root of Sum of Square (SSOS) by using pixel magnitudes of low-resolution images. The EM estimates the sensitivity maps using the SSOS and low resolution multichannel images as shown in Figure 1. The proposed architecture is optimized for low latency and high throughput using HLS directives such as pipelining and loop-unrolling.

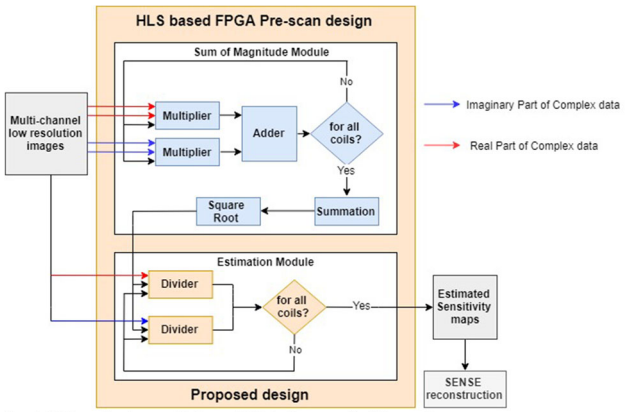

Figure1. HLS based hardware architecture on FPGA for Pre-scan method (Proposed)

The design is tested using eight-channel phantom dataset which is acquired using 1.5T scanner (data acquisition details are shown in Table 1). Dimension of low-resolution images used for this method is 64 × 64.

Scanner	1.5T (GE MR450)
Number of Receiver Coils	8
Matrix Size	256 x 256
FOV	300mm^2
TR	520ms
TE	15ms
slice thickness	5mm
Flip Angle	90 degree

Table 1. Data acquisition details

Results: The performance of the proposed FPGA based pre-scan method for SENSE is compared with its serial counter on CPU. The computation time (t), estimated sensitivity profiles and SENSE reconstructed image are evaluated for acceleration factor R= 2 as shown in Figure 2. The result shows that proposed method significantly speeds up the computation time by 8x as compared to CPU based method, without compromising the reconstruction accuracy of the SENSE reconstruction algorithm.

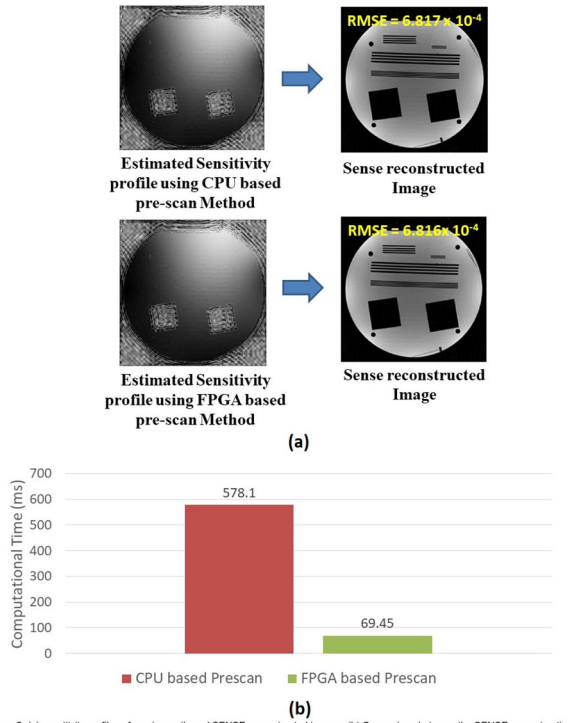

Figure 2. (a) sensitivity profiles of receiver coils and SENSE reconstructed images; (b) Comparison between the SENSE reconstruction time between the proposed method and CPU based Pre-scan method

Discussion/Conclusion: A new parameterized FPGA based architecture of pre-scan method is proposed to accelerate the sensitivity map estimation for SENSE reconstruction. This architecture is optimized by using HLS framework to achieve low latency and high throughput without degrading the quality of reconstructed images.

References:

[1] Pruessmann K P, Weiger M, ScheideggerMB and Boesiger P "SENSE: sensitivity encoding for fastMRI" *Magn. Reson. Med.* 42 952–62 1999.

[2] Siddiqui, MF, Reza, AW, Shafique, A, Omer, H, Kanesan, J. FPGA implementation of real-time SENSE reconstruction using prescan and Emaps sensitivities. *Magn Reson Imaging* 2017; 44: 82– 91

P02.21

Magnetic Resonance Image Compilation (MAGiC): Applications beyond brain

R. Vadapalli[1], R. d. Mulukutla[2], a. s. Vadapalli[3], R. b. Annamraju[4]

[1]Vijaya Diagnostics, Radiology, Hyderabad, INDIA, [2]Udai Omni Hospitals, Spine surgery, Hyderabad, INDIA, [3]Medway Maritime Hospital Windmill Road Gillingham Kent, Orthopaedic surgery, Hyderabad 500020, INDIA, [4]GE Healthcare, Digital innovations in affordable care, Bangalore, INDIA

Purpose/Introduction: To elucidate the emerging clinical applications of MAGC(Magnetic Resonance Image Compilation) beyond brain in MSK, spine.

Synthetic MR imaging enables reconstruction of various image contrasts from 1 scan, reducing scan times and potentially providing novel information with multiple contrasts.

Subjects and Methods: 67 subjects in the age groups of 28–64 years with M:F ratio of 3;2 who were referred for MR examinations for cervical and lumbar radiculopathy (n = 32),Knee Pain (n = 9),Hip pain (n = 8),Shoulder injury (n = 5),ankle and foot pain (n = 6) Wrist and hand (n = 7).The Conventional MR Imaging protocols were supplemented with MaGIC sequence with 6 image contrasts. T1, T2, PD, STIR, DIR, PSIR with quantitative T1 and T2 R1.R2 maps in 4 min. This study was done with informed consent of the patient and ERB approval.

The images were randomized and independently assessed for diagnostic quality, morphologic legibility, diagnostic radiologic findings indicative of disc herniations, spinal stenosis, sacro ilitis, Ligament injury, chondromalacia, sjubchondral erosions, Tenosynovitis, joint effusion, tendnoses, tendon and meniscal tears were analyzed on MAGIC 6 contrast views and compared to the conventional MR imaging.

The MAGIC T2 quantitative maps of knee and hip with ROIs on cartilage were compared with conventional Multi echo T2 relaxometry cartigram maps

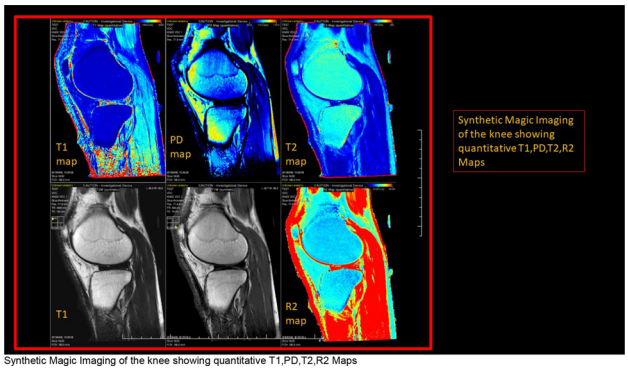

Synthetic Magic Imaging of the knee showing quantitative T1,PD,T2,R2 Maps

Results:

Overall diagnostic quality of synthetic MR images was noninferior to conventional MR imaging for epilepsy on a 5-level Likert scale ($P < .001$; mean synthetic-conventional, -0.344 ± 0.312; $\Delta = 0.5$; lower limit of the 95% CI -0.398). Legibility of synthetic and conventional morphology agreed in $> 95\%$, except in the ankle and shoulder T1, T2 STIR (all $> 60\%$). Synthetic T2 STIR had more obvious artifacts. T2 synthetic maps contributed to measurement of T2 relaxation times of Knee and hip cartilage which showed concordance with Conventional Multi echo T2 relaxometry sequences. Morphological findings like joint effusion, erosions, chondromalacia, ligament and tendon injuries, meniscal and labral tears and spinal stenosis and disc herniations, sacro ilitis showed acceptable concordance.

STIR, DIR vews of Magic contributed maximum for detections of sacro ilitis, tenosymovitis chondromaacia and so as quantitative T2 maps of MAGIC. Inter observer variability was in acceptable limits (Cohen's kappa 0.9).

Sensitivity and Specificity and AUC of conventional and Synthetic Magic sequences are 98%, 89% and 98% and 82% respectively

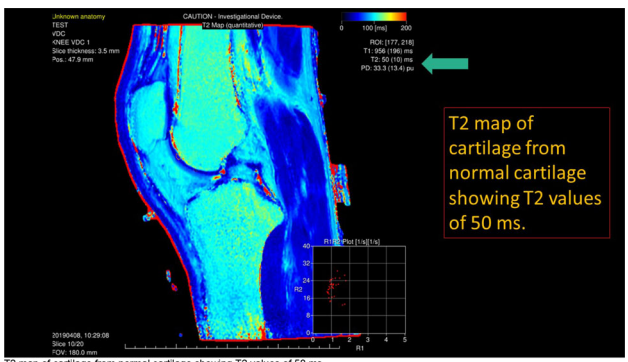

T2 map of cartilage from normal cartilage showing T2 values of 50 ms

Discussion/Conclusion:

Overall synthetic MR imaging quality was similar to that of conventional spine, joint imaging with the facility of additional contrast views : STIR, PSIR and DIR quantitative T1 T2, R1; R2 maps thus increasing the sensitivity and specificity.

References:

Tanenbaum LN, et. al. Synthetic MRI for clinical neuroimaging. AJNR Am J Neuroradiol 2017; 1103–10.

P02.22

Feasibility of single voxel CEST measurements with a transceiver surface coil

D. Kleimaier, L. R. Schad

Heidelberg University, Computer Assisted Clinical Medicine, Mannheim, GERMANY

Purpose/Introduction: Chemical exchange saturation transfer (CEST) is a powerful method to study proteins and biomolecules with an imaging resolution comparable to conventional MRI[1,2]. Exchangeable protons are selectively saturated by a saturation pulse and the reduced water signal is acquired. The saturation pulse requires a volume coil to achieve a homogenous B_1^+ distribution across the imaging object[3]. To achieve a high SNR, the volume coil must be combined with a receiver surface array which might not be available for every imaging object. Thus, a transceiver surface coil, resulting in an inhomogeneous B_1^+ distribution, might be preferred due to the higher SNR compared to a transceiver volume coil.

In this study, we investigated the feasibility of single voxel CEST measurements with a transceiver surface coil by acquisition of Z-spectrum for various B_1^+ strengths. Volume coil CEST measurements served as a gold standard.

Subjects and Methods: Data was acquired on a 9.4T preclinical MRI (Bruker, Germany) with two different coils:

1. Quadrature ^{1}H volume coil combined with a rat receiver surface array.
2. ^{1}H/^{19}F transceiver surface coil.

A voxel localized continuous wave CEST sequence with PRESS readout was used (Fig. 1). B_1^+ and T_1 were measured with a double angle method and inversion recovery sequence. The B_1^+ map was used for the optimization of the flip angle within the voxel. The Z-spectrum was analyzed by calculating the AREX metric[4]. To determine the reference Z-spectrum for the AREX metric, the Z-spectrum was inversely fitted by[2] (Fig. 1):

$$Z_{ss} = (\cos^2(\theta) * R_1)/(R_{eff} + R_{ex,ssMT} + R_{ex})$$

Where R_{eff}: water saturation[2]; $R_{ex,ssMT}$: gaussian lineshape[5]; R_{ex}: solute pool (k_b-term + R_{2b}-term + cross-term)[2].

Both coils were compared by varying the B_1^+ amplitude in the range of [0.1 7] µT and calculation of the NH_4Cl AREX amplitude by using two phantoms:

1. 10 mM NH_4Cl in 0.9% NaCl
2. 19.3 mM NH_4Cl in PBS with 2% agar.

a)

Sequence	Sequence parameters
CEST-PRESS	$T_R = 11.2$ s, $T_E = 16$ ms, 3x3x3 mm^3 voxel, 8192 points, $\Delta\tau = 62.4$ µs, 91/97 non-equidistant offsets, 10 s block pulse, [0.1 7.0] µT B_1^+ strength
Inversion Recovery	$T_R = 16$ s, 4096 points, $\Delta\tau = 124.9$ µs, 40 inversion times
B_1^+ map (EPI)	$T_R = 16$ s, 60° and 120° excitation angle, $T_E = 9.3$ ms, 25x25 mm^2 FoV, 100x100 matrix, 3 mm slice thickness

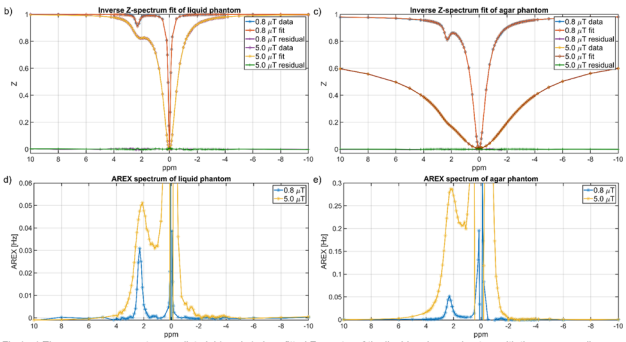

Fig.1: a) The sequence parameters are listed. b) and c) show fitted Z-spectra of the liquid and agar phantom with the corresponding AREX spectra shown in d) and e).

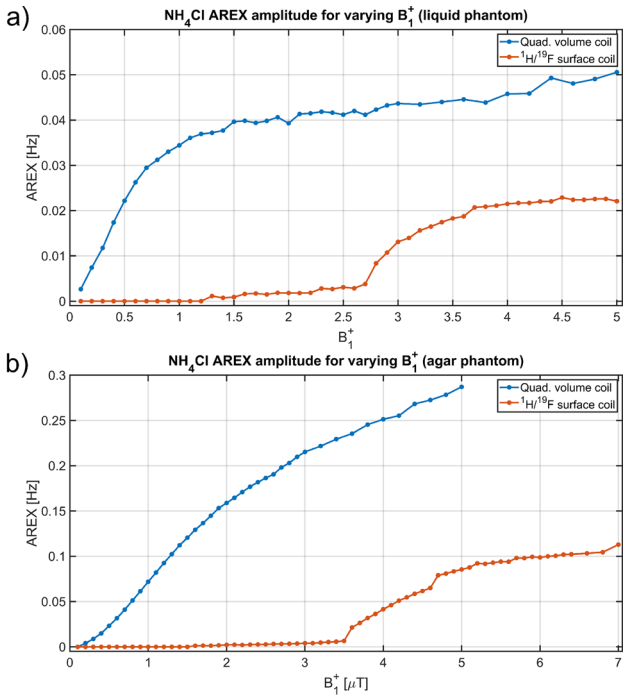

Fig.2: Comparison of the AREX amplitude of both coils for varying B1+ strength shown for the a) liquid as well as the b) agar phantom. The AREX amplitude was substantially lower and shifted when the transceiver surface coil was used.

Results:

The NH_4Cl AREX amplitude in both phantoms was substantially lower when the transceiver surface coil was used compared to the volume coil (Fig. 2). In addition, a shift towards higher B_1^+ strengths could be observed for the surface coil measurements (Fig. 2) even though the flip angle was optimized to yield the desired flip angle within the voxel. This becomes also evident when the Z-spectrum of both coils are compared (Fig. 3).

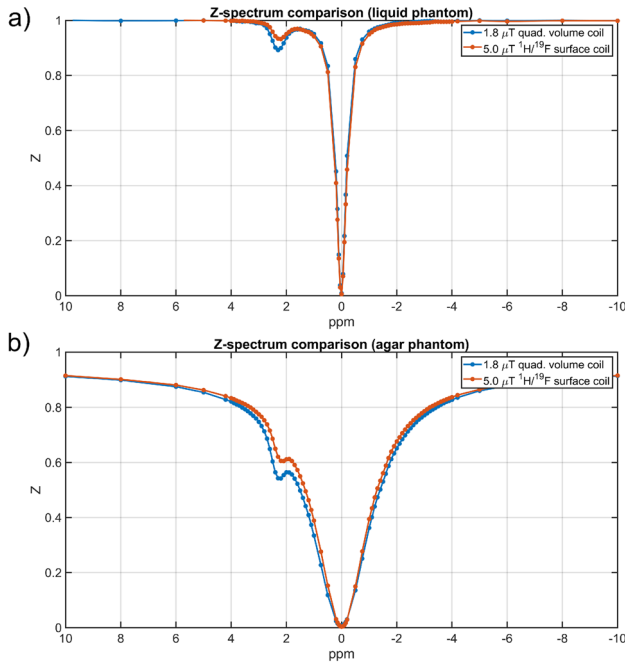

Fig.3: The Z-spectra of the a) liquid and b) agar phantom had a similar water saturation and semi-solid magnetization transfer, however the NH4Cl signal was lower for the transceiver surface coil measurements compared to the volume coil measurements.

Discussion/Conclusion: The inhomogeneous B_1^+ distribution of a transceiver surface coil resulted in a substantially lower and shifted NH_4Cl AREX amplitude compared to the volume coil.
In conclusion, our results showed that a transceiver surface coil is not suitable for single voxel CEST measurements due to a substantially lower and shifted solute AREX amplitude. Therefore, only volume coils in combination with a receiver array should be used to achieve the highest possible CEST signal.

References:

[1]Zhou NatMed 2003.
[2]Zaiss PhysMedBiol 2013.
[3]Windschuh NMRBiomed 2015.
[4]Zaiss NMRBiomed 2014.
[5]Desmond MRM 2011.

P02.23

Can bolus injection duration explain the difference in CBF estimates from DSC- and CT-perfusion?

J. Arvidsson, O. Jalnefjord, K. Lagerstrand, G. Starck

Sahlgrenska University Hospital, Department of Medical Physics and Biomedical Engineering, Gothenburg, SWEDEN

Purpose/Introduction: Measures of perfusion using bolus tracking techniques have been shown to be sensitive to the bolus administration scheme [1, 2]. A previous study where subjects underwent CT- and DSC-perfusion measurements under carefully matched conditions showed that DSC-MRI tended to produce higher estimates of CBF than CT, especially for high values of CBF [3].
One of the methodological differences between CT- and DSC-perfusion is the duration of the contrast-agent injection. In this work, we hypothesize that this difference in the contrast agent administration is a key source of discrepancy between CBF estimates when comparing CT- and DSC-perfusion. To test the hypothesis, signal time curves simulated using injection schemes typical of clinical CT- and DSC-perfusion protocols were analyzed to obtain estimates of CBF from each technique.

Subjects and Methods: Simulated signal time curves were generated based on the parameters in Table 1. Arterial input functions (AIF's) were simulated by convolving a box function (bolus injection) with a gamma variate function (bolus dispersion of the lungs and heart). The box function length was set according to typical clinical bolus administration protocols for DSC- and CT-perfusion. Tissue concentration time curves were simulated by convolving the AIF with the tissue response functions representing different levels of perfusion. The tissue residue response functions were generated according to $CBF \cdot R_{tissue}(t) = CBF \cdot (1 - \int_0^t h(\tau)d\tau)$, where h(t), is a gamma variate distribution of transit times, described by α and β and where $\beta = MTT/(\alpha + 1)$.
Gaussian distributed noise was added in the signal domains and curves where scaled to achieve an SNR of 12 at a CBF of 50 ml/100 g/min. Estimates of CBF were obtained by the use of a model based, Bayesian expectation maximizing deconvolution scheme [4].

Results: Noisy signal and concentration time curves where simulated with contrast agent injection durations typical of DSC- and CT-perfusion, one example is shown in Figure 1. CBF estimates where produced and presented in a scatter plot (Figure 2), which in particular illustrates a more pronounced underestimation of CBF for higher values for CT-perfusion when compared to of DSC-perfusion.

Discussion/Conclusion: This simulation study shows that differences between higher levels of CBF from DSC- and CT-perfusion found in previous experimental studies can be attributed, at least in part, to the longer bolus injection duration typical of CT-perfusion techniques.

Injection duration CT [s]	Injection duration MR [s]	small circulation dispersion parameters A and B	tissue transit time distr. parameter α	CBF [ml/100g/min]	CBV [ml/100g]	SNR (at CBF=50 ml/100g/min)
13	3	3 and 2	3	[10 30 50 70]	4	12

Table 1. Parameters describing the AIFs, tissue response function, and the SNR used for simulations

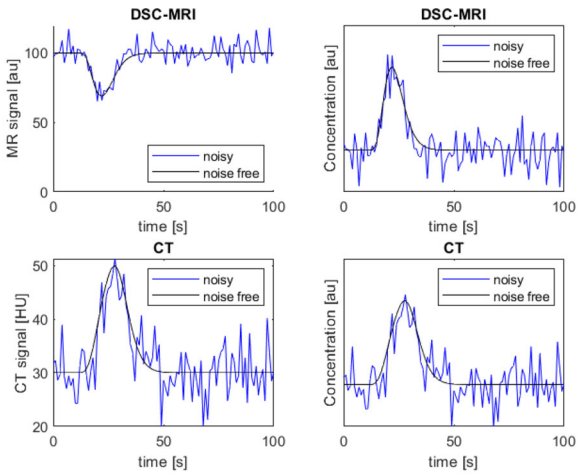

Figure 1. Simulated signal and concentration time curve (CBF 50 ml/100g/min) with and without noise for CT and DSC-MRI. The subplots show MR signal (top-left) MR concentration (top-right), CT signal (bottom-left) and CT concentration (bottom-right).

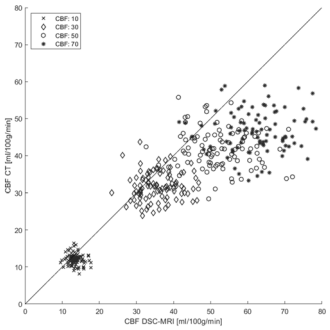

Figure 2. CBF estimates from DSC-MRI and CT-perfusion, performed for 100 noise instances for each simulated level of CBF (10,30,50,70 ml/100g/min)

References:

1. Wirestam 2010 Eur. J. Radiol.
2. van Osch 2003 MRM.
3. Ziegelitz 2009 MRM.
4. Mouridsen 2014 J. Cereb. Blood Flow Metab.

Clinical Review Posters

C01.01

The effect of automatic normative quantification of brain tissue volume on confidence in MRI based diagnosis of dementia: a pilot study

R. Steketee[1], K. de Visser[1], J. Papma[2], W. Niessen[3], M. Smits[1], M. Vernooij[4]

[1]*Erasmus University Medical Center, Radiology and Nuclear Medicine, Rotterdam, NETHERLANDS,* [2]*Erasmus University Medical Center, Neurology, Rotterdam, NETHERLANDS,* [3]*Erasmus University Medical Center, Biomedical Imaging Group Rotterdam—Departments of Medical Informatics and Radiology and Nuclear Medicine, Rotterdam, NETHERLANDS,* [4]*Erasmus University Medical Center, Radiology and Nuclear Medicine and Epidemiology, Rotterdam, NETHERLANDS*

Introduction: Brain magnetic resonance imaging (MRI) may support dementia diagnosis, but detecting early abnormalities visually and distinguishing these from normal aging remains difficult. Quantitative normative assessment of MRI may be more sensitive to abnormalities and enables comparison of individual patients' brain volumes to reference data from a healthy aging population.[1] We aimed to investigate whether such normative quantification changed confidence of neuroradiologists in dementia diagnosis, compared to routine visual assessment. Four neuroradiologists performed routine visual assessment (VA) of MRI scans of 30 memory clinic patients as well as quantitative assessment (QA) using Quantib™ ND (Fig. 1). They rated diagnostic confidence for both VA and QA, and change in confidence in VA after QA.

Screenshot of Quantib™ Neurodegenerative (ND), which automatically segments and quantifies brain structures from T1w-scans and plots these against age and sex specific reference curves derived from the population-based Rotterdam Study (ref. 2,3)

Cases: With VA, scans were rated normal in 10/30 (33.3%) and abnormal in 20/30 (66.7%) cases vs. 11/30 (36.7%) and 19/30 (63.3%) respectively with QA. There were 7 discrepancies (3 cases rated normal with VA and abnormal with QA, and 4 cases vice versa). Confidence in data being (ab) normal was similarly high for VA and QA (Fig. 2A).

Alzheimer's disease (AD) was more often diagnosed with VA than QA (5 vs. 3 cases), while frontotemporal lobar degeneration (FTLD) was more often diagnosed with QA than VA (6 vs. 4 cases, Fig. 2B). Both vascular dementia (VaD, 1 case) and mixed or multiple pathologies (4 cases) were diagnosed equally often with VA and QA. Diagnoses different than AD, FTLD, or VaD were slightly more often based on VA than QA (6 vs. 5 cases).

Confidence in diagnosis (Fig. 2C) tended to be slightly higher with VA than QA. Diagnostic confidence in VA after taking QA into account remained the same in 46.7% of cases, but decreased in 30% and increased in 23.3%.

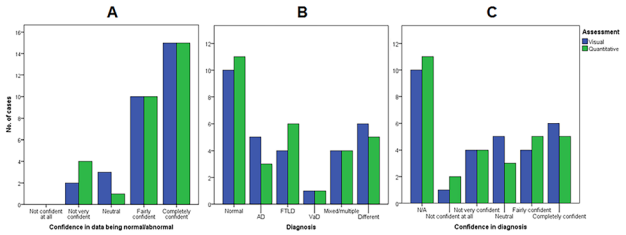

Histograms for visual (blue) and quantitative (green) assessment. A) confidence in data being (ab)normal; B) Diagnosis (AD: Alzheimer's disease, FTLD: frontotemporal lobar degeneration, VaD: vascular dementia); and C) confidence in diagnosis.

Representative cases are shown in Fig. 3. In Case 1, VA reflected QA, both leading to the diagnosis AD, with more confidence after taking QA into account. Multidisciplinary diagnostic analysis confirmed AD. In Case 2, the radiologist was fairly confident of the diagnosis AD based on VA, but confidence decreased after QA was rated normal. The multidisciplinary diagnosis was AD. For Case 3, the radiologist was fairly confident that VA was normal, but also fairly confident that QA was abnormal because of symmetric isolated frontal volume loss. This decreased confidence based on VA. The multidisciplinary conclusion was subjective memory complaints.

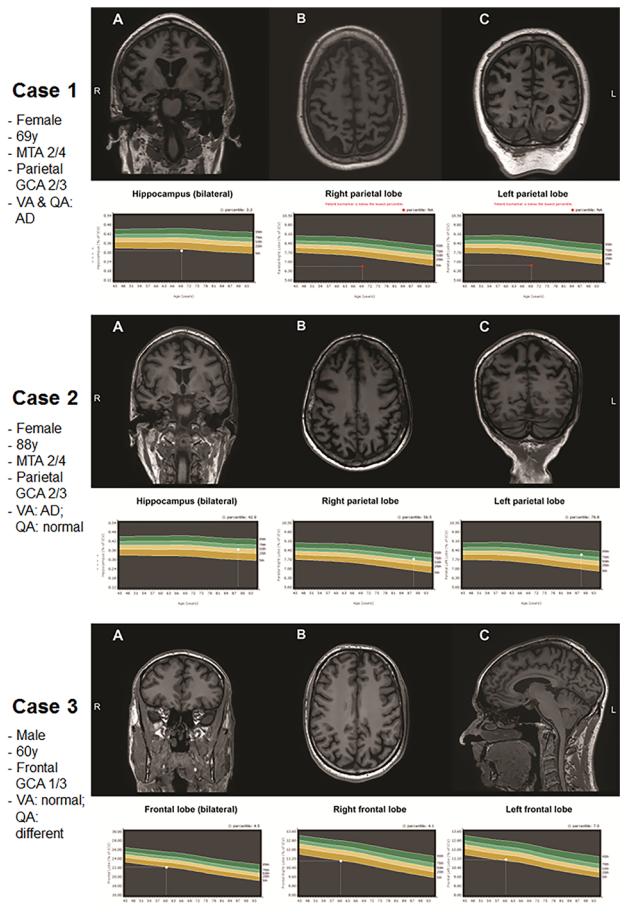

Visual and quantitative data of quantitative assessment (QA) supporting visual assessment (VA, Case 1), and of discrepancies between VA and QA (Case 2 and 3). MTA: medial temporal lobe atrophy; GCA: global cortical atrophy. AD: Alzheimer's disease

Discussion: We showed in a small sample of memory clinic patients that normative quantification of brain tissue volume may aid neuroradiological diagnosis of dementia. Collection of confidence ratings is ongoing to determine in a larger sample the actual effect of quantitative assessment on confidence in MRI based diagnosis of dementia.

References:
1 Vernooij et al. Neuroimage Clin 2018;20:374–379.
2 Hofman et al. Eur J Epidemiol 2015;30:661–708.
3 Ikram et al. Eur J Epidemiol 2015;30:1299–1315.

C01.02
WITHDRAWN

C01.03
Analysis of RF Induced Heating of Orthopedic Implant Embedded in Bone Material

Z. Ihsan[1], G. Schaefers[2]

[1]*MR:comp GmbH, Gelsenkirchen, GERMANY,* [2]*MRI-STaR-Magnetic Resonance Institute for Safety,Technology and Research GmbH, Gelsenkirchen, GERMANY*

Introduction: A test object immersed in the gel simulating the tissue of the human body is used as the standard test procedure of radio frequency (RF) induced heating for passive implants [1]. However, especially orthopedic implants, e.g. hip prosthesis are fully embedded in the bone of the human body where relative electric permittivity of the bone (cancellous) material is smaller than relative electric permittivity of the gel used in the experiment. The impact on RF induced heating of passive implants surrounded by bone has been discussed in [3–5]. Here we propose a workflow to select the worst-case of multi-configuration orthopedic implants embedded in the bone material.

Cases: The wavelength in the medium λ_m depends on the relative permittivity of the medium ε_r expressed as $\lambda_m = \lambda_0/\varepsilon_r$, where λ_0 represents the vacuum wavelength. This fundamental principle indicates that the resonant length of the orthopedic implant in the bone material would be larger than in the gel. Two simulation setups with the ASTM phantom inside a birdcage RF coil at 64 MHz were performed. First the phantom was completely filled with gel, and in the second setup a bone construct surrounding the implant in the gel was used as illustrated in Fig. 1. Electromagnetic (EM) simulation of a titanium (Ti) rod with a varying length of 5 cm to 29 cm inside these phantoms was applied by employing a time-domain (TD) solver (CST *studio suite* 2019, Darmstadt, Germany) in order to assess the worst-case length of both scenarios. Additionally, thermal simulation for an exposure of up to 15 min was performed in order to verify the worst-case length.

Discussion: The normalized SAR peak values over the length of the Ti rod are shown in Fig. 2. The worst-case length of the Ti rod immersed in the gel was found at *the critical length* of 19 cm. It can be seen that the Ti rod embedded in the bone material leads to a different worst-case at length of 25 cm. The thermal simulation shows an agreement as shown in Fig. 3 where the temperature at the hot spot rises by increasing the rod length in the bone material and decreases in the gel material. The higher temperature found in the bone material is mainly influenced by the higher thermal resistance of the bone material.

The full-wave simulation confirms that the length of the worst-case implant embedded in the bone material could be longer than immersed in the gel. This strategy is proposed in case the length of the implant covered in the product matrix exceeds the critical length.

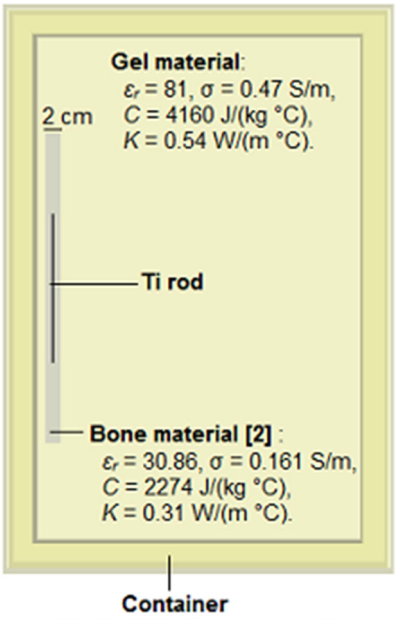

Fig. 1 : ASTM F2182-11a phantom with the bone construct.

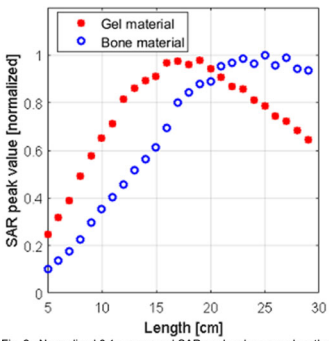

Fig. 2 : Normalized 0.1 g averaged SAR peak values over length of the Ti rod in the gel and in the bone construct at 64 MHz.

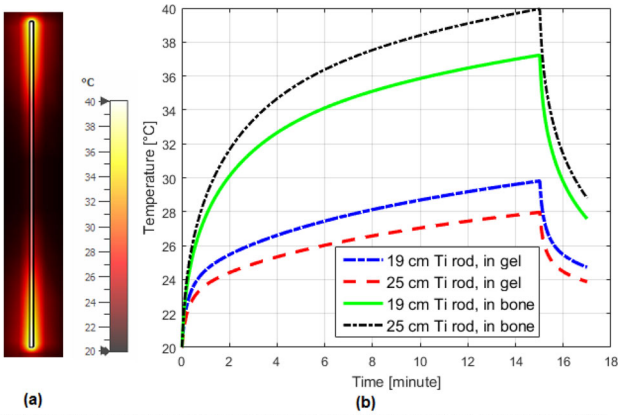

Fig. 3 : (a) Temperature distribution of the 25 cm Ti-rod in the bone construct at 15 minutes of exposure, (b) Temperature rise at the maximum hot spot in the gel and in the bone construct.

References:
[1] ASTM F2182-11a (2011).
[2] ISO/TS 10974:2018.

[3] J.A. Nyenhuis, C.R. Miller, "Calculation of Heating of Passive Implants by the RF Electromagnetic Field in MRI", 30th URSI Symposium, 2011.
[4] M. Kozlov, G. Schaefers, WEP-UA.3P.2, AP-S/URSI, 2016.
[5] M.Murbach, E. Zastrow, E. Neufeld, T. Samaras, W. Kainz & N. Kuster, #0647 26th ISMRM Proceedings, 2018.

C01.04
WITHDRAWN

C01.05
Identification of the somatosensory system using diffusion tensor tractography

W. Lee[1], S. Hartono[2], Y. L. Lo[2], L. L. Chan[1]

[1]*Singapore General Hospital, Department of Diagnostic Radiology, Singapore General Hospital, Singapore, Singapore, SINGAPORE,* [2]*Singapore General Hospital, Department of Neurology, National Neuroscience Institute, Singapore General Hospital Campus, Singapore, Singapore, SINGAPORE*

Introduction: The medial lemniscus (ML) and spinothalamic tracts (STT) are the two main somatosensory tracts. ML pathway is the neural tract for proprioception and tactile sensations, whilst STT is the neural tract responsible for pain and temperature. Diffusion tensor tractography (DTT) is extensively used pre-operatively for in vivo mapping and visualisation of neural tracts. There is however, scanty DTT literature on somatosensory tracts compared to the other neural tracts. Although the effects of injury to somatosensory tracts is less crippling than, for example, speech impairments due to accurate fasciculus tract disruption, it is no less important. Conditions such as multiple sclerosis can impair somatosensory functions, resulting in delayed pain and temperature sensations. Additionally, somatosensory injury has been demonstrated to impact physical activity, resulting in prolonged hospital stay.
Delineating the somatosensory tracts is challenging due to the complex brainstem nuclear anatomy and varying DTT methodology[1,2]. Understanding the complex brainstem anatomy lends greater accuracy to DTT region of interest (ROI) placement, adding value to predictive clinical outcomes of operative efforts. The objective of this poster is to demonstrate the clinical feasibility of reconstructing ML, STT and their thalamocortical pathways, as well as the technical difficulties encountered.
Cases: Both ML and STT ascends from the medulla (STT dorsolateral to ML), through the pontine tegmentum, lateral to mesencephalic decussation to terminate at the thalamus. The thalamocortical pathways then continue as third-order neurons to the somatosensory cortex (Fig. 1).

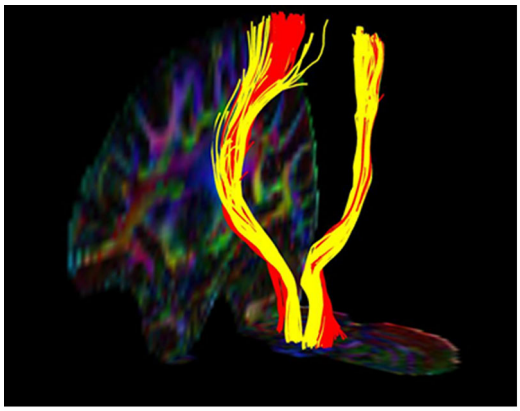

Figure 1. Tractography of ML and STT and corresponding thalamocortical pathways

Two axial ROIs were applied for both ML and STT. The first ROI was placed at the most inferior axial section containing the red nucleus (RN) (Fig. 2), and the second at level of mid-pons (Fig. 3), in the pontine tegmentum. STT ROIs were placed more dorsolaterally than those for ML.

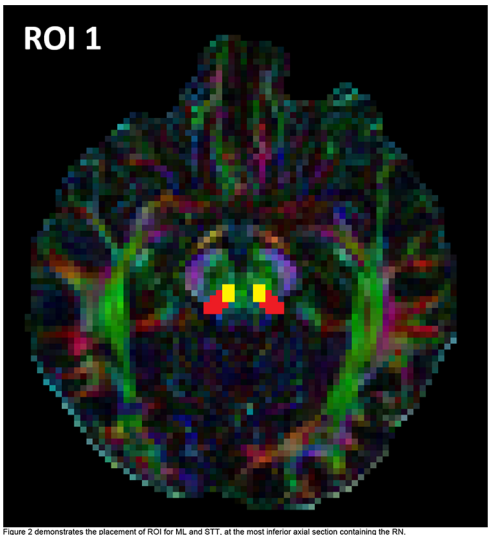

Figure 2 demonstrates the placement of ROI for ML and STT, at the most inferior axial section containing the RN.

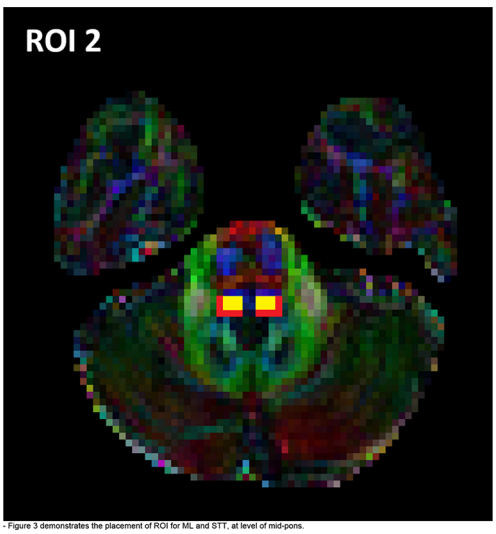

- Figure 3 demonstrates the placement of ROI for ML and STT, at level of mid-pons.

Discussion: Demonstration of the origin and termination of somatosensory tracts and their thalamocortical pathways aids in preoperative evaluation of risks and rehabilitative strategies. ML and STT terminates at the thalamus, and thus have more limited anatomical targets for ROIs placement for DTT. More work to improve tractography methods for these neural tracts is much needed. These could further forward our understanding of brain plasticity following cortical injury.

References:

1. Kamali, Arash, et al. "Diffusion tensor tractography of the somatosensory system in the human brainstem: initial findings using high isotropic spatial resolution at 3.0 T."

2. Yoshida, Shoko, et al. "Quantitative diffusion tensor tractography of the motor and sensory tract in children with cerebral palsy."

C01.06

Improving the Accuracy and Reliability of Callosal Angle Measurement in the Diagnosis of Normal Pressure Hydrocephalus

W. Lee[1], A. Lee[1], R. Chen[1], N. Keong[2], L. L. Chan[1]

[1]*Singapore General Hospital, Department of Diagnostic Radiology, Singapore General Hospital, Singapore, Singapore, SINGAPORE,* [2]*Singapore General Hospital, Department of Neurosurgery, National Neuroscience Institute, Singapore, Singapore, SINGAPORE*

Introduction: Normal pressure hydrocephalus (NPH) can resemble neurodegenerative diseases such as Alzheimer's Disease (AD), with clinical symptoms similarity of 75%[1], making diagnosis challenging. An accurate diagnosis is crucial as NPH is the only surgically reversible gait disorder. However, there is variability in treatment management due to difficulty in diagnosis and therefore establishes the need for a clear imaging maker[1]. Corpus callosal angle (CA) presents as a viable diagnostic tool and was reported to have an accuracy of 93%, sensitivity of 97% and specificity of 88% in differentiating NPH from AD, using a recommended CA cut-off of 90°[2].

Cases: CA is measured on the coronal plane, drawing lines tangential to the lateral ventricular roof, and is given by the degree of intersection of both lines. While CA measurement is straight forward, a non-standardized workflow or setup for measurement can result in variable readings and impact the clinical utility. Therefore, consistent and reproducible measurements are important and require a two-step approach. Firstly, care should be taken to ensure that the chosen coronal slice at the posterior commissure is oriented perpendicular to the antero-posterior commissure plane (AC-PC). Secondly, ensure that the coronal plane created is perpendicular to the mid-sagittal line (Fig 2b).

In the following figures, coronal slices were deliberately reconstructed with different angulations (± X and ± 2X) to the AC-PC, to demonstrate how anterior-posterior and right-left rotations of the coronal planes can result in variable CA measurements (Figs. 1, 2).

Figure 1

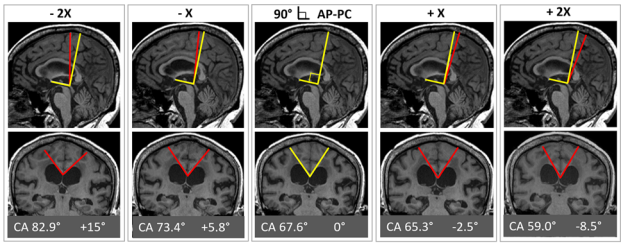

Figure 1. Variable CA values of subject A (pre-shunt), as a result of anterior/posterior offset angle of X and 2X. A larger angle offset generated greater variability in CA.

Figure 2

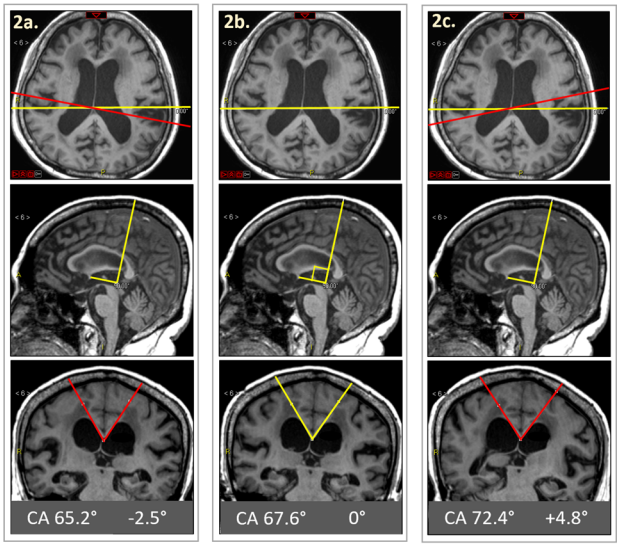

Figure 2. Variable CA values of subject A, with right/left rotation of angle X. 2b demonstrates the ideal plane set up; Perpendicular to both AC-PC and mid-sagittal planes, at level of PC.

Discussion: CA measurements is a useful non-invasive clinical imaging marker, and when done accurately can ensure timely diagnosis and treatments. Measurements can easily be performed, albeit at risk of misreporting secondary to coronal plane malrotation. Therefore, it is imperative to ensure optimal plane setup for accurate and reproducible measurements.

References:

1. Di Ieva, Antonio, Mikaeel Valli, and Michael D. Cusimano. "Distinguishing Alzheimer's disease from normal pressure hydrocephalus: a search for MRI biomarkers." *Journal of Alzheimer's Disease* 38.2 (2014): 331-350.

2. Ishii, Kazunari, et al. "Clinical impact of the callosal angle in the diagnosis of idiopathic normal pressure hydrocephalus." *European radiology* 18.11 (2008): 2678.

C01.07

WITHDRAWN

C01.08

Arterial spin labelling: Basics and current emerging clinical applications what every resident must know

R. Vadapalli[1], S. J. sattaluri[2], a. s. Vadapalli[3], R. b. Annamraju[4]

[1]Vijaya Diagnostics, Radiology, Hyderabad, INDIA, [2]KIMS, Neurology, Hyderabad, INDIA, [3]Medway Maritime Hospital Windmill Road Gillingham Kent, Orthopaedic surgery, Hyderabad 500020, INDIA, [4]GE Healthcare, Digital innovations in affordable care, Bangalore, INDIA

Introduction: Content organization:
-Various techniques of arterial spin labelling (ASL)are discussed with their pearls and pitfalls.
- Role of ASL on following Clinical applications is discussed, acute and chronic cerebrovascular disease, AV malformations Neoplasms Epilepsy, Neurodevelopmental disorders,Aging and neurodegenerative disorders. Paediatric cerebral blood flow studies with Perfusion based FMRI.
-Illustrative case examples are highlighted.

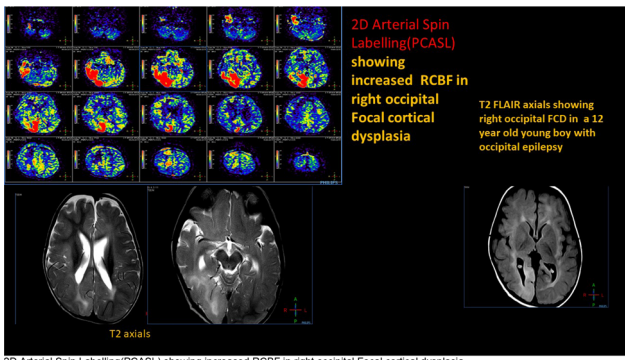

2D Arterial Spin Labelling(PCASL) showing increased RCBF in right occipital Focal cortical dysplasia

Cases:
Clinical applications case based review:
acute and chronic cerebrovascular disease,
AV malformations
Neoplasms
Epilepsy,
Neurodevelopmental disorders,
-Illustrative case examples are highlighted.

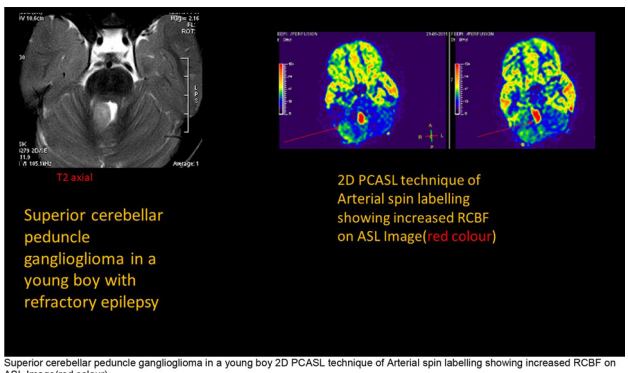

Superior cerebellar peduncle ganglioglioma in a young boy 2D PCASL technique of Arterial spin labelling showing increased RCBF on ASL Image(red colour)

Discussion:
Basic concepts of ASL :key points:
Arterial spin labelling (ASL) is a non-invasive, quantitative, repeatable MRI technique, which allows measuring the brain perfusion without contrast agent using arterial blood water as an endogenous tracer and eliminating the risk of nephrogenic systemic fibrosis in patients with renal dysfunction.
A radiofrequency pulse (RF) using to invert the water molecules- this is the labelling part of the ASL.
After a delay so-called post-labelling delay (PLD) or inversion times (TI) the labelled blood flows into the brain tissue and a labelled image is acquired which contain signal from the inverted- and static tissue protons. A control image is also necessary without labelling. The difference between the control and labelled images provide a measure of labelled blood from arteries delivered to the tissue by perfusion
Snapshot images are acquired in labelled and control conditions and subtracted
There are three major approaches for ASL: continuous (CASL) and pulsed (PASL) and Pseudo continuous ASL.
In CASL, arterial blood water is continuously and selectively labelled as it passes through a labelling plane, typically applied at the base of the brain. Labelling of all blood water occurs at the same location, and labelling can be applied for several seconds, maximizing the effects on brain signal. In PASL, a short RF pulse is used to instantaneously invert blood and tissue, and can be applied either below the brain, or to the entire brain with subsequent selective inversion of the imaging slices to produce a magnetization difference between blood and brain water.
ASL imaging sequences incorporating high field, parallel imaging, pseudo-CASL, and 3D imaging with background suppression now provides an approximately 10-fold increase in sensitivity for imaging CBF

References:

1. Wong EC. Quantifying CBF with pulsed ASL: technical and pulse sequence factors. J Magn Reson Imaging.;2005;22:727–731.
2. Wang J, Alsop DC, Song HK, et al. Arterial transit time imaging with flow encoding arterial spin tagging (FEAST) Magn Reson Med. 2003;50:599–607.

C01.09

WITHDRAWN

C01.10

WITHDRAWN

C01.11

Myelinisation in young children who stutter: a DTI-study of the speech and language network

H. Deman, F. Vandecruys, N. Baerts, S. Timmermans, S. Sunaert, M. Verly

KU Leuven, Department of Neurosciences, Leuven, BELGIUM

Introduction: Nowadays, fluent speech production seems to be an obvious ability. Developmental stuttering is a disorder that affects millions of children all over the world. Stuttering is unintentionally and can highly affect the quality of life. The etiology of developmental stuttering is still unclear. However, evidence is growing that there are subtle neurostructural differences in adults who stutter (AWS) and children who stutter (CWS).
We aim to investigate the structural connectivity underlying stuttering in young CWS and the relation to their language skills and stuttering severity. More specific, we evaluate the structural connectivity in four white matter tracts: the Superior Longitudinal Fascicle (SLF), the Inferior Fronto-Occipital Fascicle (IFOF), the Uncinate Fascicle (UF) and the Inferior Longitudinal Fascicle (ILF).
Cases: Method: Using DTI and manual tractography, white matter morphology was investigated in twelve CWS (ranging from 4 to

11 years of age) and twelve controls. Both macrostructural and microstructural parameters were used to characterize those tracts in both groups. Inclusion criteria required all children to exhibit developmental stuttering, no indication of known neurological or medical disorders, Dutch as their native language and a normal language and cognitive development. In addition, language performances was investigated as well as stuttering severity and IQ.

Results: Differences in structural neuroconnectivity between both groups were found. Additionally, the majority of the parameters of all investigated tracts exhibited a more pronounced right-sided lateralization in CWS, while control children displayed a more left-sided lateralization. A link between structural neuroconnectivity and language skills or stuttering severity was not found.

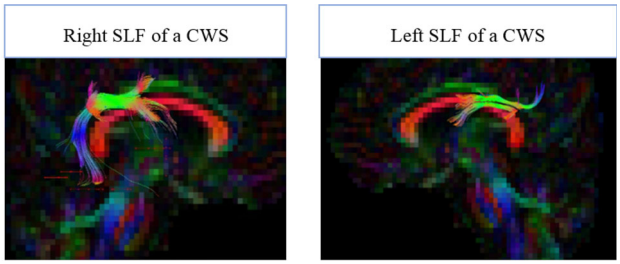

Example of the SLF in a CWS illustrated on ExploreDTI.

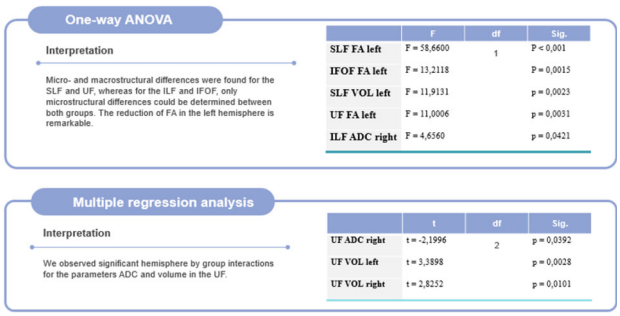

Comparison of the DTI parameters of CWS versus CNS: significant results.

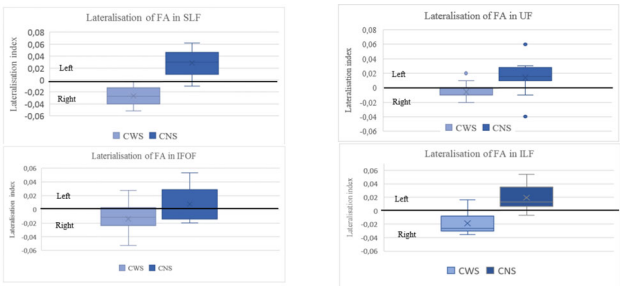

Difference in lateralisation of FA in the SLF, IFOF, UF and ILF.

Discussion: Our most remarkable finding is the atypical asymmetry in the language related white matter tracts of CWS. The results show that CWS develop a more pronounced right-sided lateralization in all investigated tracts, in contrast to the left-sided lateralization in typically developing children. Due to the abnormal development of the left hemisphere, an abnormal lateralization pattern might arise in CWS (Kell et al.). Our results show evidence for a compensatory role of the right hemisphere in CWS. Because all our participants were young children, our results can prove that the detected group differences constitute the cause for stuttering and do not reflect compensatory processes following years of stuttering.

References:

Geschwind, N., & Galaburda, A. M. (1985). Cerebral Laterialization. Biological Mechanisms, Associations, and Pathology. Archives of Neurology, 42, 428–654.

Kell, C. A., Neumann, K., von Kriegstein, K., Posenenske, C., von Gudenberg, A. W., Euler, H., & Giraud, A.-L. (2009). How the brain repairs stuttering. Brain, 132(10), 2747–2760.

C01.12

Management of intracranial aneurysms with 3D-SMS-TOF imaging and acetylsalicylic acid therapy: First completely regressed aneurysm in the literature

O. ALGIN

UMRAM, Bilkent University, Ankara, TURKEY

Introduction: In recently published articles, low-dose acetylsalicylic acid (ASA) administration has been reported to be beneficial for prevention of aneurysm rupture. This articles argued that ASA decreases inflammation which is a key mechanism in a formation and/or rupture of intracranial aneurysms. Based on data of a small number of patients of these studies, ASA treatment may decrease the inflammation or oxidative stress in the walls of aneurysms. However, such as our case or condition has not been reported in the literature.

In this paper, we present a patient with cerebellar infarcts and headache due to posterior system aneurysm. The patient's complaints and aneurysm were completely regressed with low-dose (100 mg) daily ASA therapy for 2 years. Our aim is to discuss the efficacy of daily low-dose ASA administration in the treatment of cerebral aneurysms referring to the literature.

Cases: 67 years old smoker female sent to our clinic from another center due to headache and multiple posterior system infarcts. On the back of the eye-level isotropic SMS-TOF MRA images, dissecting PICA aneurysm with wide neck was detected. An immediately obtained DSA examination showed an aneurysm with 8 mm diameter in the right PICA. The patient was given detailed information about the risks of surgery or endovascular intervention. The patient did not accept surgery or intervention. Therefore, the patient was started on low-dose daily ASA treatment. The patient was followed up at 6-month intervals. Two years later she applied to our hospital, the eye-level isotropic SMS-TOF MRA images showed that the aneurysm regressed completely and there is no any additional abnormality.

Discussion: Hasan et al. reported that daily low-dose ASA treatment is useful for prevention of intracranial aneurysm rupture, especially in patients with a small aneurysm or high operation & intervention risk. The mechanism of action of the ASA related that macrophages and COX-2/mPGES-1 related products are thought to be the leading part in the formation and rupture of cerebral aneurysms. ASA has been found to be safe in patients harboring cerebral aneurysms and low dose daily ASA treatment may be a promising agent for reducing vascular inflammation.

In conclusion, back of the eye-level isotropic SMS-TOF MRA can help in early diagnosis, management and follow-up of patients with an intracranial aneurysm. In patients with a small aneurysm or high risk for surgery/intervention; long-term treatment with daily low-dose ASA can be initiated, and surgery or intervention can be postponed. This approach may prevent unnecessary surgeries/interventions and decrease mortality/morbidity/costs. More importantly, it may be a more preferable treatment method due to its non-invasive nature. Comprehensive researches are needed for clarifications of these issues.

References:

References will be given later (off-line).

Software Exhibits

SE01.01
BreastIS: An Analysis Software for Breast Magnetic Resonance Imaging of Breast

B. Bayrambas[1], G. H. Hatay[1], K. Yegin[2], E. Ozturk-Isik[1]

[1]*Bogazici University/Biomedical Engineering Institute, Istanbul, TURKEY,* [2]*Ege University, Electrical and Electronics Engineering, Izmir, TURKEY*

Purpose of the Software: Magnetic resonance imaging of breast provides valuable information about breast tissue composition. A common breast MRI protocol may include dynamic contrast enhanced (DCE) MRI, diffusion weighted MRI (DWI) and proton MR spectroscopic imaging (1H-MRSI). There have been several software tools that can analyze each of these data types separately. In this study, we developed a flexible and open-source post-processing software called BreastIS to analyze DCE-MRI, DWI, and 1H-MRSI and store them in a database for further exploration.
Methods/Implementation: BreastIS image processing software was implemented using MATLAB and the graphical user interphase was developed using MATLAB GUI and Java. The software could be run on Windows, Mac and Linux computers.
The software supports DICOM format for analysis. It has basic features of a PACS system. It creates workspace for each patient, and stores patient and scanning information, DICOM images in.mat format, and analysis results in the corresponding directory of database for future access.
Main features of BreastIS software in terms of image processing and analysis are as follows.

(1) It provides a viewer for MR as shown in Figure 1. Region of interest (ROI) based analysis is provided.
(2) It allows image quality assessment, signal to noise ratio (SNR) calculation, and low-pass, high-pass and median filtering.
(3) For DCE-MRI analysis, kinetic curves are generated for user defined ROI with signal uptake patterns (0: no enhancement,1: persistent, 2:plateau, 3:washout) [1]. Signal uptake, percentage enhancement (PE) and time-to-peak (TTP) maps are created for dynamic series (Figure 2).
(4) For DWI analysis, an interface provides access to SPM [2] toolbox of MATLAB, which calculates fractional anisotropy (FA) and mean diffusivity (MD) maps.
(5) The interface for 1H-MRSI analysis allows water removal, zero and first order phase correction and apodization. It also calculates peak integrals of critical metabolites, their ratios, and generate metabolite maps (Figure 3).

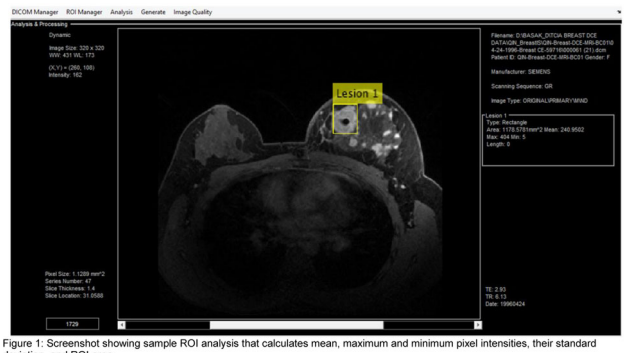

Figure 1: Screenshot showing sample ROI analysis that calculates mean, maximum and minimum pixel intensities, their standard deviation, and ROI area

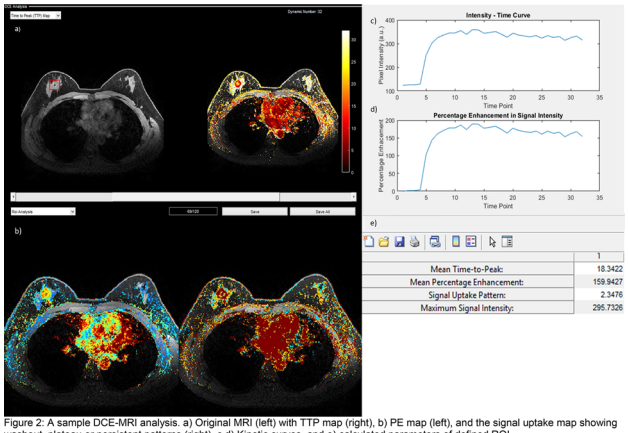

Figure 2: A sample DCE-MRI analysis. a) Original MRI (left) with TTP map (right), b) PE map (left), and the signal uptake map showing washout, plateau or persistent patterns (right). c,d) Kinetic curves, and e) calculated parameters of defined ROI.

Features illustrated at the Exhibit:
BreastIS is a flexible and open source software tool capable of analyzing, visualizing and quantifying various breast MRI. It provides an efficient visualization with its easy to use, and simple user interface. The software will be freely available with new features for research purposes on GitHub by June 2019.
Acknowledgement:
This project has been funded by TUBITAK 116E155 '*1H Bilateral and Flexible Breast RF Coil Design for Magnetic Resonance Imaging Systems' grant*.
References:
1. Kuhl et al., Radiology, 1999. **211**(1): p. 101–10.
2. *Statistical Parametric Mapping: The Analysis of Functional Brain Images*. 1st ed. 2006.

SE01.02
VoxLogicA: Voxel-based Logical Analyser

V. Ciancia[1], G. Belmonte[2], D. Latella[1], M. Massink[1]

[1]*Consiglio Nazionale delle Ricerche, Istituto di Scienza e Tecnologie dell'Informazione 'A. Faedo', Pisa, ITALY,* [2]*Azienda Ospedaliera Universitaria Senese, Medical Physics, Siena, ITALY*

Purpose of the Software: VoxLogicA [1] is a free and open source, multi-platform tool, catering for a novel approach to image segmentation, bringing in ideas from formal methods in software engineering, rapid-development, and declarative programming languages, that have been successful in other domains.
In a few lines of code, complex analyses can be specified, translating domain knowledge into logical properties. For instance, in brain tumor segmentation, logical properties encode facts such as "the oedema touches the tumor", or "the tumor contains hyperintense areas; furthermore, very intense areas that are very close to hyperintense ones, are part of the tumor". Such constraints are extremely effective at filtering noise in automated analysis.
The logical core is extended by including imaging primitives, e.g., texture similarity or image normalisation. The language is "a query language for image analysis". Its innovation potential can be compared to that of the "Structured Query Language" SQL, that revolutionised automated data analysis, by permitting queries on large datasets to be designed by experts of the domain to which the data belongs, instead of computer programmers.

In related work [2], about 200 3D cases of brain tumor from the BRATS challenge have been contoured for radiotherapy, using a short (10 lines) logical specification (see Fig. 1), with average DICE score of 0.88 (GTV) and 0.90 (CTV) (see Fig. 2). Execution time is about 10 s per case on a standard desktop machine. The procedure can be explained very easily, and it is amenable to improvement by the community. No machine learning was needed to obtain such results, although the two approaches could be combined on a by-need basis.

```
let background = touch(flair < 0.1,border)
let brain = !background
let pflair = percentiles(flair,brain)

let hI = pflair > 0.95
let vI = pflair > 0.86
let hyperIntense = flt(5.0,hI)
let veryIntense = flt(2.0,vI)

let growTum = grow(hyperIntense,veryIntense)
let tumSim = similarFLAIRTo(growTum)
let tumStatCC = flt(2.0,(tumSim > 0.6))
let tumFinal= grow(growTum,tumStatCC)
```

Fig. 1: Specification of tumor segmentation in VoxLogicA

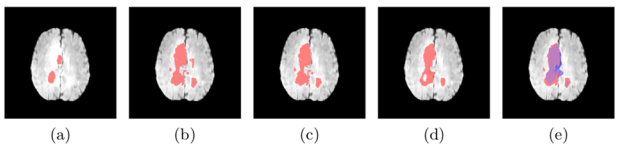

Fig. 2: Segmentation results of the procedure in Fig. 1: image Brats17_2013_2_1, FLAIR, axial 2D slice at Z=97. (a) hyperIntense (b) veryIntense (c) growTum (d) tumStatCC (e) tumFinal (red) and manual (blue, overlapping area is purple)

Methods/Implementation: VoxLogicA reuses methods from "model checking", a branch of Computer Science devoted to the fully automated analysis of software. Logical specifications are automatically turned into parallel execution plans. Tasks of the execution plan are then run using the Insight Toolkit (ITK). 2D and 3D NIFTI, jpg and png images can be loaded and saved. Multimodal analysis is also made easy by the tool; several images from different modalities can be loaded, and related to each other via logic formulas.

Features illustrated at the Exhibit: We shall illustrate the interface and basic functionality of the tool, showing how to program and execute logical specifications of image analysis procedures, both on simple 2D test cases and on 3D images from the glioblastoma case study.

References:

[1] https://github.com/vincenzoml/VoxLogicA.

[2] Belmonte, Ciancia, Latella, Massink, Springer, 2019 https://link.springer.com/chapter/10.1007%2F978-3-030-17462-0_16 (preprint https://arxiv.org/abs/1811.05677).

SE01.03

BASIL: Bayesian Inference for Quantitative Arterial Spin Labelling Perfusion

M. A. Chappell,
M. Y. Zhao, F. Kennedy McConnell, Y. Suzuki, M. Craig

University of Oxford, Institute of Biomedical Engineering and Wellcome Centre for Integrative Neuroimaging, Oxford, UNITED KINGDOM

Purpose of the Software: BASIL provides both GUI and command line tools for the quantification of cerebral perfusion from Arterial Spin Labelling data. It includes all of the main steps required to analyse single-subject data and prepare individual data for subsequent group analysis. BASIL can analyse the majority of flavours of ASL, including both single and multiple post label delay data. Advanced options include correction for distortion, field inhomogeneity, macrovascular contamination [1] and partial volume effects [2].

BASIL is part of the FMRIB Software Library (www.fmrib.ox.ac.uk/fsl/BASIL) and can integrate with other analyses that might be required in a larger neuroimaging study.

Methods/Implementation: BASIL is built around a fast Bayesian inference algorithm [3] that can maximise the information obtainable from ASL data in a robust manner by exploiting prior information about typical haemodynamic parameters and the typical homogeneity of perfusion in organs. By using a Bayesian method the algorithm can scale seamlessly from simple single PLD ASL right up to more complex acquisitions that also offer more measurable information about perfusion kinetics.

It is implemented in C ++ allowing for fast computation, for example whole brain ASL in < 5 min is possible. A comprehensive GUI is provided that will suit the majority of users, but more advanced and tailored analysis is possible via command line tools.

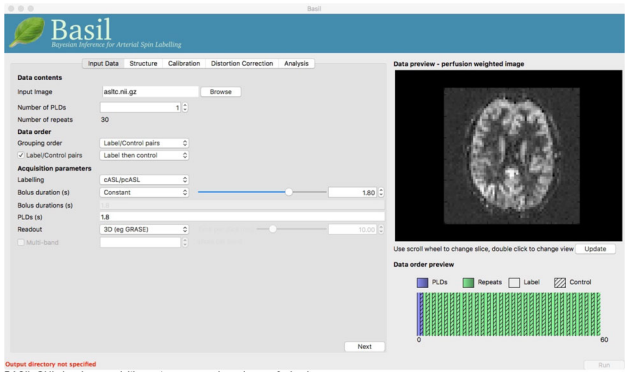

BASIL GUI showing acquisition setup page and preview perfusion image

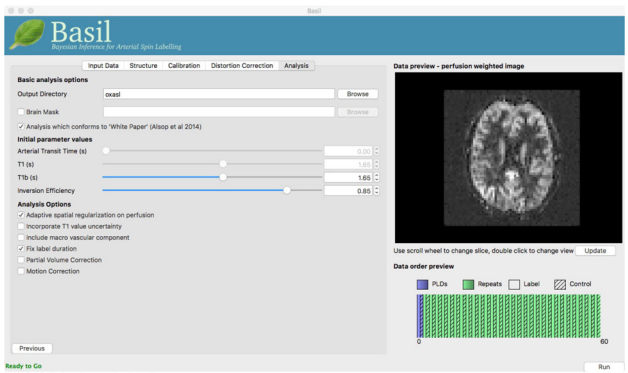

BASIL GUI showing analysis options

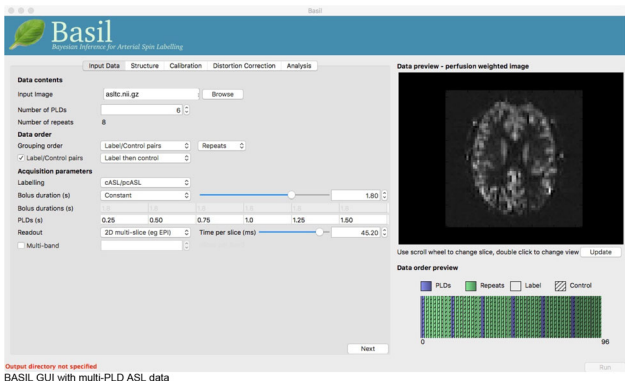

BASIL GUI with multi-PLD ASL data

BASIL comes as part of FSL (v 6.0.1) and can thus be used on OS X and Linux natively. A virtual machine is available for Windows installation.

Features illustrated at the Exhibit: A step-by-step walkthrough of how to quantify perfusion from both single and multi-PLD pcASL data using BASIL via the graphical user interface. A range of tutorials are also available online at www.neuroimagingprimers.org

References:

[1] Chappell, M. A., Groves, A., Whitcher, B. & Woolrich, M. Variational Bayesian Inference for a Nonlinear Forward Model. *IEEE Transactions on Signal Processing* **57,** 223–236 (2009).

[2] Chappell, M. A., Groves, A. R., Macintosh, B. J., Donahue, M. J., Jezzard, P. & Woolrich, M. W. Partial volume correction of multiple inversion time arterial spin labeling MRI data. *Magn Reson Med* **65,** 1173–1183 (2011).

[3] Chappell, M. A., MacIntosh, B. J., Donahue, M. J., Günther, M., Jezzard, P. & Woolrich, M. W. Separation of macrovascular signal in multi-inversion time arterial spin labelling MRI. *Magn Reson Med* **63,** 1357–1365 (2010).

SE01.04
Image reconstruction pipeline

F. Luesebrink[1], F. Luesebrink[2], H. Mattern[2], S. Oeltze-Jafra[1], S. Oeltze-Jafra[3], O. Speck[2], O. Speck[3], O. Speck[4], O. Speck[5]

[1]*Otto-von-Guericke University, Department of Neurology, Medicine and Digitalization, Magdeburg, GERMANY,* [2]*Otto-von-Guericke University, Institute for Physics, Biomedical Magnetic Resonance, Magdeburg, GERMANY,* [3]*Center for Behavioral Sciences, Magdeburg, GERMANY,* [4]*German Center for Neurodegenerative Disease, Magdeburg, GERMANY,* [5]*Leibniz Insitute for Neurobiology, Magdeburg, GERMANY*

Purpose of the Software: Image reconstruction at the scanner's console is to some extend a black box and no offline out-of-the-box image reconstruction pipeline is publicly available. While e.g. Gadgetron[1] and BART[2] exists, they do offer a set of tools to reconstruct data rather than an easy to use reconstruction pipeline. The presented pipeline (Fig. 1) can handle Siemens raw data following a Cartesian trajectory at the moment only. However, it is easily extendible, e.g. dealing with radial undersampled data using BART or reading in the ISMRM raw data format[3]. Using a readily available open source reconstruction pipeline promotes reproducible research. Therefore, the pipeline will be made freely available soon.

After extraction of raw data (mapVBVD [7]), the channels are pre-whiten. Then data can be denoised optionally and filtered in k space (3D Tukey window [8]). After iFFT, the channels are combined by adaptive combine [9], and output as NIfTIs.

Methods/Implementation: The reconstruction pipeline is written in MATLAB (tested using 2015b to 2019a on Windows, Linux and MacOS). It contains following features:

[*] Reconstruction of Siemens raw data files that are larger than RAM by writing/reading intermediate results to/from disk, allowing reconstruction of huge raw data files[9,10]. If raw data fits RAM, processing can be done in RAM to improve reconstruction time.

[*] Reconstruction of data in parallel using MATLAB's parallel toolbox by splitting data into chunks. Depending on the processing stage, data are split across channels or slices. Number of CPUs and chunks to be processed can be user specified or detected automatically depending on available number of CPUs and free RAM.

[*] Channel decorrelation by estimating noise covariance matrix (requires noise data from the same session).

[*] Channel combination by sum of squares or adaptive combination[8] (slice-by-slice or 3D).

[*] Channel compression using SVD[11] within adaptive combine to improve reconstruction time.

[*] Writing of correctly oriented magnitude, phase, and complex valued NIfTI files.

[*] 2D GRAPPA reconstruction from ESPIRiT code of Michael Lustig[12].

[*] Application of 3D Tukey filter[13] in k space to reduce Gibbs ringing artifact.

[*] Application of 3D distortion correction (requires gradient coefficient file from Siemens of your specific gradient system)[14].

[*] Application of bias field correction, segmentation, and creation of a brainmask using SPM12[15].

[*] Application of 2D phase unwrapping (per slice) using a total variation approach.

[*] Application of denoising in complex domain during reconstruction. Includes denoising by BM4D[6], all NLM denoiser's of Manjón and Coupé et al.[16–19] as well as using MATLAB's implementation of DnCNN[7] utilizing the neural network toolbox (requires MATLAB 2017a or above).

Features illustrated at the Exhibit: All features can be illustrated at the exhibit.

References:

1. Hansen, M. S. & Sørensen, T. S. Gadgetron: an open source framework for medical image reconstruction. *Magnetic resonance in medicine* **69,** 1768–1776 (2013).
2. Martin Uecker & Jonathan Tamir. *bart: version 0.4.04* (Zenodo, 2018).
3. Inati, S. J. *et al.* ISMRM Raw data format: A proposed standard for MRI raw datasets. *Magnetic resonance in medicine* **77,** 411–421 (2017).
4. Ehses, Philipp,DZNE Bonn, personal communication.
5. Hansen, M. S. & Kellman, P. Image reconstruction: an overview for clinicians. *Journal of magnetic resonance imaging : JMRI* **41,** 573–585 (2015).
6. Maggioni, M., Katkovnik, V., Egiazarian, K. & Foi, A. Nonlocal transform-domain filter for volumetric data denoising and reconstruction. *IEEE transactions on image processing : a publication of the IEEE Signal Processing Society* **22,** 119–133 (2013).
7. Zhang, K., Zuo, W., Chen, Y., Meng, D. & Zhang, L. Beyond a Gaussian Denoiser: Residual Learning of Deep CNN for Image Denoising. *IEEE transactions on image processing : a publication of the IEEE Signal Processing Society* **26,** 3142–3155 (2017).
8. Walsh, D. O., Gmitro, A. F. & Marcellin, M. W. Adaptive reconstruction of phased array MR imagery. *Magn. Reson. Med.* **43,** 682–690 (2000).
9. Lüsebrink, F., Sciarra, A., Mattern, H., Yakupov, R. & Speck, O. T1-weighted in vivo human whole brain MRI dataset with an ultrahigh isotropic resolution of 250 µm. *Scientific data* **4,** 170032 (2017).
10. Lüsebrink, F., Sciarra, A., Mattern, H., Yakupov, R. & Speck, O. Raw data from: T1-weighted in vivo human whole brain MRI dataset with an ultrahigh isotropic resolution of 250 µm.
11. Zhang, T., Pauly, J. M., Vasanawala, S. S. & Lustig, M. Coil compression for accelerated imaging with Cartesian sampling. *Magnetic resonance in medicine* **69,** 571–582 (2013).
12. Michael Lustig. Publicly shared software. Available at http://people.eecs.berkeley.edu/~mlustig/Software.html.
13. Tukey JW. An introduction to the calculations of numerical spectrum analysis. *Spectral Analysis of Time Series* **1967,** 25–46.
14. Yarach, U. *et al.* Correction of gradient nonlinearity artifacts in prospective motion correction for 7T MRI. *Magnetic resonance in medicine* **73,** 1562–1569 (2015).
15. Ashburner, J. SPM: a history. *Neuroimage* **62,** 791–800 (2012).
16. Manjón, J. V., Coupé, P., Buades, A., Louis Collins, D. & Robles, M. New methods for MRI denoising based on sparseness and self-similarity. *Med Image Anal* **16,** 18–27 (2012).

SE01.05

Platform for Enhanced Diffusion MRI Data Processing Pipeline to Guide Tumor Neurosurgery

D. Krahulec[1], F. Thiele[2], M. Versluis[1], P. de Bruin[1], K. van de Ven[1], M. Breeuwer[1]

[1]*Philips Healthcare MR, Best, NETHERLANDS,* [2]*Philips GmbH Innovative Technologies, Research Laboratories, Aachen, GERMANY*

Purpose of the Software: Preoperative workflow comprises two critical steps: anatomical and functional brain mapping. While structural and diffusion MRI have been used to describe the lesion and its surroundings, functional MRI has aided in eloquency localization (language, motor and visual areas) [1]. Effective surgical outcome relies on maximized tumor resection with minimal harm to healthy tissue [2]. Current pre-surgical workflow is time inefficient (nonstandardized approaches, various data formats, tools, etc.), applies suboptimal techniques (tensor-based tractography), and produces inconsistent results [3]. Multiparametric visualization lacks information about geometry and uncertainty. For the evaluation of perilesional white matter, high-definition fiber tractography methods (e.g. CSD) have been proposed [4], overcoming the poor performance of DTI tractography in brain regions with complex nerve fiber architectures. The purpose of the clinical software application prototype is to accelerate preoperative planning, improve overall data processing accuracy, and expand surgeons' knowledge of the tumor-tract relationship.

Methods/Implementation: The prototype solution has been implemented in the Philips IntelliSpace Discovery (ISD) research platform that facilitates convenient integration of both Philips and external tools. Reflecting the latest clinical needs, this application provides automated processing pipelines with more accurate data segmentation and coregistration for structural and diffusion MRI data. These pipelines incorporate tools from external packages, such as MRtrix3 [5], FreeSurfer [6] or ANTs [7]. All external tools run in a Linux environment via Docker [8], and they are sequentially connected with Philips plugins into intermediately controlled processing steps. An advanced VTK-based visualization tool will be attached to the end of the pipelines for 3D representation of the results.
Fig. 1 illustrates the user interface of the ISD's Research Oncology Suite with external plugins. Processed data is stored in the patient/subject directory and viewed without the need for manual reloading (Fig. 2). Diffusion streamlines from anatomically constrained tractography are overlaid on the coregistered anatomical images (Fig. 3).

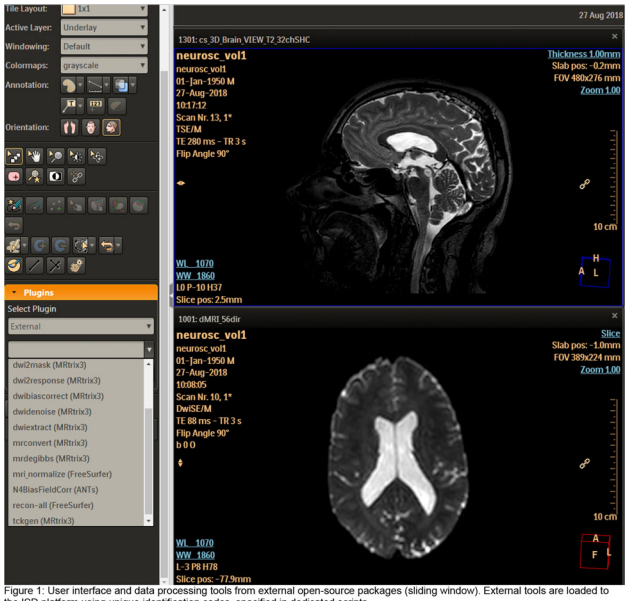

Figure 1: User interface and data processing tools from external open-source packages (sliding window). External tools are loaded to the ISD platform using unique identification codes, specified in dedicated scripts.

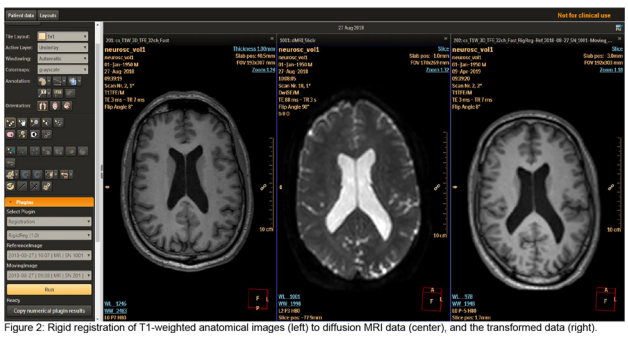

Figure 2: Rigid registration of T1-weighted anatomical images (left) to diffusion MRI data (center), and the transformed data (right).

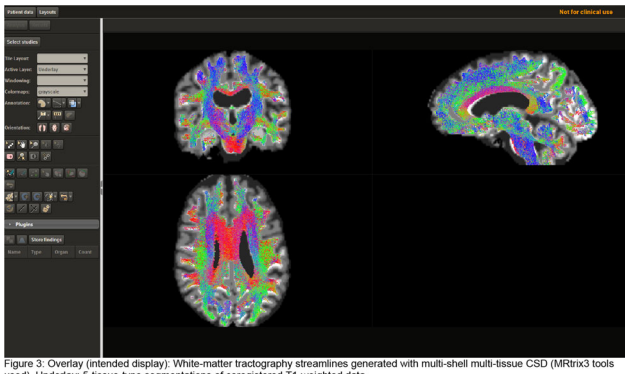

Figure 3: Overlay (intended display): White-matter tractography streamlines generated with multi-shell multi-tissue CSD (MRtrix3 tools used). Underlay: 5-tissue-type segmentations of coregistered T1-weighted data.

Features illustrated at the Exhibit: 1. User interface and architecture of the prototype
2. Patient/subject data handling on study/scan level
3. Data processing step (combining plugins and external tools)
4. Data processing pipelines (structural, diffusion MRI data)

References:

[1] Castellano et al. Curr. Treat. Options Neurol., 2017; (10): 34.
[2] Dubey et al. Asian journal of neurosurgery, 2018; 13 (2): 302–306.
[3] Schilling et al. Magnetic resonance imaging, 2019; 57: 194–209.
[4] Panesar et al. Neurotherapeutics, 2019; 16 (1): 36–51.
[5] http://www.mrtrix.org/.
[6] https://surfer.nmr.mgh.harvard.edu/.
[7] http://stnava.github.io/ANTs/.
[8] https://www.docker.com/.

SE01.06

Quantiphyse: Quantitative Analysis of Physiological MRI

M. A. Chappell, P. Croal, M. Y. Zhao, M. Craig

University of Oxford, Institute of Biomedical Engineering and Wellcome Centre for Integrative Neuroimaging, Oxford, UNITED KINGDOM

Purpose of the Software: Quantiphyse (www.quantiphyse.org) is a data visualisation and quantitative analysis tool for physiological MRI. Via a GUI, Quantiphyse allows the user to load imaging data, and perform a range of interactive analyses, before finally turning this into a batch pipeline for future reuse. Quantiphyse is sepcifically designed for use with the increasing number of quantitative and physiological MRI methods.

Methods/Implementation: Quantiphyse includes tools for:
> Quantitative analysis of physiological MRI.
- Arterial Spin Labelling perfusion [1].
- Dynamic Susceptibility Contrast perfusion [2,3].
- Dynamic Contrast Enhanced perfusion.
- Chemical Exchange Saturation Transfer [4].

> Image viewing and timeseries plotting tools.
> Automated region generating tools, clustering and supervoxel methods.
> Loading and manual definition of regions of interest (ROI).
> ROI-based summaries of descriptive statistics.

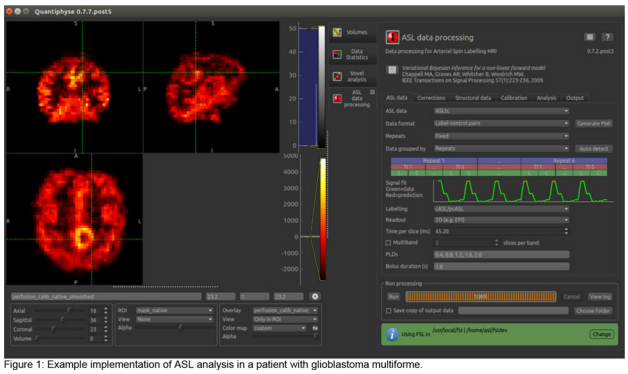

Figure 1: Example implementation of ASL analysis in a patient with glioblastoma multiforme.

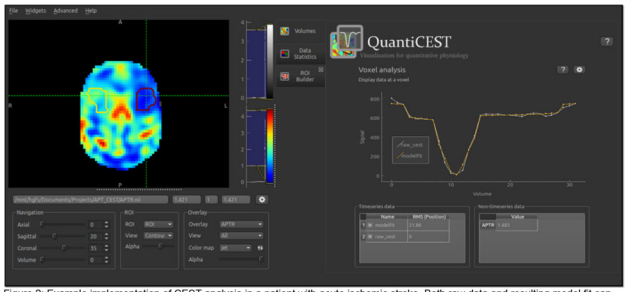

Figure 2: Example implementation of CEST analysis in a patient with acute ischemic stroke. Both raw data and resulting model fit can be visualised and compared on a voxelwise basis.

Quantiphyse is available as a package for Windows, OS X and Linux via the Oxford University Software Store (free for academic use), or via PyPi.

Features illustrated at the Exhibit: Hands-on tutorials for perfusion and Chemical Exchange Saturation Transfer image analysis using brain imaging data from healthy individuals and patients with high-grade glioma.

A range of tutorials are available online at: www.quantiphyse.org

References:

[1] Chappell, M. A., Groves, A., Whitcher, B. & Woolrich, M. Variational Bayesian Inference for a Nonlinear Forward Model. *IEEE Transactions on Signal Processing* **57,** 223–236 (2009).
[2] Chappell, M. A. & Mehndiratta, A. Correcting for large vessel contamination in dynamic susceptibility contrast perfusion MRI by extension to a physiological model of the vasculature. *Magnetic resonance in …* **74,** 280–290 (2015).
[3] Mehndiratta, A., MacIntosh, B. J., Crane, D. E., Payne, S. J. & Chappell, M. A. A control point interpolation method for the non-parametric quantification of cerebral haemodynamics from dynamic susceptibility contrast MRI. *NeuroImage* **64,** 560–570 (2013).
[4] Chappell, M. A., Donahue, M. J., Tee, Y. K., Khrapitchev, A. A., Sibson, N. R., Jezzard, P. & Payne, S. J. Quantitative Bayesian model-based analysis of amide proton transfer MRI. *Magn Reson Med* **70,** 556–567 (2013).

SE01.07

CEST Simulations: Toolbox for Bloch-McConnell equations with arbitrary number of pools

K. Herz, K. Scheffler, **M. Zaiss**

MPI for Biological Cybernetics, Tuebingen, GERMANY

Purpose of the Software: Realistic simulations of CEST effects are very important with regard to e.g. the choice of saturation parameters or fitting of experimental results. However, most of the time only very few CEST pools or even single pools are used for simulations with regard to computation time and code simplicity. In this work, we present a fast, MATLAB compatible, toolbox for Bloch-McConnell simulations, which is designed in a flexible way that allows simulations of a system with arbitrary number of CEST pools and all types of pre-saturation.

Methods/Implementation: The source code is written in C++ and is callable from MATLAB as a *mex* function. *openMP* is used for parallelization of the different Z-spectra offset simulations and *eigen*[1] for linear algebra operations. The dynamic design allows a variable number of CEST Pools and an optional MT pool with either a Lorentzian or a Super-Lorentzian line-shape. A simple 3 pool model e.g. is defined by the relaxation rates *R1* and *R2*, the exchange rate k, proton fraction f and the chemical shift $\delta\omega$ of a CEST and an MT Pool. In addition, the MT line-shape and the relaxation rates of the water pool need to be set. Figure 1 shows an exemplary Z-Spectrum with **15 CEST pools** in total (9 in vivo pools[2] and 6 paraCEST pools[3]) and a Super-Lorentzian shaped MT Pool.

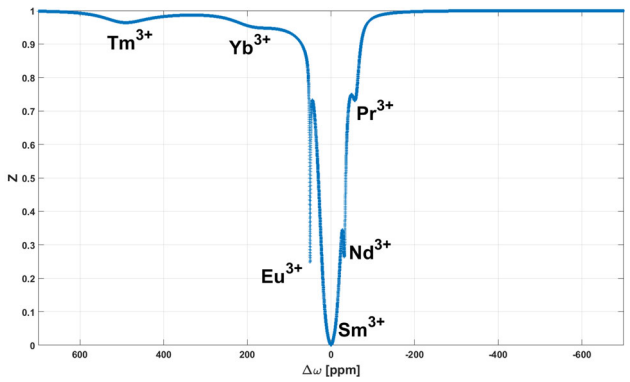

Simulated Z-spectra with 15 CEST Pools and an additional MT Pool.

The code was compiled for a 64-bit Windows 10 OS, using Visual Studio 2017 Professional. Simulation parameters for **continuous wave saturation** were: B_0: 18.8 T; T1: 4 s; T2: 1 s; 1 rectangular pulse with t_{pulse} = 1 s; B_1: 15 μT; Δω = ± 700 ppm; 30 k Z-spectrum samples. Using 6 *openMP* threads, the computation time was approx. 13 s on an Intel i7-7700 K Kaby Lake CPU. The same setting, but with just one CEST and a Lorentzian shaped MT Pool was solved in approx. 0.26 s. Figure 2 shows the simulation of the parameters from reference 2 at B_0 = 9.4T; T1 = 2 s and T2 = 35 ms. Here, **pulsed CEST** with a train of 150 15 ms Gaussian pulses with 50 pulse samples and a duty cycle of 50% was simulated for 100 Z-spectra samples between ± 4.5 ppm.

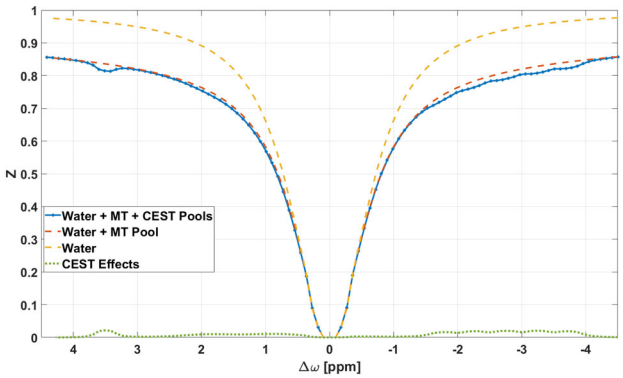

Pulsed simulation using 150 Gaussian pulses and the CEST pool parameters from reference 2

For the 9 CEST Pools and an MT pool this resulted in a computation time of approx. 20 s. The same setting with only water and the MT pool is solved in ∼ 1.1 s and in ∼ 0.25 s for only the water baseline.

Features illustrated at the Exhibit: By using native code, the simulation of Bloch-McConnell equations can be highly accelerated in comparison to MATLAB code. With a compiled simulation as a *mex* function, we provide an interface for MATLAB scripts that can easily be integrated in simulation or fitting procedures. The high flexibility of the simulation is given by:

1. Arbitrary Number of CEST Pools.
2. Pulsed Saturation with arbitrary pulse shapes (e.g. for adiabatic spin lock) and number of pulses.
3. Possible parallelization for usage on CPU clusters.

References:

1. http://eigen.tuxfamily.org.
2. van Zijl et al. *Neuroimage 2018*.
3. Zhang et al. *Accounts of chemical research 2003*.